# Abstract

| | |
|---|---|
| Title of Dissertation: | The Dynamics of Dense Stellar Systems with a Massive Central Black Hole |
| | Michael A. Gill, Doctor of Philosophy, 2011 |
| Dissertation directed by: | Professor M. Coleman Miller |
| | Department of Astronomy |

In this work, we explore the dynamics of two similar types of dense stellar systems with a central black hole of mass much greater than a typical stellar object. In particular, we use numerical N-body simulations to examine the effects that the massive black hole (MBH) has on the surrounding stars and compact objects as they pertain to indirectly observable signals.

The first systems we consider are the highly uncertain cusps likely comprised of primarily massive compact objects that surround the MBHs at the center of typical galaxies. The gradual inspiral of a compact object by emission of gravitational radiation, called an extreme mass-ratio inspiral (EMRI), will produce a signal that falls in the peak detection range of the space-bound laser interferometer space antenna (LISA). Despite a veritable gold mine of astrophysical data that could be gleaned from such a detection, previous investigations in the literature have left the predicted rate of these events uncertain by several orders of magnitude.

We present direct N-body simulations of the innermost $\lesssim 100$ objects with the inclusion of the first-order Post-Newtonian correction with the aim of reducing one of the key uncertainties in the dynamics of these systems - the efficiency of resonant relaxation. We find that relativistic pericenter precession prevents a significant enhancement of the EMRI rate; the rate we derive during this work is consistent with those derived in the literature from less direct methods. We do find, however,

that our EMRI progenitors originate from much closer to the MBH than previous investigations have suggested was likely.

Our second investigation delves into the possibility of finding intermediate-mass black holes (IMBHs), with masses $\sim 10^{2-4} M_\odot$, at the center of dense star clusters. Because of the substantial investment of telescope time needed to perform the multi-year proper motion studies that are likely needed to achieve a definitive detection, careful selection of candidate clusters is prudent. We provide a new observational signature of the presence of an IMBH in a dense star cluster - a quenching of mass segregation.

Our ensemble of direct N-body simulations with $N \leq 32768$ objects and highly varied initial conditions show that the existence of an IMBH with mass $\sim 1\%$ of the total cluster mass limits the mass segregation in visible stars, as measured by the radial gradient in average stellar mass. This effect is consistently visible in systems that have had enough time to reach their equilibrium value of mass segregation, usually about 5 initial half-mass relaxation times. In practical terms, our method will apply to Galactic globular clusters that are fairly small, and that are unlikely to have lost a significant portion of their mass to Galactic tidal stripping.

We apply this method to two of the $\sim 30$ Galactic globular clusters that fit our conservative criteria for application of this method, NGC 2298 and NGC 6254 (M10). Thanks to deep observations by the Hubble Space Telescope Advanced Camera for Surveys, data exist that are sufficient to allow a good comparison to our simulation data. We find that the degree of mass segregation we observe in NGC 2298 is clearly inconsistent with simulations harboring an IMBH at about the $3 - \sigma$ level. In contrast, application of the method to NGC 6254 reveals a mass segregation profile that can only be explained by the presence of either an IMBH or a significant population of primordial binaries ($\gtrsim 5\%$). Unfortunately, a reliable

measure of the binary fraction of NGC 6254 does not exist; however, NGC 6254 is a good candidate for follow-up proper motion studies.

# The Dynamics of Dense Stellar Systems with a Massive Central Black Hole

by

Michael A. Gill

Dissertation submitted to the Faculty of the Graduate School of the
University of Maryland at College Park in partial fulfillment
of the requirements for the degree of
Doctor of Philosophy
2011

Advisory Committee:

Professor M. Coleman Miller, chair
Professor Derek Richardson
Professor Stacy McGaugh
Professor Alessandra Buonanno
Professor Roeland van der Marel
Professor Douglas Hamilton

# Preface

A significant portion of the work that appears in this thesis was published. Chapter 3 was published in *The Astrophysical Journal* as *Intermediate-Mass Black Hole Induced Quenching of Mass Segregation in Star Clusters*(Gill et al. 2008). The applications of the method to the Galactic globular clusters NGC 2298 and NGC 6254 that appear in Chapter 4 both originally appeared in *The Astrophysical Journal* respectively as *Mass Segregation in NGC 2298: Limits on the Presence of an Intermediate Mass Black Hole*(Pasquato et al. 2009) and *The Dynamical State of the Globular Cluster M10 (NGC 6254)*(Beccari et al. 2010).

To my wife and parents

# Acknowledgements

A number of people have helped to make this work possible. I feel as though I have been very lucky in my time at Maryland - almost all of my interactions have been a positive force in my life, and I would like to take this opportunity to highlight those people who have contributed to who I am as a graduating Ph.D. student.

Firstly, I owe great thanks to Cole for being an amazing advisor. Besides putting up with me for nearly all of my time as a graduate student, he always provided a logical guiding hand when I needed it. His unflappable enthusiasm for science and continued optimism in the face of the many frustrations the last few years brought were a continual source of inspiration. Plus, it was always nice to have a regular meeting where, even if just for a short while, I could comfortably say I was not the nerdiest person in the room.

Thanks to all of the wonderful teachers, collaborators and staff into contact with whom I have come in the last many years. Thanks to Derek

# Contents

# List of Tables

# List of Figures

# Chapter 1

# Introduction

One of the fascinating aspects of astronomy is the existence of objects and scales of almost unfathomable mass, speed, size and number. Even our own Solar System spans a distance scale that is sufficiently greater than our everyday experiences to boggle the mind. The Universe inspires awe due to its sheer size and curiosity due to its seemingly never-ending supply of riddles. The drive to understand the Universe arises from this combination of wonder and interest, and no single object evokes this combination of reactions more than the massive black hole (MBH, hereafter).

Besides satisfying these criteria many times over, massive black holes are extremely interesting and important astrophysical objects. They power accretion disks and jets more luminous than the billions of other stars that inhabit their host galaxy. Their mass exhibits a puzzlingly tight correlation to the velocity dispersion of the surrounding galaxy stars, despite the lack of feedback between these two populations. Even their very existence raises still open questions about hierarchical galaxy formation, the formation of black holes in the early universe, and the deaths of the first stars. As we learn more and more about black holes, these and many other questions still remain to be answered.

Any mysteries regarding black holes remain difficult to unravel due to the shrouded

nature of these objects. Direct observations are by definition impossible and thus any information must be inferred from either their influence on the surrounding environment or from the radiation emitted from an accretion disk, should one exist. This difficulty has slowed progress in black hole research, and only in the last decade or so has concrete evidence appeared to even confirm their existence. We attempt to add a piece to the MBH puzzle by using dynamical N-body simulations to constrain the impact of a MBH of varying mass on the observable facets of its immediate environment.

## 1.1 What We Know About Massive Black Holes

Despite the fact that the notion of a black hole was first postulated in the late 1700's, the first suggestion of the existence of MBHs was not until the discovery of quasars in the early 1960's (e.g., Salpeter (1964)). The high efficiency of converting gravitational potential energy into radiation suggested the MBH as a mechanism to produce the astonishingly high powers radiated by these strange objects. Since then, the gradual improvement of observational techniques at a variety of different wavelengths has produced increasingly convincing evidence that many if not all elliptical and spiral galaxies contain a MBH at their centers (Kormendy & Gebhardt 2001; Kormendy & Richstone 1995; Richstone et al. 1998), as was initially suggested by Lynden-Bell (1969). In fact, the evidence for the existence of a MBH at our own galactic center is now at least as strong as the evidence for the existence of stellar mass black holes.

Observations have revealed sources in the centers of as many as 10% of galaxies with inferred bolometric luminosities of $10^{46-48}$ erg/s, depending on whether the emission is assumed to be isotropic. These sources, called Active Galactic Nuclei

(AGN) also exhibit X-ray variability on timescales of a few hours, providing a tight upper bound for the size of the region from which this radiation is emitted. This, combined with the line emission from gas moving at speeds of thousands of km s$^{-1}$ strongly suggests that the signal is the result of an extremely deep potential well rather than a stellar process.

While a deep potential well could a priori be the result of a dense cluster of smaller objects, several factors argue for a single massive object being responsible:

1. A dense cluster of objects would be highly unstable dynamically and is likely to undergo core collapse on much less than a Hubble time, even in the presence of many hard binaries (Miller 2006).

2. AGN are surprisingly similar sources considering the wide variation in luminosity, whereas we should expect significant variation in the nature of a signals emitted from a dense cluster of objects depending on the particular details of the system.

3. Around 10% of AGN are associated with jet structures, in which charged particles are ejected en masse from the nucleus in a collimated, relativistic stream. This necessitates both a relativistic potential and a preferred axis for ejection that is stable for long timescales. A spinning MBH satisfies both of these criteria (Begelman et al. 1984).

The tightest constraints on the existence of a MBH come from multi-year ESO VLT observations of stellar orbits around Sgr A$^*$, the radio point source at the center of the Milky Way (Eisenhauer et al. 2005). Fig. 1.1 shows the best fit to these orbital observations from which the dark mass at the center was calculated to be $\sim 4.0 \times 10^6 M_\odot$ at a distance of $7.62 \pm 0.32$ kpc. The innermost of these stars, S2, orbits with a semimajor axis of $\sim 6 \times 10^2$ AU and an eccentricity of $\sim 0.87$,
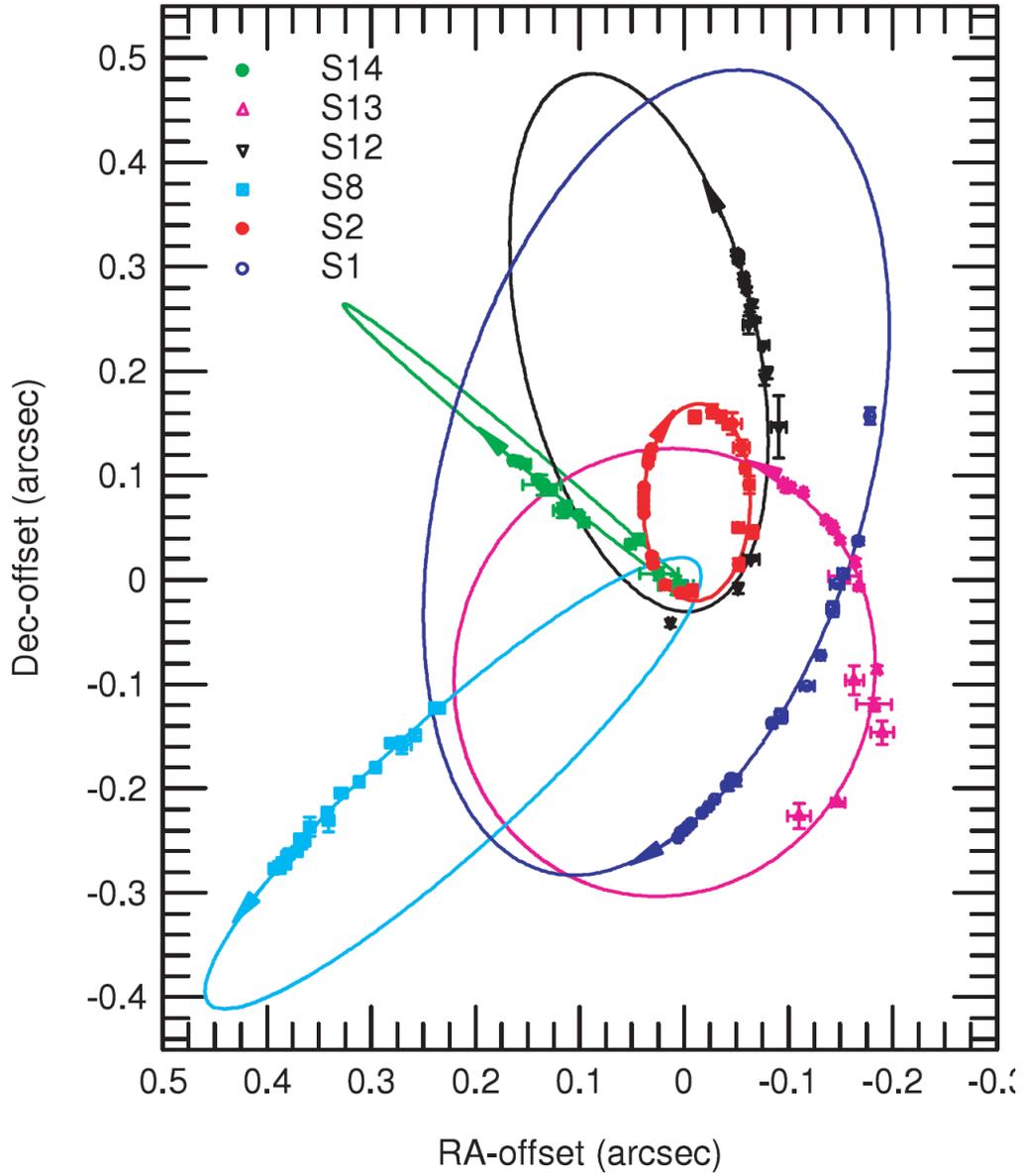
Figure 1.1: **(Figure Credit: Eisenhauer et al. (2005))**
The best fit orbits to multi-year proper motion and radial velocity studies done with the VLT around the dark mass at the center of the Milky Way. The common mass interior to the orbits is inferred to be around $4 \times 10^6 M_\odot$.

and thus a pericenter distance of around 80 AU. The proximity of this object at pericenter to Sgr A* all but excludes explanations that do not include a MBH.

While the existence of MBHs is essentially confirmed, much remains to be determined about their population properties, formation, and growth. Interactions between MBHs and their host galaxies are clearly an important clue in both galaxy formation and evolution. The most famous of these is the tight correlation that exists between MBH mass and the velocity dispersion of its host galaxy. This M-$\sigma$ relation was first noticed at the beginning of the century (Ferrarese & Merritt 2000; Gebhardt et al. 2000), and a modernized rendering is shown in Fig. 1.2, leading to the most recent formulation (Gültekin et al. 2009):

$$\log\left(\frac{M_{BH}}{M_\odot}\right) = (8.12 \pm 0.08) + (4.24 \pm 0.41) \times \log\left(\frac{\sigma}{200\text{km s}^{-1}}\right). \qquad (1.1)$$

The velocity dispersion measurements used in the derivation of the $M - \sigma$ relation are taken from well outside the radius of influence of the MBH, making a purely dynamical explanation for this phenomenon impossible. A connection relating the formation and evolution of the galaxy to the growth of the MBH seems to be the most likely explanation.

Unfortunately, while the growth of the more massive MBH candidates ($\gtrsim 10^8 M_\odot$) is thought to be due to radiatively efficient gas accretion (Marconi et al. 2004; Soltan 1982), little is known about the growth of the smaller MBHs, including the one residing in our own Milky Way. Many suggestions have been made (see Miller et al. (2009) for a brief summary), but the increased difficulty involved in observing these inherently dimmer objects currently stands as a limiting factor in this line of research. Understanding the formation mechanism responsible will require, among other things, a better understanding of the characteristics of the existing population. Unfortunately, even measurements from the next generation telescopes are unlikely to reduce the uncertainty in MBH mass measurements to below a factor of
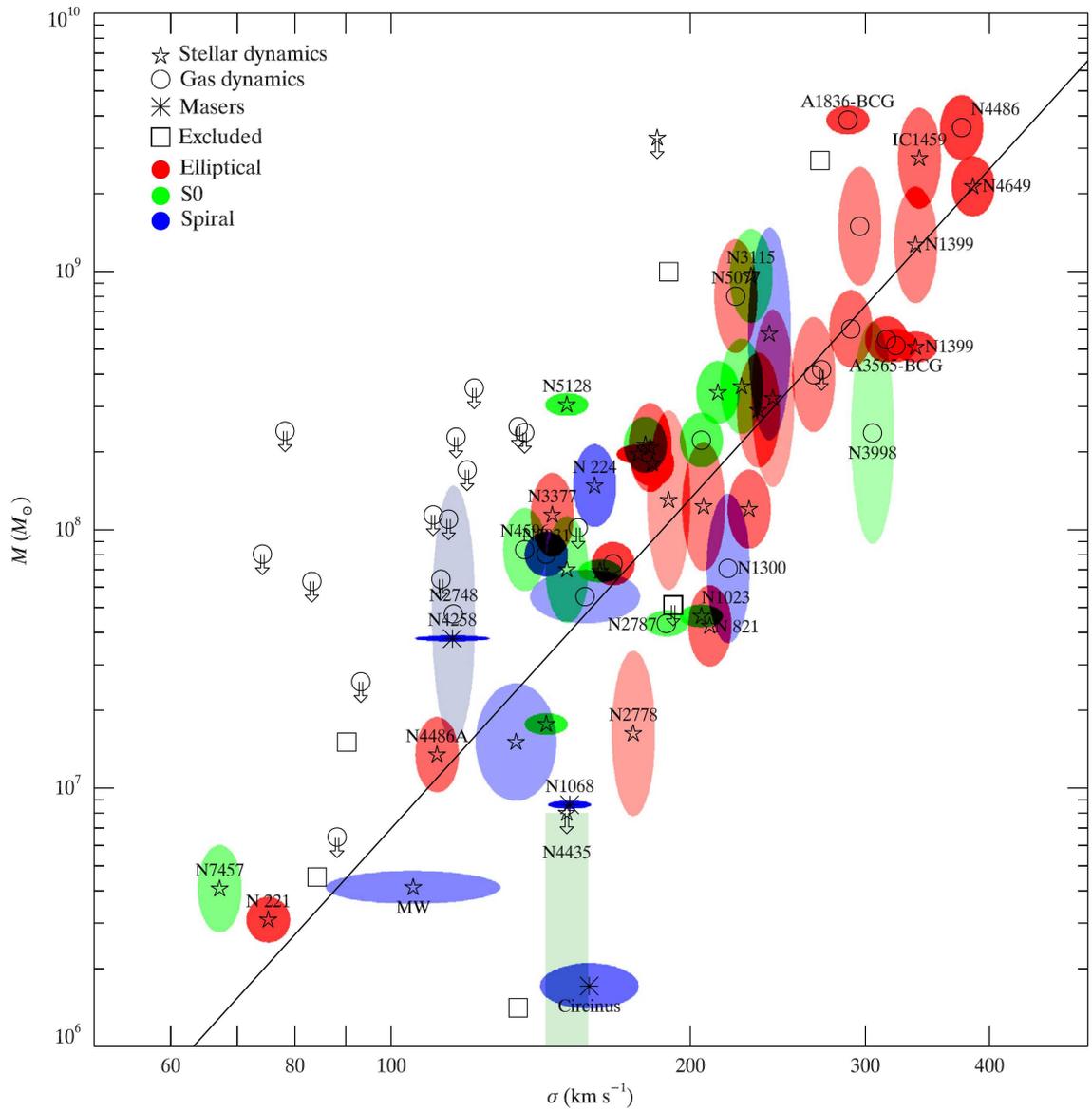
Figure 1.2: **(Figure Credit: Gültekin et al. (2009))**
A modern rendering of the M-$\sigma$ relation, showing the strong correlation between the inferred mass of the MBH at the center of a galaxy and the 3-dimensional velocity dispersion of the surrounding stars.

2 (Miller et al. 2009).

As observations of electromagnetic radiation are proving to be a necessary but not sufficient tool to solve this and other mysteries surrounding MBHs, a new type of instrument brings with it the promise of providing an unprecedented look into the life of these elusive objects.

## 1.2 Gravitational Waves: The Prospect of Seeing Massive Black Holes in a 'hole New "Light"

While the proliferation of multi-wavelength astronomy has greatly improved MBH research, the inherent difficulties involved in directly observing MBH systems has kept progress relatively slow. With the discovery of binary pulsar PSR B1913+16 (Hulse & Taylor (1975), see Weisberg et al. (2010) for the modern rendering shown in Fig. 1.3) providing the first concrete evidence for the existence of gravitational waves (GWs), the prospect emerged of observing MBH systems through the lens of the gravitational radiation they emit.

To this end, the Laser Interferometer Gravitational-Wave Observatory (LIGO) was built. LIGO has since completed its science runs, and, unfortunately, has yet to provide a detection of a GW source. While the next generation of ground-based GW detectors will offer improved sensitivity over LIGO, the unavoidable noise that results from the detectors being on the surface of the Earth greatly limits the available range of frequencies for which an adequate sensitivity can be achieved.

Plans to build the Laser Interferometer Space Antenna (LISA) attempt to circumvent this issue by moving the detector into space. LISA will probe a range of GW frequencies unattainable by Advanced LIGO and the other second-generation terrestrial GW detectors. Provided these detectors are completed and function as
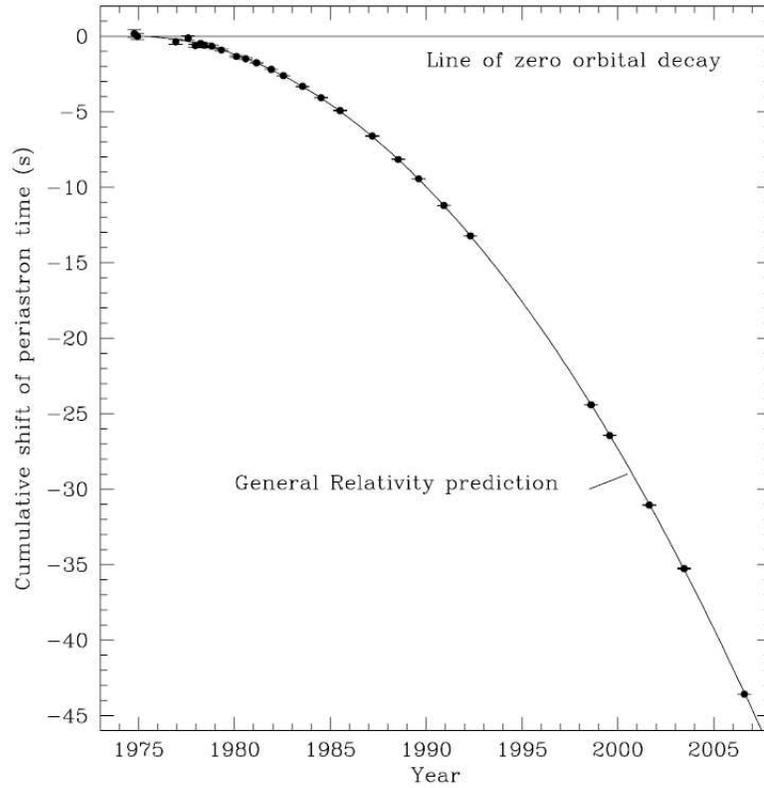
Figure 1.3: **(Figure Credit: Weisberg et al. (2010))**
B1913+16 is a system containing two pulsars in close enough orbit to lose non-negligible energy and angular momentum to gravitational radiation. This configuration allows a precise measurement of the orbital period of the system, which slowly decays. This plot slows the near perfect agreement between this decay over more than 30 yr with the predictions of general relativity.

planned, they will provide a truly unique view of astrophysical systems that have long been invisible in electromagnetic radiation.

While any close encounter between two massive enough objects will emit non-negligible gravitational radiation, we are only concerned with systems that contain enough mass to produce GWs that will reach the Earth with detectable amplitude, and whose signal can be extracted from a data stream whose complexity may

confound even today's fastest computers. The gradual inspiral of a stellar-mass compact object onto a MBH of mass $\sim 10^{4-7} M_\odot$ represents one such signal, even at extragalactic distances (Amaro-Seoane et al. 2007).

This system, called an *extreme mass-ratio inspiral* (EMRI), represents one of the most promising sources of astrophysical data to be mined through the LISA mission. While the coalescence of two MBHs would produce a stronger and more easily detectable signal, detection of an EMRI would actually provide a more valuable test of the strong field limit of general relativity. Because the compact object is essentially a test particle in the field of the MBH, the gravitational waves produced by this system carry otherwise unobtainable information about the (nearly Kerr) spacetime around the horizon of the MBH (Ryan 1995), in addition to the mass of the MBH, its spin, as well as the mass and orbital elements of the inspiraling compact object.

Fig. 1.4 shows a simulation of the relative signal strengths of the expected sources of LISA-detectable GWs. Extracting the signal from an extragalactic EMRI from the much stronger foreground noise generated by Galactic compact binaries will be difficult, but theoretically possible due to the longevity of the signal (Amaro-Seoane et al. 2007). The addition of information about the likely rate and orbital characteristics of EMRIs would enhance the likelihood of obtaining a detection, as the gravitational waveforms themselves are strong functions of eccentricity (e.g. Barack & Cutler (2004); Wen & Gair (2005)). In order to provide this information, we require a detailed understanding of the complex dynamics that occur at the centers of galaxies where these systems are found.

To produce a LISA-detectable EMRI signal at extragalactic distances, a compact object must orbit closely enough to radiate continuously in the projected LISA peak frequency range (0.1-100 mHz, see Larson et al. (2000)), corresponding to an orbital
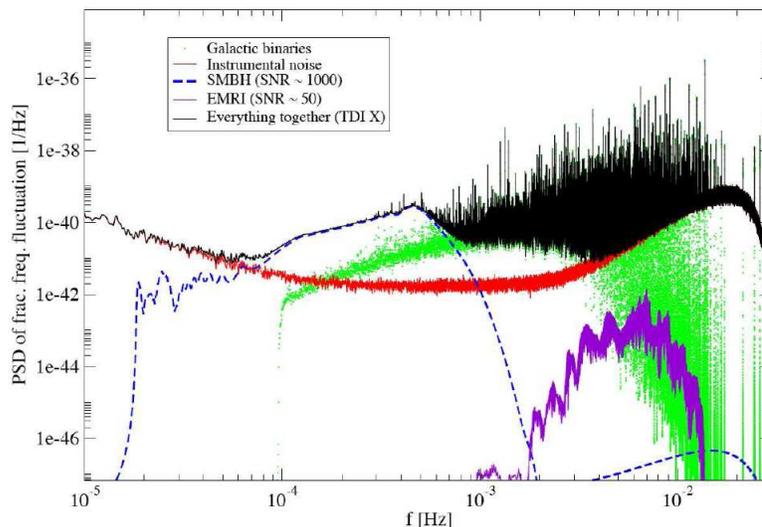
Figure 1.4: **(Figure Credit: Amaro-Seoane et al. (2007))**
A synthetic model of the relative strengths of various LISA-detectable signals. The
stream will likely be dominated by Galactic white-dwarf binaries at the wavelengths
emitted by an EMRI signal. The longevity of the EMRI, which will radiate contin-
uously during the last $\sim$ month of the inspiral should allow the signal-to-noise ratio
to be built up to where a detection is possible.

period $P_{LISA} \leq 10^4 s$. Only during the last $\sim$ month of the inspiral will the object's
period fall below this threshold. Thus, it will be undetectable during most of its
inspiral time, which is given by

$$\tau_{merge} \simeq 6 \times 10^{17} \frac{(1 M_\odot)^3}{M_\bullet m (M_\bullet + m)} \left( \frac{a}{1 AU} \right)^4 (1 - e^2)^{7/2} \text{yr}, \qquad (1.2)$$

where $M_\bullet$ is the mass of the MBH, $m$ is the mass of the orbiting object, and $a$ and
$e$ are the semimajor axis and eccentricity of the orbit, respectively.

Because $\tau_{merge}$ is a strong function of pericenter distance ($r_p \equiv a(1 - e)$), most
EMRI candidates in the standard capture model are objects on highly eccentric
orbits (we note that other models for EMRI formation exist, e.g., Miller et al. (2005)
- we will focus solely on captures in this work). A high eccentricity will cause these

objects to shed energy and angular momentum during close pericenter passages, even when their semimajor axes are still large. During this time, interactions with other stars can disrupt their progress, either raising their pericenter distance to where they will no longer lose energy, or lowering it enough to cause a direct plunge into the MBH. Hopman & Alexander (2005) find that objects with $a \gtrsim .01$ pc are unlikely to be able to shed enough energy to become an EMRI without first being disrupted to a lower-eccentricity or plunge orbit.

Within the innermost .01 pc, the near-Keplerian potential leads to orbits that retain their spatial orientation for many periods. In this regime, the traditional assumption of uncorrelated encounters is no longer valid, and long-lived orbits exert coherent torques on one another leading to greatly enhanced angular momentum relaxation in a process called *resonant relaxation* (Rauch & Tremaine 1996). Resonant relaxation causes linear changes to the magnitude of the angular momenta of the objects on timescales less than the natural precession timescale of the system. Close to the MBH the precession is dominated by the effects of general relativity (GR) . As orbits get farther away from the MBH, orbital precession is caused by the deviations from a pure Keplerian potential caused by the enclosed mass of other orbiting objects.

Previous investigations into the rate of EMRIs have presented mostly semi-analytic and Monte-Carlo simulations of these systems, both with and without the effects of resonant relaxation (e.g. see Hils & Bender (1995), Sigurdsson & Rees (1997), Hopman & Alexander (2005), Hopman & Alexander (2006a), among others). A fully realistic simulation of the radius of influence of a MBH remains beyond modern computational capabilities, so the degree to which resonant relaxation affects the dynamics near a MBH remains a key uncertainty that must be conquered before the EMRI rate can be determined. We do know that the importance of res-

onant relaxation depends critically on the degree to which it is quenched by GR pericenter precession. In Chapter 2, we pick up the quest to better constrain the rate of EMRIs through modern direct N-body simulations both with and without the first-order Post-Newtonian correction.

## 1.3   Intermediate-Mass Black Holes

While the evidence for the existence of both stellar-mass black holes and MBHs mounts, a natural question arises. Is the gap between their masses ($\sim 5 - 25\ M_\odot$ for stellar mass black holes and $\sim 10^{6-9}\ M_\odot$ for MBHs) real and therefore an important clue as to the formation of these two populations? Or do black holes exist to fill this gap that we simply have yet to find - so-called intermediate-mass black holes (IMBHs; with masses $\sim 10^{2-4}\ M_\odot$).

If these objects do exist, extrapolation of the $M - \sigma$ relation (Eq. 1.1) would suggest they exist in stellar systems with velocity dispersions of $\sim 7 - 20$ km/s. Globular clusters are a common example of systems with the requisite velocity dispersion. Indeed, theoretical work has suggested that some globular clusters may harbor IMBHs in their centers (e.g., Portegies Zwart et al. 2004). If this is the case, there are significant consequences for ultra-luminous X-ray sources, gravitational wave emission from dense star clusters, scenarios of hierarchical MBH formation, and the dynamics of globular clusters (GCs) in general (see Miller & Colbert 2004; van der Marel 2004 for an overview).

Definitive evidence for the existence of IMBHs has, however, been elusive. For example, Gebhardt et al. (2002, 2005) argued for an IMBH in G1 based on the analysis of HST line-of-sight velocity data and Keck spectra, but an alternative analysis by Baumgardt et al. (2003a) points out that acceptable dynamic models

without a large central object also fit the observations. Gerssen et al. (2002, 2003) argued that the kinematics of M15 seem to slightly favor the presence of an IMBH, but for this cluster alternative interpretations exist (Baumgardt et al. 2003b; Dull et al. 2003). More recently, the observed line-of-sight kinematics of Omega Cen have also been used to argue for the presence of an IMBH (Noyola et al. 2008).

A more secure identification of an IMBH in a GC can, in principle, be provided by also measuring the proper motion of central stars in order to reconstruct their orbits and thus firmly establish if a central massive point object is present, similar to the Eisenhauer et al. (2005) work done in the Galactic center. Several HST-GO programs based on this idea have been approved in past cycles (e.g. GO10474, PI Drukier; GO10401 & GO10841 PI Chandar; GTO/ACS10335 PI Ford), but to date they have not yielded any indisputable detections. The limitation for such studies is the need to carry out multi-year observations, thus progress is slow. To maximize the chances of success it is thus of primary importance to focus the observations on the candidates most likely to harbor an IMBH.

Candidate selection is possible if one focuses on the indirect influence of the IMBH on the dynamics of its host. Direct N-body simulations by Baumgardt et al. (2004) and Trenti et al. (2007a) found that the presence of an IMBH acts as a central energy source that is able to prevent gravothermal collapse and thus maintain a sizable core to half-mass radius ratio throughout the entire life of the GC. The existence of such a large ($\gtrsim 0.1$) core to half-mass radius ratio in a collisionally relaxed cluster might be due to the presence of an IMBH (see also Heggie et al. 2007). However, the picture becomes more complicated when this signature is transferred from the ideal world of N-body simulations, where a complete knowledge of the system is available, to real observations, where essentially only main sequence and red giant branch stars define the light profile of the system. In fact, an analysis by

Hurley (2007) cautioned that the difference between mass and light distributions can lead to a large observed core to half-light radius ratio for GCs with single stars and binaries only.

In Chapter 3, we continue the search for indirect IMBH fingerprints by focusing on the consequences of the presence of an IMBH on mass segregation. Through direct N-body simulations we show that the presence of a large (of order 1% of the total mass), central mass significantly inhibits the process of mass segregation, even among only visible main sequence stars and giants. To the best of our knowledge this effect was first briefly mentioned in Baumgardt et al. (2004), but left without further quantitative analysis. Quenching of mass segregation is present in all of our simulations with an IMBH, independent of the initial conditions of the cluster, including variations in initial mass function, density profile, strength of the galactic tidal interaction, number of particles and initial binary fraction.

We find that examining the radial gradient in the average visible stellar mass radius is effective in separating star clusters with and without an IMBH, provided that the stellar system is at least 5 initial half-mass relaxation times old. This measure is observationally feasible with current data (for example, see De Marchi et al. 2007 and references therein), and in Chapter 4 we apply this method to existing data for two small Galactic globular clusters, NGC 2298 and M10 to demonstrate the feasibility of this technique.

# Chapter 2

# The Impact of Resonant Relaxation on the Rate of Extreme Mass-Ratio Inspirals

## 2.1   Introduction

In this Chapter, we delve into the dynamics of systems dominated by a MBH with the purpose of estimating the rate of EMRIs. Throughout, we will assume a spherically symmetric system of point-mass objects of average mass $m$ and number density $n$ (which may vary as a function of distance from the center of the system) orbiting a MBH of mass $M_\bullet$. The mutually exerted gravitational attraction of the bodies in the system is the only force that will influence its evolution.

Given the fact that we are observing galaxies after they have existed for billions of years, any compact objects that form on orbits eccentric enough to lose significant energy to gravitational radiation will have merged long ago. Thus, our concern is the rate at which a compact object's orbit at the center of a typical galaxy will be

perturbed into a highly eccentric orbit in an otherwise steady-state system.

On the traditional assumption of uncorrelated encounters between the objects, two-body relaxation is the only process by which orbits change. As objects pass one another, they exchange energy and angular momentum. Because a given encounter is as likely to increase the energy/angular momentum of an object as it is to decrease it, both quantities evolve as a random walk in time

$$\frac{\Delta E}{E_i} \sim \frac{\Delta L}{L_{max}} \sim \left(\frac{t}{t_{rlx}}\right)^{0.5}, \tag{2.1}$$

where $E_i$ is the initial energy of the orbit, $L_{max} = \sqrt{GM_\bullet a}$ is the angular momentum of a circular orbit at a given energy, and $t_{rlx}$ is the characteristic timescale on which these quantities change. This quantity is called the two-body relaxation time, and for an object of mass $m_1$ within a dense cluster of objects of average mass $m$ orbiting a MBH, it is given by (Spitzer 1987)

$$t_{rlx}(r) = \frac{0.339}{\ln\Lambda} \frac{\sigma^3(r)}{G^2 m m_1 n(r)}, \tag{2.2}$$

where $\sigma$ is the velocity dispersion at a distance $r$ from the center of the system, and $\ln\Lambda$ is the Coulomb logarithm. Inside the radius of influence of the MBH, where we will be focusing our attention, $\Lambda \approx M_\bullet/m$ (Amaro-Seoane et al. 2007), and $\sigma(r) \sim \sqrt{GM_\bullet r^{-1}}$, reducing Eq. 2.2 to

$$t_{rlx}(r) = \frac{0.339}{\ln(M_\bullet/m)} \frac{M_\bullet^{1.5}}{(Gr^3)^{0.5} m m_1 n(r)}. \tag{2.3}$$

In general, the angular momentum relaxation time, $t_{rlx}^L$, of an orbiting object with arbitrary eccentricity is shorter than $t_{rlx}$ since it will have $L < L_{max}$ and, thus, will take less time to change by $\vartheta L$. Like with $t_{rlx}$, $t_{rlx}^L$ evolves as a random walk in time

$$\frac{\Delta L}{L} = \left(\frac{t}{t_{rlx}^L}\right)^{0.5}, \tag{2.4}$$

and we relate the two by combining Eqs. 2.1 and 2.4 to yield

$$t_{rlx}^L = \left(\frac{L}{L_{max}}\right)^2 t_{rlx} = \left(\frac{\sqrt{GM_\bullet a(1-e^2)}}{\sqrt{GM_\bullet a}}\right)^2 t_{rlx} = (1-e^2)t_{rlx} \tag{2.5}$$

16

To generate an EMRI in this scenario, we require an orbiting object to reach a critical eccentricity threshold where the timescale to merge due to gravitational radiation is sufficiently less than the local angular momentum relaxation time (making the approximation that $(1 - e^2) \approx 2(1 - e)$ when $e \lesssim 1$)

$$t_{GW} \lesssim C_{EMRI}(1 - e)t_{rlx}, \tag{2.6}$$

where $C_{EMRI}$ is a constant of order 1 chosen to more or less guarantee the sufficiency of this condition. Combining this with Eqs. 1.2 and 2.2 and the parameters of our simulations gives us a critical eccentricity at each semimajor axis where GW emission dominates:

$$\left(\frac{a}{1pc}\right) \lesssim \frac{2.3 \times 10^{-5} C_{EMRI}^{2/7}}{(1 - e)^{5/7}}, \tag{2.7}$$

which we shall henceforth call the critical eccentricity line. We note that regardless of the chosen value of $C_{EMRI}$, there is always a chance that a close encounter with another passing object in the system could perturb a potential EMRI candidate onto a either a less eccentric orbit where $t_{GW} > (1 - e)t_{rlx}$, or onto a plunge orbit where it will be swallowed on an orbital timescale.

The basic picture described above has been explored in the literature in an attempt to determine the EMRI rate, mostly through Monte-Carlo simulations (Freitag 2001; Freitag et al. 2006; Freitag & Benz 2002; Hils & Bender 1995; Hopman & Alexander 2005) and Fokker-Planck analyses (Hopman & Alexander 2005; Sigurdsson & Rees 1997). From these results, the rate of EMRIs is found to be on the order of $10^{-6} - 10^{-8} \text{yr}^{-1}$ for a MBH of mass $10^6 M_\odot$. When combined with the uncertainty in the distribution of dark compact objects near the MBH in galactic centers, as well as the uncertainty in the number density of MBHs of this particular mass, the current estimated LISA event rate for EMRIs spans quite a few orders of magnitude.

Subsequent to these initial works, modifications to the standard picture have been presented. Hopman & Alexander (2006a) extended the Fokker-Planck analysis of Hopman & Alexander (2005) by adding a diffusion term corresponding to the effects of resonant relaxation (RR; see Sec. 2.2 for a thorough description), finding that the rate could be enhanced by a factor of $\sim 10$ depending on the efficiency of RR. In particular, the degree to which the addition of the first-order GR correction to the potential quenches RR will have a significant impact on the event rate. We set out initially with the intention of quantifying this impact via numerical simulations.

Since then, Merritt et al. (2011) have presented direct N-body simulations with and without the Post-Newtonian corrections up to order $(v/c)^5$, the radiation reaction term, as well as deriving a theoretical limit for the maximum eccentricity obtained by resonant relaxation as a function of the orbital semimajor axis (see Sec. 2.2.3). In this Chapter, we attempt to further their exploration of this particular facet of the dynamics of systems with a MBH with the ultimate goal of better constraining the EMRI rate.

This Chapter is organized as follows. First, we provide a summary of resonant relaxation and explore our theoretical expectations for the evolution of these systems. We will then describe the methodology of our numerical simulations. We will then present our results, a comparison to the results of Merritt et al. (2011), and the implications of our results for the EMRI rate.

## 2.2 Overview of the Dynamics of Systems with a Massive Central Black Hole

### 2.2.1 Scalar Resonant Relaxation

Resonant relaxation was first presented in Rauch & Tremaine (1996) and we mainly follow their derivation below. We consider a system of $N \gg 1$ stars of average mass $m$ orbiting a MBH of mass $M_\bullet \gg mN$, conditions that are easily met at the center of a typical galaxy. Deep within the radius of influence of the MBH, the potential is, to lowest order, Keplerian, resulting in nearly closed orbits that remain essentially constant for many orbital periods. This fact invalidates the usual assumption of uncorrelated encounters, as objects will make the same passages by one another repeatedly as they follow their orbital paths.

Even in a purely Newtonian system, however, the orbits will slowly precess due to the deviations from a Kepler potential created by the interior mass of other orbiting objects. The timescale on which a typical star in the system will precess depends on the degree of dominance of the central mass as

$$t_{prec} \sim \frac{M_\bullet}{m_*} t_{orb},$$

where $m_*$ is the total enclosed mass of other stellar-mass objects, and $t_{orb}$ is the orbital timescale. We will use $t_{prec}$ throughout this Chapter to signify this (Newtonian) mass precession timescale. GR pericenter precession also causes changes in the orbits on a timescale given approximately by

$$t_{prec,GR} \simeq \frac{c^2 a(1 - e^2)}{6GM_\bullet} t_{orb},$$

where $a$ and $e$ are the semimajor axis and eccentricity of the orbit, respectively. As general relativistic precession is always prograde and mass precession is retrograde,

the timescale on which an individual object will precess is given by

$$t_{prec,tot} = \left( \frac{1}{t_{prec,GR}} - \frac{1}{t_{prec}} \right)^{-1}. \tag{2.10}$$

We first consider this system on a timescale, $t$, such that $t_{orb} \ll t \ll t_{prec}$. On this timescale, orbits are constant enough that they can be thought of as wires with mass density inversely proportional to the speed of the object at that point in the orbit. A wire with mass $m$ and semimajor axis $a$ will exert a torque on another wire of similar semimajor axis with magnitude

$$\tau \sim \frac{Gm}{a}. \tag{2.11}$$

The total torque acting on a particular wire will, on average, sum to zero in a spherically symmetric system. However, local Poissonian deviations from symmetry will lead to a torque excess in a random direction with average magnitude

$$\tau_{tot} \sim \sqrt{N_a}\tau = \sqrt{N_a}\frac{Gm}{a}, \tag{2.12}$$

where $N_a$ is the number of objects with similar enough semimajor axes to contribute. Objects with semimajor axes greater than twice the apocenter distance of a given star will have negligible contribution to the torque (Gürkan & Hopman 2007). Because these torques are coherent, the fractional change in the specific angular momentum grows linearly as

$$\frac{\Delta L}{L_{max}} \sim \beta_s \frac{\tau t}{aV}, \qquad (t \ll t_{prec,tot}) \tag{2.13}$$

where $V$ is the characteristic orbital speed and $\beta_s$ is a dimensionless constant of order unity. We now use that $GM_\bullet \sim V^2 a$ and $t_{orb} \sim a/V$ to rewrite this as

$$\frac{\Delta L}{L_{max}} \sim \beta_s \frac{m\sqrt{N_a}}{M_\bullet} t/t_{orb}. \qquad (t \ll t_{prec,tot}) \tag{2.14}$$

On timescales $t \gg t_{prec,tot}$ we will see random-walk behavior in $\Delta L/L_{max}$ with each step being of length $t_{prec}$ and, therefore, magnitude given by

$$\frac{\Delta L}{L_{max}} \sim \beta_s \frac{m\sqrt{N_a}}{M_\bullet} t_{prec,tot}/t_{orb}. \tag{2.15}$$

20

Thus, the overall evolution of the angular momentum is

$$\frac{\Delta L}{L_{max}} \sim \beta_s \frac{m\sqrt{N_a}}{M_\bullet} \left(\frac{t_{prec,tot}t}{t_{orb}^2}\right)^{1/2}, \qquad (t \gg t_{prec,tot}) \qquad (2.16)$$

and, in the pure Newtonian case we can reduce this further via Eq. 1 to

$$\left(\frac{\Delta L}{L_{max}}\right)_{Newt} \sim \beta_s \sqrt{\frac{m}{M_\bullet}}(t/t_{orb})^{1/2}. \qquad (2.17)$$

This leads to a reduced angular momentum relaxation time, defined by $(\Delta L/L_{max})_{Newt} \sim (t/t_{rel})^{0.5}$, of

$$t_{rel} \sim \frac{M_\bullet}{m}t_{orb}. \qquad (2.18)$$

### 2.2.2 Vector Resonant Relaxation

Over timescales $t \gg t_{prec,tot}$, objects trace out planar rosettes in space. One can also consider the mutual torque between two rosettes. These torques effectively act between disk-like structures, so they cannot affect the shape of the orbits within the rosettes, only their spatial orientations. These torques will add coherently with magnitude $T \sim N^{1/2}Gm/a$ on timescales $t \ll t_{prec}^L$, where

$$t_{prec}^L \sim \sqrt{N_a}\frac{M_\bullet + m}{m}t_{orb} \qquad (2.19)$$

is the timescale on which the rosettes precess. In near-Keplerian systems where $M_\bullet \gg m$, we expect

$$t_{prec}^L \sim \sqrt{N_a}t_{prec}. \qquad (2.20)$$

Vector resonant relaxation functions despite the presence of rapid apsis precession, so it will be a factor in the dynamics of systems with a MBH. However, as it cannot affect the pericenter of orbits, we will mostly focus our attention on scalar resonant relaxation in this work.

## 2.2.3 Derivation of the Maximum Eccentricity From RR

As noted in Rauch & Tremaine (1996) and Hopman & Alexander (2006a), GR peri-center precession will greatly reduce the efficiency of resonant relaxation by scrambling the torques exerted on a particular object's orbit and limiting the period of coherent change to its angular momentum. However, Merritt et al. (2011) discovered that it also creates the so-called **Schwarzschild Barrier**, which is a theoretical maximum in the eccentricity that can be achieved by resonant relaxation.

We first derive the expression, following the Merritt et al. (2011) derivation, then provide a qualitative explanation. Going back to Eq. 2.12, we have that the total torque excess on a given object in the system $\tau \approx Gma^{-1}\sqrt{N_a}$. Since the total (specific) angular momentum of an object is given by $L = \sqrt{GM_\bullet a(1 - e^2)}$, the timescale on which $L$ changes is

$$t_L \approx \frac{L}{\tau} \approx \frac{\sqrt{GM_\bullet a(1 - e^2)}}{Gma^{-1}\sqrt{N_a}} = \frac{M_\bullet}{m}\sqrt{\frac{a^3(1 - e^2)}{GM_\bullet N_a}}. \tag{2.21}$$

In order for resonant relaxation to significantly affect the angular momentum of the object, this timescale must be less than the precession timescale due to GR, which is given in Eq. 2.9 as

$$t_L \lesssim t_{prec,GR} \simeq \frac{c^2 a(1 - e^2)}{6GM_\bullet}t_{orb} = \frac{2\pi c^2 a^{5/2}(1 - e^2)}{6(GM_\bullet)^{3/2}} = \frac{2\pi a^{5/2}(1 - e^2)}{3r_s(GM_\bullet)^{1/2}}, \tag{2.22}$$

where $r_s = 2GM_\bullet/c^2$ is the Schwarzschild radius of the MBH, and we have applied Kepler's 3rd Law. Substituting the full form of $t_L$ gives

$$\frac{M_\bullet}{m}\sqrt{\frac{a^3(1 - e^2)}{GM_\bullet N_a}} \lesssim \frac{2\pi a^{5/2}(1 - e^2)}{3r_s(GM_\bullet)^{1/2}}. \tag{2.23}$$

Isolating the term with the eccentricity, asserting that $\pi \sim 3$, and squaring both sides gives us

$$(1 - e^2) \gtrsim \frac{1}{4}\left(\frac{r_s}{a}\right)^2\left(\frac{M_\bullet}{m}\right)^2\frac{1}{N_a}, \tag{2.24}$$

22

thus providing us with a maximum eccentricity that can be attained through resonant relaxation.

In order to understand this, we postulate the following scenario. Suppose that the particular details of the system at some time cause a torque excess that rapidly lowers the angular momentum of an orbiting object to near this barrier. As the object's pericenter becomes lower and lower, it will begin precessing rapidly - much more rapidly than the rest of the system. When the object has precessed by $\pi$ radians, symmetry demands that the same torque excess that caused a decrease in $L$ before will cause the opposite effect now, because the relative constancy of the other orbits leaves the torque excess essentially unchanged. The object will "bounce" off of this invisible barrier and return to a higher value of $L$.

To verify that this effect is indeed the explanation for the Schwarzschild barrier, we assume that the torque on an orbit varies naturally as a simple function of the argument of periapse, $\omega$, as

$$\frac{dL}{dt} = \tau = -\tau_{tot}\cos(\omega), \tag{2.25}$$

where $\tau_{tot}$ is the typical torque excess given by Eq. 2.12. We then rewrite the equation for the precession rate of an orbit in a more convenient form

$$\Delta\omega = \frac{3\pi}{8}\left(\frac{L_{LSO}}{L}\right)^2 (t/t_{orb}), \tag{2.26}$$

where $L_{LSO} = 4GM_{\bullet}/c$ is the angular momentum of the last stable circular orbit. We now change units so that times are measured in units of $t_{orb}$ for the particle under consideration, and so that $L$ is measured in units of $L_{LSO}$, yielding

$$\begin{cases} \dot{L} = -\frac{\sqrt{N}Gm}{a}\cos(\omega) \\ \dot{\omega} = \frac{3\pi}{8L^2}, \end{cases} \tag{2.27}$$

which is a coupled set of differential equations that we can integrate numerically. We start each object at an initial angular momentum of $L_0 = 100L_{LSO}$ and a different
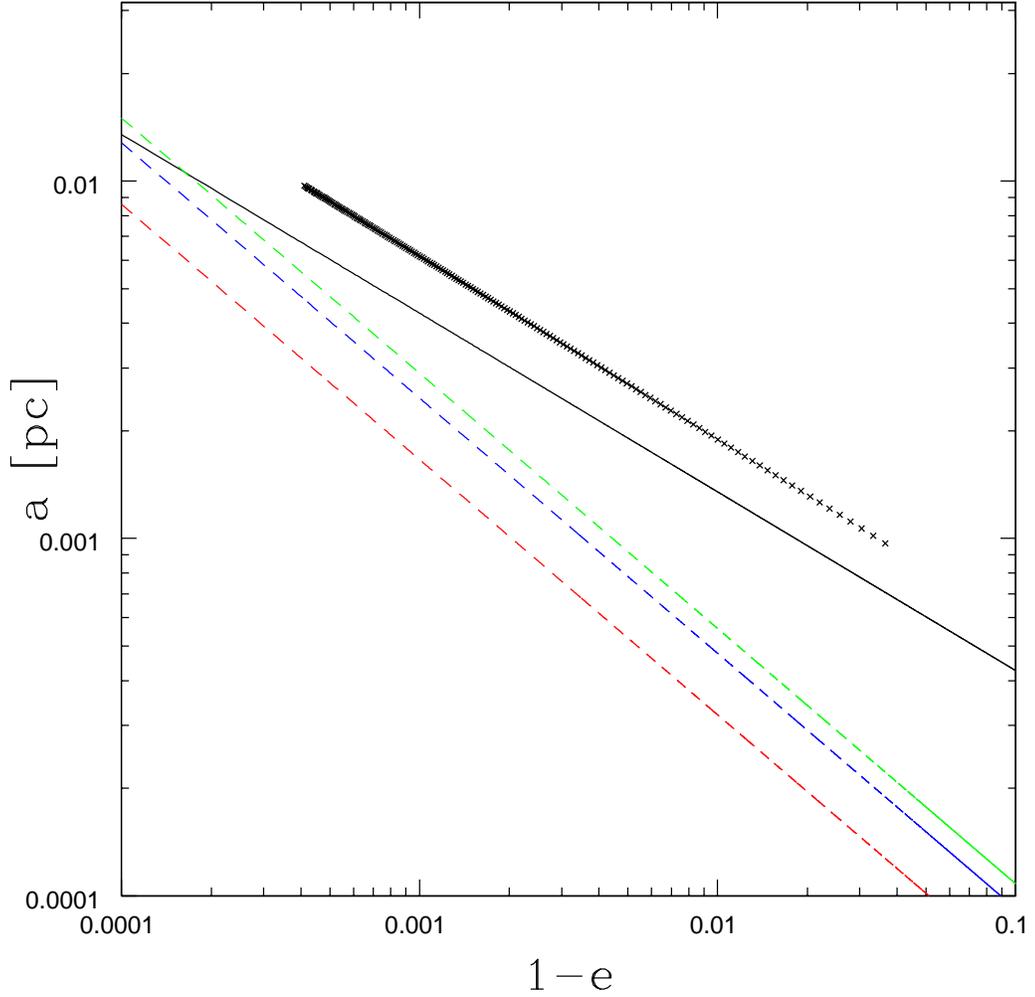
Figure 2.1: Compares the Merritt derivation of the Schwarzschild Barrier (Eq. 2.24; solid line) to the one obtained by our solution to the set of differential equations given in Eq. 2.27 for varying values of the semimajor axis (x points). Also shown as the dashed line is Eq. 2.7 with $C_{EMRI} = 0.1$ (red), 0.4 (blue) and 0.7 (green) for the parameters used our second set of simulations (see Sec. 2.3). The fact that the Schwarzschild Barrier falls above this line for $a \leq .01$ pc indicates that resonant relaxation alone cannot generate an EMRI.

value of the semimajor axis, then step forward in time until a minimum is reached. In Fig. 2.1, we plot these minima with the hatched points alongside the prediction for the Schwarzschild barrier given by Eq. 2.24. We can see that the two are in good agreement, especially given the approximate nature of the preceding derivation. As expected, changing $L_0$ up to $150L_{LSO}$ or down to $50L_{LSO}$ only makes a tiny change in the minimum value of $L$, since nearly all of the accumulation of $\Delta\omega$ happens after the pericenter becomes small. Given this agreement, we can be confident that our assessment of the dynamical picture behind the Schwarzschild Barrier is correct.

## 2.2.4 Theoretical Implications of the Schwarzschild Barrier for the EMRI Rate

Also depicted in Fig. 2.1 is Eq. 2.7 for $C_{EMRI} = 0.1$ (red dashed line), 0.4 (blue dashed line), and 0.7 (green dashed line). An object that crosses this line is extremely likely to inspiral and become an EMRI, but as we can see, the line falls below the Schwarzschild Barrier for our simulation parameters ($a \leq .01$ pc). This means that the barrier will prevent resonant relaxation alone from taking an object with a mildly eccentric orbit and turn it into an EMRI. Thus, we do not expect a massive increase in the rate due to RR.

Since this barrier is not an actual physical barrier, it seems possible that an object near the barrier in the midst of a bounce could be perturbed by an encounter with another orbiting object into an orbit that crosses the barrier. Any object that's near the barrier can experience such a close encounter, but for this to be reasonably likely, the timescale for orbital change (i.e., 2-body angular momentum relaxation time) must be smaller than the time it takes the object to complete the bounce, which is essentially $t_{prec,GR}$. This criterion is thus expressed as (using Eqs. 2.5 and

2.9)

$$t_{rlx}^L \approx .03(1-e^2)\frac{M_\bullet^{1.5}}{\sqrt{Ga^3}m_1 mn(a)} \lesssim t_{prec,GR} = \frac{a(1-e^2)c^2}{6GM_\bullet}t_{orb}, \qquad (2.28)$$

where we have assumed that $\ln M_\bullet/m \sim 10$ and that the relaxation time at radius $r$ holds for an orbiting object at semimajor axis $r$. The eccentricity dependencies cancel nicely, leaving us with a condition on the semimajor axis. We apply Kepler's 3rd law, $t_{orb} = 2\pi\sqrt{a^3/GM_\bullet}$, and make the approximation that $2\pi \approx 6$, leaving

$$.03\frac{GM_\bullet^3}{a^4c^2m_1mn(a)} \lesssim 1. \qquad (2.29)$$

Finally we, make the approximation that $n(a) \sim N/a^3$ and isolate $a$, leaving

$$a_{penetrate} \gtrsim .03\frac{GM_\bullet^3}{Nc^2m_1m}, \qquad (2.30)$$

which for the parameters in the Merritt et al. (2011) simulations (and our second set of numerical simulations) comes out to $a_{penetrate} \gtrsim .01$ pc $= 2000AU$. Below this threshold, we expect objects crossing the Schwarzschild barrier to be scarce. We note that this value is likely to be an overestimation of the true threshold for a two reasons. Firstly, Eq. 2.9 assumes that the angular change per orbit is small, which means that the approximation will break down near the barrier. Secondly, we see in our simulations (as do Merritt et al. (2011) in their simulations) that objects frequently oscillate near the barrier as long as the net background torques remain roughly constant, i.e., the precession timescale of the other objects in the system. Since this will, by construction, be longer, we expect a lower value of $a_{penetrate}$. In fact, Merritt et al. (2011) derive an equation for the same critical value of $a$,

$$\left(\frac{a}{mpc}\right)_{penetrate} \approx 15\left(\frac{C_{SB}}{0.7}\right)\left(\frac{M_\bullet}{10^6M_\odot}\right)^{5/2}\left(\frac{m}{10M_\odot}\right)^{-3/2}\left(\frac{N}{10^2}\right)^{-1/2}, \qquad (2.31)$$

where $C_{SB}$ is a dimensionless constant of order unity that is related to the minimum value of $a$ for which the Schwarzschild barrier exists. Assuming $C_{SB} = 0.7$, we obtain a value of $a_{penetrate} \gtrsim 500$ AU for our EMRI rate simulations.

Given the existence of a barrier preventing orbits from reaching high eccentricity, we might question whether these findings will lower the EMRI rate even below the findings in the literature. Hopman & Alexander (2005) found that the majority of EMRI candidates originate from highly eccentric orbits near the maximum value of $a$ that could lead to a merger, which they found to be around .01 pc. In this region of orbital parameter space, $t_{rlx}^L \sim 2 \times 10^4$yr, meaning that the fractional change in $L$ during a single orbit is $\vartheta 10^{-1}$. These facts suggest that

1. The existence of the Schwarzschild barrier should not decrease previous predictions for the EMRI rate, as RR is not the dominant dynamical effect when the orbital evolution in a single orbit is significant. This can also be seen in Fig. 2.1 from the fact that for large enough semimajor axis, the barrier actually lies to the left of the critical eccentricity line.

2. RR could still enhance the rate of EMRIs by repeatedly bringing objects with $a < .01$ pc near the Schwarzschild barrier, thus giving them many opportunities to be perturbed across the border onto inspiraling orbits.

## 2.3 Numerical Simulations

### 2.3.1 Numerical Methodology

Our original intention in this project was to use **PKDGRAV** (Stadel 2001), to perform our simulations. PKDGRAV is a parallel tree code, which would have allowed it to perform integrations much faster than a direct N-body ever could on a single processor. This would have allowed exploration of significantly higher numbers of objects and longer integration times. However, we were ultimately unable to adapt the code to accurately handle the extremely close encounters that are crucial

Table 2.1: Orbital Precession in HNBody vs. Expected Values

| $a$ | $e$ | $d\omega_{pred}$ | $d\omega_{HNBody}$ | $\Delta d\omega/d\omega_{pred}$ |
|-----|------|---------|----------|-------|
| 100 | 0.99 | 0.0935  | 0.0965   | 0.032 |
| 100 | 0.95 | 0.0191  | 0.0192   | 0.006 |
| 100 | 0.90 | 0.00979 | 0.00982  | 0.003 |

Note. — The integrations were performed with $M_\bullet = 10^6 M_\odot$ and $m = 50 M_\odot$ as in our second set of simulations.

to EMRI formation without adopting a prohibitively low timestep. Full details of our attempt to use PKDGRAV for this problem are described in Appendix B.

We present two sets of simulations in this work. The first set of simulations was created with the intention of observing the degree of resonant relaxation in the inner $\sim 100$ AU, where the gravitational dominance of the MBH is strongest. While this dominance provides the highest potential for RR, it also the creates the shortest precession timescales due to GR. This first group of simulations was performed entirely with **HNBody**, a direct N-body code, with the adaptive fourth-order Runge-Kutta integrator option (Rauch & Hamilton, AJ, in preparation). While itself a purely Newtonian code, HNBody allows optional inclusion of the first-order Post-Newtonian correction as described in Newhall et al. (1983).

As we care about resonant relaxation, it is important that our code replicate the GR pericenter precession well. Tab. 2.1 compares the small-angle precession formula given in Eq. 2.9 to the changes observed during integrations with HNBody. We can see that it closely reproduces the appropriate angular apsis change in the low-angle precession regime where the Eq. 2.9 is valid. We also note that, as expected, the approximate formula gives slightly lower values for the precession than integrating the equations of motion.

Our choice of a direct N-body code was motivated by the desire to correctly resolve the effects of resonant relaxation. However, this choice made simulation of even a significant portion of the radius of influence of the MBH computationally impossible due to the slow nature of the method. To effectively probe the long-term effects of resonant relaxation, we require integration to a final time $t_f \gtrsim (M_\bullet/m_*)t_{orb}$. For objects within $\sim 100$ AU we require $t_f \gtrsim 10^4$ yr to minimally satisfy this criterion. Because of the computational complexity of integrating objects on close orbits to the MBH, we were forced to accept $N \leq 100$ for this group of simulations, despite only integrating to a final time of $t_f = 10^4$ yr.

Even with this short integration time, error accumulation became an issue. While our Newtonian simulations accumulated miniscule error during these integrations, those with the first-order Post-Newtonian correction had substantial, but tolerable error. To some degree, we expect extra accumulation of error when applying this correction when objects have close passages near the MBH. After all, the Post-Newtonian expansion is a Taylor series in $(v/c)$, where $v$ is the velocity of the object and $c$ is the speed of light, and it is common for objects in our simulations to achieve velocities that are $\sim 0.1c$, bordering on a regime where this approximation is no longer valid.

At the conclusion of our first set of simulations, we concluded that it was necessary to explore orbits with larger semimajor axes, as the inclusion of GR pericenter precession nullified the effects of RR in all but our largest system. Concurrently with this realization, the work in Merritt et al. (2011) was initially presented with simulations of fifty $50M_\odot$ point masses orbiting a MBH of mass $10^6 M_\odot$ spanning a volume out to 10 mpc (2000 AU). In order to facilitate a comparison with these results, we adopted these basic initial conditions for most of our second set of simulations. The expansion of the system also allowed us to integrate for substantially

longer ($\sim 10^{5-6}$ yr) due to the decreased computational complexity of a sparser system.

We set out intending to use just HNBody for our second set of integrations as we did for the first. However, our initial integrations with the Post-Newtonian correction accumulated unacceptably high angular momentum error, in some cases greater than the total initial value of the angular momentum of the system. Our investigation into the source of this error revealed that the rapid error accumulations corresponded to the existence of a single object on a highly eccentric orbit with a pericenter of only a few gravitational radii ($r_g = GM/c^2$) around the MBH.

Tab. 2.2 shows the fractional error in a system similar to those in Merritt et al. (2011) due to a single pericenter passage of an object with varying eccentricity (and thus of the pericenter, $r_p$). Obviously, the existence of such an orbit would cause the accumulation of a prohibitive amount of error in a very short integration time, thus rendering its simulation useless. Unfortunately, as we see in the final two columns of Tab. 2.2, increasing the required accuracy of the integration did nothing to assuage this problem. Due to the fact that the evolution of these highly eccentric orbits are crucial to the estimation of the EMRI rate, HNBody alone was insufficient to handle this problem.

In order to address these concerns, we wrote a separate code called **HNBDriver** to iteratively call HNBody in many smaller time increments. After each time segment, the code checks for the existence of objects whose merger time due to gravitational radiation is less than the local two-body angular momentum relaxation time. When such an object exists, it switches over to integrating the system with a second version of HNBody, **HNDrag**, which allows the inclusion of user-specified extra forces. In this case, we include the radiation reaction term (proportional to $(v/c)^5$) from the Post-Newtonian approximation, which is responsible for the energy

Table 2.2: Accumulated Errors During a Single High Eccentricity Orbit with the First Order Post-Newtonian Correction

| e | $r_p/(GM/c^2)$ | $\Delta E/E_i$ | $|\Delta \vec{L}/\vec{L}_i|$ | $\Delta E/E_i^*$ | $|\Delta \vec{L}/\vec{L}_i|^*$ |
|---|---|---|---|---|---|
| 0.999987 | 3.2 | 9.8e-5 | 2.6e-3 | 5.2e-5 | 5.1e-3 |
| 0.999985 | 3.4 | 1.1e-4 | 2.1e-3 | 2.5e-4 | 4.2e-3 |
| 0.999980 | 3.6 | 9.9e-5 | 1.4e-3 | 2.2e-4 | 2.7e-3 |
| 0.999975 | 4.1 | 5.7e-4 | 8.9e-4 | 1.3e-4 | 1.8e-3 |
| 0.999970 | 4.7 | 2.5e-5 | 5.1e-4 | 6.7e-5 | 1.0e-3 |
| 0.999960 | 6.3 | 2.4e-6 | 8.4e-5 | 2.1e-5 | 1.7e-4 |
| 0.999950 | 8.2 | -3.1e-6 | 2.0e-5 | 2.1e-5 | 4.6e-5 |
| 0.999930 | 12.2 | -5.0e-6 | 3.8e-5 | 2.1e-5 | 8.2e-5 |
| 0.999900 | 18.2 | -4.6e-6 | 2.4e-5 | 2.1e-5 | 5.4e-5 |
| 0.999500 | 96.1 | 2.0e-5 | 1.1e-5 | 2.1e-5 | 1.1e-5 |
| 0.999000 | 191.7 | 2.1e-5 | 1.5e-5 | 2.0e-5 | 1.5e-5 |
| n/a | n/a | 2.2e-6 | 4.3e-7 | 2.1e-6 | 2.0e-7 |

Note. — The two columns with a * indicate a higher integration accuracy threshold ($10^{-13}$ instead of the usual $10^{-12}$). The system used consisted of 50 orbiting objects during a single pericenter passage of an orbiting object with semimajor axis $a \sim 2000$ AU and eccentricity given in column 1. The last line of the table shows the errors accumulated during the same integration time for the rest of the system without this particular particle to establish a baseline.

and angular momentum loss. We continue integrating with HNDrag until the object is either perturbed onto an orbit that is unlikely to continue towards a merger, or until its merger time is a small fraction of the local two-body relaxation time. In this case, we remove the offending object on the grounds that it is practically guaranteed to become an EMRI. Full details of HNBDriver are provided in Appendix A. The addition of this code both serves to allow us to provide a reasonable estimation of the EMRI rate as well as limiting the error due to unnecessary (and unphysical) integration of close orbits.

Despite the use of HNBDriver to conduct our second set of simulations, accumulation of error remained a limiting factor in our progress. Unfortunately, some simulations still accumulated prohibitively high angular momentum errors due to

either

1. Objects that were eventually removed from the system, but caused high errors prior to their removal, or

2. Objects whose merger time was never low enough to be removed but whose pericenter passages still resulted in significant error accumulation during the simulation.

In practice, we terminated simulations when the system-wide fractional error in the energy or angular momentum reached around $10^{-2}$. As such only a few of them made it all the way to our desired final integration time of $10^6$ yr.

## 2.3.2 The Likely Source of Error in our Integrations and Its Implications

As stated in the previous section, despite our best efforts, accumulation of error still remained a thorn in the side of our progress. After careful investigation, we have concluded that a significant portion of this error stems from a failure to conserve the motion of the center of mass in a close pericenter passage between an orbiting object and the MBH when tne HNBody is applying the first-order Post-Newtonian correction.

We conducted the following experiment. First, we performed an integration of just a single body on an orbit with a semimajor axis of 2000 AU and an eccentricity of 0.9999 around a MBH of mass $10^6 M_\odot$. The code passed this test with flying colors - the fractional error in the angular momentum during this integration was around $10^{-10}$. However, because the code outputs in barycentric coordinates, any spurious motion of the center of mass would be subtracted out before the output. In order to see this, we added a third object on a nearly circular orbit with $a = 2000$ AU.

Table 2.3: Velocity Jump in a Third Object Due to a Close Pericenter Passage

| t | $x$/AU | $y$/AU | $z$/AU | $v_x$/(AU/yr) | $v_y$/(AU/yr) | $v_z$/(AU/yr) |
|---|---|---|---|---|---|---|
| 24.783 | -59.160461 | -1984.7842 | 0.051256249 | 141.14466 | 9.9165681 | 0.011961366 |
| 24.784 | -59.019316 | -1984.7742 | 0.051268169 | 141.14500 | 9.9268896 | 0.011861988 |
| 24.785 | -58.878171 | -1984.7643 | 0.051279879 | 141.14543 | 9.9387545 | 0.011406578 |
| 24.786 | -58.737026 | -1984.7543 | 0.051288449 | 141.15018 | 10.012879 | -0.0040895004 |
| 24.787 | -58.595876 | -1984.7443 | 0.051284135 | 141.15055 | 10.024314 | -0.0044105982 |
| 24.788 | -58.454725 | -1984.7343 | 0.051279695 | 141.15086 | 10.034616 | -0.0044601151 |

The fractional angular momentum error accumulated during this single pericenter passage jumped to $\sim 10^{-4}$ as a result of adding an object that was nowhere near the interaction of the other two objects.

To investigate further, we examined the actual coordinates of the objects with high time resolution. Tab. 2.3 shows the output of this third object (in barycentric coordinates) just before and after the pericenter passage of the other two objects after $t = 24.785$ yr. Despite being almost 2000 AU away at the time, we see a sudden velocity jump in this object during the exact step where the other two objects experience their close encounter. When we calculate the velocity of the center of mass of the first two bodies, we do indeed see that it also experiences an equal and opposite kick (when multiplied by the appropriate mass ratio) at the same instant.

This explanation also makes sense in light of our experience with the code, namely that we experience significant error accumulation where there is an object making repeated pericenter passages. It also explains why the object causing the problems does not seem to experience any erroneous motion. Because our purely Newtonian simulations accumulated several orders of magnitude less error, it seems possible that there is a problem with the implementation of the Post-Newtonian correction.

The Newhall et al. (1983) implementation that is used by HNBody is given by

$$
\begin{aligned}
\ddot{\vec{r}}_i =\ & \sum_{j\neq i}\frac{\mu_j(\vec{r}_j-\vec{r}_i)}{r_{ij}^3}\left(1-\frac{2(\beta+\gamma)}{c^2}\sum_{k\neq i}\frac{\mu_k}{r_{ik}}-\frac{2\beta-1}{c^2}\sum_{k\neq j}\frac{\mu_k}{r_{jk}}+\gamma\left(\frac{v_i}{c}\right)^2\right. \\
& \left.+(1+\gamma)\left(\frac{v_j}{c}\right)^2-\frac{2(1+\gamma)}{c^2}\dot{\vec{r}}_i\cdot\dot{\vec{r}}_j-\frac{3}{2c^2}\left[\frac{(\vec{r}_i-\vec{r}_j)\cdot\dot{\vec{r}}_j}{r_{ij}}\right]^2+\frac{1}{2c^2}(\vec{r}_j-\vec{r}_i)\cdot\ddot{\vec{r}}_j\right) \\
& +\frac{1}{c^2}\sum_{j\neq i}\frac{\mu_j}{r_{ij}^3}\left([\vec{r}_i-\vec{r}_j]\cdot[(2+2\gamma)\dot{\vec{r}}_i-(1+2\gamma)\dot{\vec{r}}_j]\right)(\dot{\vec{r}}_i-\dot{\vec{r}}_j) \\
& +\frac{3+4\gamma}{2c^2}\sum_{j\neq i}\frac{\mu_j\ddot{\vec{r}}_j}{r_{ij}},
\end{aligned}
\tag{2.32}
$$

where $m_i$ is the mass of body $i$, $\vec{r}_i$, $\dot{\vec{r}}_i$, and $\ddot{\vec{r}}_i$ are its barycentric position, velocity and acceleration vectors, $\mu_j \equiv Gm_j$, $\vec{r}_{ij} = |\vec{r}_j - \vec{r}_i|$, and $\beta = \gamma = 1$ for our purposes. We have omitted the last term in the Newhall et al. (1983) equation, which is unique to solar system applications, and we note that the two terms that contain $\ddot{\vec{r}}_j$ are specific to the application of the Post-Newtonian correction in a barycentric coordinate system.

This implementation turns out to be slightly different from a more recent version given by Blanchet (2006) for two orbiting objects (truncated after the first Post-Newtonian correction)

$$
\begin{aligned}
a_1^i =\ & -\frac{Gm_2 n_{12}^i}{r_{12}^2} \\
& +\frac{1}{c^2}\left(\left[\frac{5G^2m_1m_2}{r_{12}^3}+\frac{4G^2m_2^2}{r_{12}^3}+\frac{Gm_2}{r_{12}^2}\left(\frac{3}{2}(n_{12}v_2)^2-v_1^2+4(v_1v_2)-2v_2^2\right)\right]n_{12}^i\right. \\
& \left.+\frac{Gm_2}{r_{12}^2}\left(4(n_{12}v_1)-3(n_{12}v_2)\right)v_{12}^i\right),
\end{aligned}
\tag{2.33}
$$

where $a_1^i$ is the acceleration of body 1's $i^{th}$ coordinate, $r_{12}$ is the coordinate distance between the two objects, $n_{12}$ is the unit vector in the direction from body 1 to body 2, $v_1$ and $v_2$ are the velocities of the two objects, respectively, and $(v_1v_2)$ denotes the inner product.

These two expressions look almost nothing alike at first but when put into the

same notation they are nearly identical. We start with the Newhall et al. (1983) expression, and recognize that for the purposes of comparison, all of the summation terms contain only one term, since the Blanchet (2006) expression is only between two orbiting objects. Thus, the summations with $i \neq j$ and $i \neq k$ can be replaced by a single term with $j$ as an index, and the terms with $j \neq k$ are replaced by an index of $i$. Making this change and substituting $\beta = \gamma = 1$ yields

$$
\begin{aligned}
\ddot{\vec{r}}_i &= \frac{\mu_j(\vec{r}_j - \vec{r}_i)}{r_{ij}^3} \left( 1 - \frac{4}{c^2}\frac{\mu_j}{r_{ij}} - \frac{1}{c^2}\frac{\mu_i}{r_{ij}} + \left(\frac{v_i}{c}\right)^2 + 2\left(\frac{v_j}{c}\right)^2 \right. \\
&\quad \left. - \frac{4}{c^2}\dot{\vec{r}}_i \cdot \dot{\vec{r}}_j - \frac{3}{2c^2}\left[\frac{(\vec{r}_i - \vec{r}_j)\cdot\dot{\vec{r}}_j}{r_{ij}}\right]^2 + \frac{1}{2c^2}(\vec{r}_j - \vec{r}_i)\cdot\ddot{\vec{r}}_j \right) \\
&\quad + \frac{1}{c^2}\frac{\mu_j}{r_{ij}^3}\left([\vec{r}_i - \vec{r}_j]\cdot[4\dot{\vec{r}}_i - 3\dot{\vec{r}}_j]\right)(\dot{\vec{r}}_i - \dot{\vec{r}}_j) + \frac{7}{2c^2}\frac{\mu_j\ddot{\vec{r}}_j}{r_{ij}}.
\end{aligned} \tag{2.34}
$$

We then replace $\mu_j$ with $Gm_j$, $\dot{\vec{r}}$ by $\vec{v}$, and $(\vec{r}_j - \vec{r}_i)/r_{ij}$ by the unit vector, $\vec{n}_{ij}$, and remove the two terms with $\ddot{\vec{r}}_j$ (which are coordinate-system dependent), giving us

$$
\begin{aligned}
\ddot{\vec{r}}_i &= \frac{Gm_j\vec{n}_{ij}}{r_{ij}^2}\left( 1 - \frac{4}{c^2}\frac{Gm_j}{r_{ij}} - \frac{1}{c^2}\frac{Gm_i}{r_{ij}} + \left(\frac{v_i}{c}\right)^2 + 2\left(\frac{v_j}{c}\right)^2 - \frac{4}{c^2}\vec{v}_i\cdot\vec{v}_j \right. \\
&\quad \left. - \frac{3}{2c^2}(\vec{n}_{ij}\cdot\vec{v}_j)^2\right) + \frac{1}{c^2}\frac{Gm_j}{r_{ij}^2}\left(\vec{n}_{ij}\cdot[4\vec{v}_i - 3\vec{v}_j]\right)\vec{v}_{ij}.
\end{aligned} \tag{2.35}
$$

As our final transformation, we multiply the first term through, pull out a factor of negative one, and then collect all of the terms with a $1/c^2$ together, yielding

$$
\begin{aligned}
\ddot{\vec{r}}_i &= -\frac{Gm_j\vec{n}_{ij}}{r_{ij}^2} + \\
&\quad \frac{1}{c^2}\left(\left[\frac{4G^2m_j^2}{r_{ij}^3} + \frac{G^2m_jm_i}{r_{ij}^3} + \frac{Gm_j}{r_{ij}^2}(-v_i^2 - 2v_j^2 + 4\vec{v}_i\cdot\vec{v}_j + \frac{3}{2}[\vec{n}_{ij}\cdot\vec{v}_j]^2)\right]\vec{n}_{ij} \right. \\
&\quad \left. + \frac{Gm_j}{r_{ij}^2}(4\vec{n}_{ij}\cdot\vec{v}_i - 3\vec{n}_{ij}\cdot\vec{v}_j)\vec{v}_{ij}\right).
\end{aligned} \tag{2.36}
$$

Except for one term, this is identical to Eq. 2.33 if we change the indices from $i, j$ to $1, 2$ and take the $i^{th}$ component of the vector terms. The only difference is that the $3^{rd}$ term in Eq. 2.36 (corresponding to the $2^{nd}$ term of Eq. 2.33) is missing a

factor of 5. This discrepancy at least suggests a possible explanation for the error we see in the HNBody implementation. It is unclear from the equations alone what effect this factor of 5 would have on the dynamics of the system, or whether it would specifically cause a non-conservation of the center of mass of the system. Without the ability to perform more detailed tests, we were unable to further constrain the source of the problem.

Given this discrepancy and the significant accumulation of error during our simulations, we must carefully consider the validity of the results we are about to present in light of this error. Because of the specific nature of the information we are intending to collect, we are confident that our results can still be meaningfully interpreted. To see why this particular error is not critical to our results, we posit 4 regimes for the error accumulation of the system and examine each qualitatively.

1. There are no objects on low-pericenter orbits (at or above the Schwarzschild barrier). In this case, our error accumulation will be minimal and comparable to or possibly even lower than normal integration error.

2. There is an object across or near the Schwarzschild barrier but that has not yet crossed the critical eccentricity line (Eq. 2.7). These objects are critical in the determination of the EMRI rate, but their pericenters are not necessarily high enough to keep the error from accumulating too rapidly - Tab. 2.2 shows that the errors imparted to the rest of the system are relatively constant for $10r_g \leq r_p \leq 100r_g$. Imparting random velocity kicks to the other objects in the system would certainly affect their orbital evolution, although it is not clear how this will retroactively affect our object that is creating the kicks. The importance of these objects combined with the uncertainty in how this error will affect their orbital evolution are why we have decided to terminate our simulations when the fractional angular momentum error reaches $10^{-2}$.

3. There is more than one object in the above regime. It seems likely that each of these objects would deliver unphysical velocity kicks to the other, spuriously affecting the evolution and probably making it easier to cross the Schwarzschild barrier. However, this scenario is extremely unlikely given the brief time for which an object can remain near the barrier (only 6 objects crossed the barrier in over $10^7$ yr of integration time).

4. There is an object that has crossed the line given by Eq. 2.7 into the zone where gravitational radiation becomes dominant. Here, the error accumulation will likely be unacceptably high, as the orbit's pericenter distance will be very low; however, we no longer care about the specific details of the other objects from the perspective of whether or not this object will merge - it is well past the point where resonant relaxation can affect it, and really only a very close passage from another object could deflect it onto a different course. The object's close pericenter passages will be imparting kicks to the other objects in the system, but due to its rapid apsis precession, the kicks will be varying in direction. Randomized kicks are at least as likely to prevent an impending chance close encounter as they are to create one, so the errors we are making should not statistically affect the destiny of these objects. The rest of the system may no longer accurately represent the evolution of a galactic center after the erroneous kicks, but the fact that an EMRI occurred should not be in doubt.

In each of these regimes, it seems likely that our results can likely still be interpreted as somewhat representative of the evolution of a real galactic center as it pertains to the EMRI rate. However, given we cannot predict all of the repercussions of the errors being introduced, we must always view our results in light of this potential shortcoming.

### 2.3.3   Initial conditions

**The First Set of Simulations**

Our choice of initial conditions for the first simulations was designed to allow us to effectively probe resonant relaxation. Within this constraint, we attempted to make the initial conditions agree with the accepted stellar distributions found in the steady-state Fokker-Planck and Monte-Carlo works mentioned in Sec. 2.1. However, since the actual distribution of matter is unknown even at our Galactic center, we made sure to vary the initial conditions to cover as much of the available parameter space as reasonable. The full details of our first set of simulations are reported in Table 2.4.

We chose a MBH mass $M_\bullet = 10^6 M_\odot$ for these simulations. This is comfortably within the range of $10^{4-7} M_\odot$ for a MBH likely to produce a detectable EMRI signal. As we increase the MBH mass, the orbital velocities also increase as $v_{circ} \propto M^{0.5}$, necessitating a smaller timestep for accurate resolution of all encounters, and thereby further limiting our ability to explore longer integration times and larger numbers of objects. In contrast, as we decrease the MBH mass below $10^7 M_\odot$ we encounter fewer and fewer galaxies for which the simulations would be representative. We chose $10^6 M_\odot$ to balance between these two competing effects.

A typical galactic center with a central mass of $10^6 M_\odot$ has a two-body relaxation time of a few Gyr, which is less than the age of these systems when we observe them. As such, we expect that mass segregation, which takes place on a relaxation timescale, will have impacted the stellar distribution by populating the center of the system with massive dark remnants. Our choice of stellar population was designed to account for the fact that mass segregation is likely to have populated the center of the system with the most massive stellar remnants.

Table 2.4: Summary of the First Set of N-body simulations of systems with an MBH.

| Name | N | $\alpha$ | $\langle m \rangle / M_\odot$ | $a_{max}$ | $t_{prec}/t_{orb}$ | $t^L_{prec}/t_{orb}$ | $\delta_{s,max}$ | $\tau\lvert\delta_s = \delta_{s,max}$ |
|------|---|----------|-------------------------------|-----------|--------------------|----------------------|------------------|---------------------------------------|
| 10s2.0 | 10 | 2.0 | 1.0 | $10AU$ | $10^5$ | $3 \times 10^5$ | 0.70 | $3.47 \times 10^5$ |
| 10s2.0GR | 10 | 2.0 | 1.0 | $10AU$ | $10^5$ | $3 \times 10^5$ | 0.30 | $3.85 \times 10^6$ |
| 10bh2.0 | 10 | 2.0 | 6.5 | $10AU$ | $1.5 \times 10^4$ | $5 \times 10^5$ | 0.77 | $4.60 \times 10^4$ |
| 10bh2.0GR | 10 | 2.0 | 6.5 | $10AU$ | $1.5 \times 10^4$ | $5 \times 10^5$ | 0.45 | $2.90 \times 10^6$ |
| 100c2.0 | 100 | 2.0 | 2.5 | $200AU$ | $4 \times 10^3$ | $4 \times 10^4$ | 0.86 | $1.42 \times 10^3$ |
| 100c2.0GR | 100 | 2.0 | 2.5 | $200AU$ | $4 \times 10^3$ | $4 \times 10^4$ | 0.60 | $1.95 \times 10^3$ |
| 100c1.5 | 100 | 1.5 | 2.5 | $100AU$ | $4 \times 10^3$ | $4 \times 10^4$ | 0.81 | $4.30 \times 10^3$ |
| 100c1.5GR | 100 | 1.5 | 2.5 | $100AU$ | $4 \times 10^3$ | $4 \times 10^4$ | 0.55 | $1.27 \times 10^4$ |
| 100s1.5 | 100 | 1.5 | 1.0 | $100AU$ | $10^4$ | $10^5$ | 0.87 | $9.33 \times 10^3$ |
| 100s1.5GR | 100 | 1.5 | 1.0 | $100AU$ | $10^4$ | $10^5$ | 0.45 | $1.44 \times 10^4$ |

Note. — The name of each run indicates:

- The number of stars in the simulation

- Whether the population contains only black holes (bh), evolved compact objects (c) or equal mass stars (s)

- The slope of the density distribution function ($\alpha = 1.5$ or $2.0$)

- Whether or not the simulation was run with the first Post-Newtonian correction (GR)

The last two columns indicate the maximum slope of a linear fit to the scalar change in the angular momentum for the objects in the simulation as a whole (see Eq. 2.39), as well as the number of orbital times at which this slope was realized.

The masses of the objects in our simulations, if not all equal, were drawn from a Salpeter (1955) initial mass function

$$\xi(m) \propto m^{-2.35}, \tag{2.37}$$

usually from an initial mass range of $8 - 100 M_\odot$, then instantaneously evolved into neutron star or black hole-mass objects prior to the start of the simulation. Objects in the mass ranges $8 - 25 M_\odot$ and $25 - 100 M_\odot$ were linearly mapped onto $1.3 - 2.0 M_\odot$ and $5 - 20 M_\odot$, respectively. These simulations are denoted by a "c" in the simulation name in Tab. 2.4. In some simulations, we used either equal

masses of $1.0 M_\odot$ (denoted by an "s" in the name) or all black hole-mass objects created described above (denoted by a "bh" in the name). These different mass ranges allowed us to observe the effects of changing the Newtonian precession time, $t_{prec} = M_\bullet / m_*$, without having to deviate from our desired MBH mass.

The orbits of these objects were chosen with semimajor axes drawn randomly from $n(r) \propto r^{-\alpha}$ with $\alpha = 1.5$ or $\alpha = 2.0$. These values were chosen to be close to the value of $\alpha = 1.75$ expected in a Bahcall & Wolf (1976) cusp while allowing us to observe the effects of varying the density profile. Our mean system densities were set by either $a_{max} = N$ AU or $a_{max} = 2N$ AU. Eccentricities were drawn from a thermal distribution ($P(e) \propto 2ede$), while the other orbital elements were chosen to randomize the orientation of the orbits in space to reflect the spherical symmetry within the radius of influence of the MBH.

**The Second Set of Simulations**

The primary difference between this set of simulations and the first is an increase in volume by a factor of $\sim 10^3$. The semimajor axes were drawn from $n(r) \propto r^{-2}$, but this time from a range of $20 - 2000$ AU, rather than an order of magnitude lower. In order to facilitate a direct comparison to the Merritt et al. (2011) results, we adopted their initial conditions almost exactly for the majority of these simulations. This consisted of 50 point-mass objects each of $50 M_\odot$ orbiting a MBH with mass $10^6 M_\odot$. As before, eccentricities were drawn from a thermal distribution, and the orbital orientations were chosen randomly.

While $50 M_\odot$ is larger than the traditionally expected values for stellar-mass black holes (Woosley et al. 2002), Merritt et al. (2011) note that this model approximately recreates the expected total enclosed mass expected in a volume this size according to previous simulations (e.g., Hopman & Alexander (2006b), Freitag et al. (2006)).

Table 2.5: Summary of the Second Set of N-body simulations of systems with an MBH.

| # of Sims | N | $\langle m \rangle / M_\odot$ | $\tau_{merge,i}$ restricted? | $\langle t_{final} \rangle$/yr | Merger Rate (yr$^{-1}$) |
|---|---|---|---|---|---|
| 5 | 50 | 50 | No | 6.6e5 | 3.0e-7 |
| 4[1] | 50 | 50 | No | 2.4e5 | 1.0e-6 |
| 4 | 100 | 25 | Yes | 3.2e5 | 1.3e-6 |
| 8 | 50 | 50 | Yes | 6.0e5 | 2.1e-7 |
| 4 | 100 | 25 | Yes | 3.9e5 | 6.3e-7 |

Note. — The runs marked with a superscript 1 were started from the end of four of the simulations in the first line of the table. The line in the middle of the table indicates where a different merger threshold was used. In the top group, we required the objects merger time to be a factor of 100 less than the local 2-body angular momentum relaxation time before we remove it. In the second group we lowered this factor to 25. We note one merger that happened in the group with a superscript 1 began the simulation on a very eccentric orbit with $a > 10^4 AU$, and finally merged with $a \sim 10^5 AU$. Since this object would in reality be extremely likely to plunge before merging, we did not count it when calculating our official EMRI rate.

To investigate the effects of (likely more realistically) spreading this mass over more objects, we also ran a number of simulations with 100 objects of mass $25 M_\odot$ spread over the same volume. The full details of the second set of simulations are shown in Tab. 2.5.

There is only one real difference between the initial conditions found in these simulations and those of Merritt et al. (2011). In an effort to limit the initial rate of error accumulation in our simulations, we chose to redraw the orbital elements of objects with initial merger time due to gravitational radiation $t_{GW,i} \leq 1$ Gyr for the majority of our simulations. Besides the computational convenience of this choice, we also justify it based on the fact that most of the galaxies from which we could observe an EMRI signal are significantly older than this. While there are obviously no guarantees, these objects are substantially more likely than other objects in these systems to have already become an EMRI prior to our small window of observation. Still, even provided this is a reasonable approximation, we note that due to this

choice our estimation will likely be unable to constrain the upper limit of the EMRI rate.

## 2.4 Results

### 2.4.1 First Set of Simulations

We began by performing a similar analysis to that done by Rauch & Tremaine (1996). To gain a sense of the overall relaxation of the system, we divided the number of orbital periods elapsed into logarithmic bins. At each system output we calculated, for each object, the fractional change in the energy ($\Delta E/E_0$), the scalar angular momentum ($\Delta|\vec{L}|/L_{max}$), and the vector angular momentum ($|\Delta\vec{L}|/L_{max}$), where $E_0$ is the initial energy and

$$L_{max}(E) \equiv \frac{GM_\bullet}{(2|E|)^{1/2}} \qquad (2.38)$$

is the angular momentum of a circular orbit with energy $E$. We put these values into the bin corresponding to the number of orbital periods experienced by that object and calculated the mean for each bin. This gives us a sense of what is happening on average to the objects in the system at any given number of orbital periods. It is important to note that, because each object in the simulation experiences a variable number of orbits, the data points towards the rightmost part of these plots are only representative of the relaxation of the innermost objects.

Fig. 2.2 shows the evolution of these quantities for several of our Newtonian simulations with varying values of $M_\bullet/m_*$. In each case, we can see the coherent growth of the changes in both $\Delta|\vec{L}|$ (red, dashed curve) and $|\Delta\vec{L}|$ (blue, dotted curve) as compared to the random walk behavior in the growth of the $\Delta E/E_0$ (solid, black curve). This linear growth eventually subsides in all four plots, as the scalar angular

Figure 2.2: Evolution of the fractional change in energy (black, solid line), the scalar angular momentum (red, dashed line), and the vector angular momentum (blue, dotted line) for four of our Newtonian simulations with different values of $t_{prec}$. As we go from upper left to lower right, we see the turnover point in the scalar angular momentum curve (where it stops growing linearly) move to a lower number of orbital times. See Tab. 2.4 for the value of $t_{prec}$ for each simulation.

momentum curves turn over and begin behaving much like the energy curve. In each case the turnover point occurs where $t \gtrsim t_{prec}$, as we expect (see Table 2.4 for the values of $t_{prec}$ for each simulation). We also note that, as predicted by Eq. 2.20, the vector angular momentum curves maintain their coherence for longer than the scalar curves, by a factor of $\sqrt{N} \approx 3 - 10$.

We see a much different picture when we include GR pericenter precession. Fig. 2.3 shows the results of the four simulations corresponding to those depicted in Fig. 2.2, but with the inclusion of the first-order Post-Newtonian correction to the potential. While we can still see coherent growth in the change in $|\Delta \vec{L}|$ due to vector resonant relaxation, the evidence for scalar resonant relaxation is almost nonexistent. A typical object in the 100-particle simulations, with a semimajor axis of 50 AU and eccentricity of $\sim 0.7$ has, by Eq. 2.9, $t_{prec,GR} \sim 4 \times 10^2 t_{orb} \ll t_{prec}$. We expect coherence only on such short timescales that the curve will essentially behave as a random walk. For objects that are close enough to the MBH to experience such rapid apsis precession, we see essentially no enhancement in the rate of scalar angular momentum relaxation.

To better quantify the difference between the Newtonian and Post-Newtonian simulations, we performed linear fits to our relaxation curves for varying numbers of orbital periods, all starting from the beginning of the simulations. Once again following Rauch & Tremaine (1996), we adopted the following fitting forms:

$$\frac{\Delta E}{E_0} = \zeta m N^{1/2} \tau^{\nu}; \qquad \frac{\Delta|\vec{L}|}{L_{max}} = \gamma_s m N^{1/2} \tau^{\delta_s}; \qquad \frac{|\Delta \vec{L}|}{L_{max}} = \gamma_v m N^{1/2} \tau^{\delta_v}, \quad (2.39)$$

where $\tau \equiv t/t_{orb}$. We expect to see the changes in angular momentum in the Newtonian simulations reach slopes substantially greater than the 0.5 that we would expect from just uncorrelated two-body encounters.

Figs. 2.4 and 2.5 show the evolution of these slopes in simulations 100s1.5/100s1.5GR and 100c2.0/100c2.0GR, respectively. As $t \to t_{prec}$, we see $\delta_s$ and $\delta_v$ for the pure
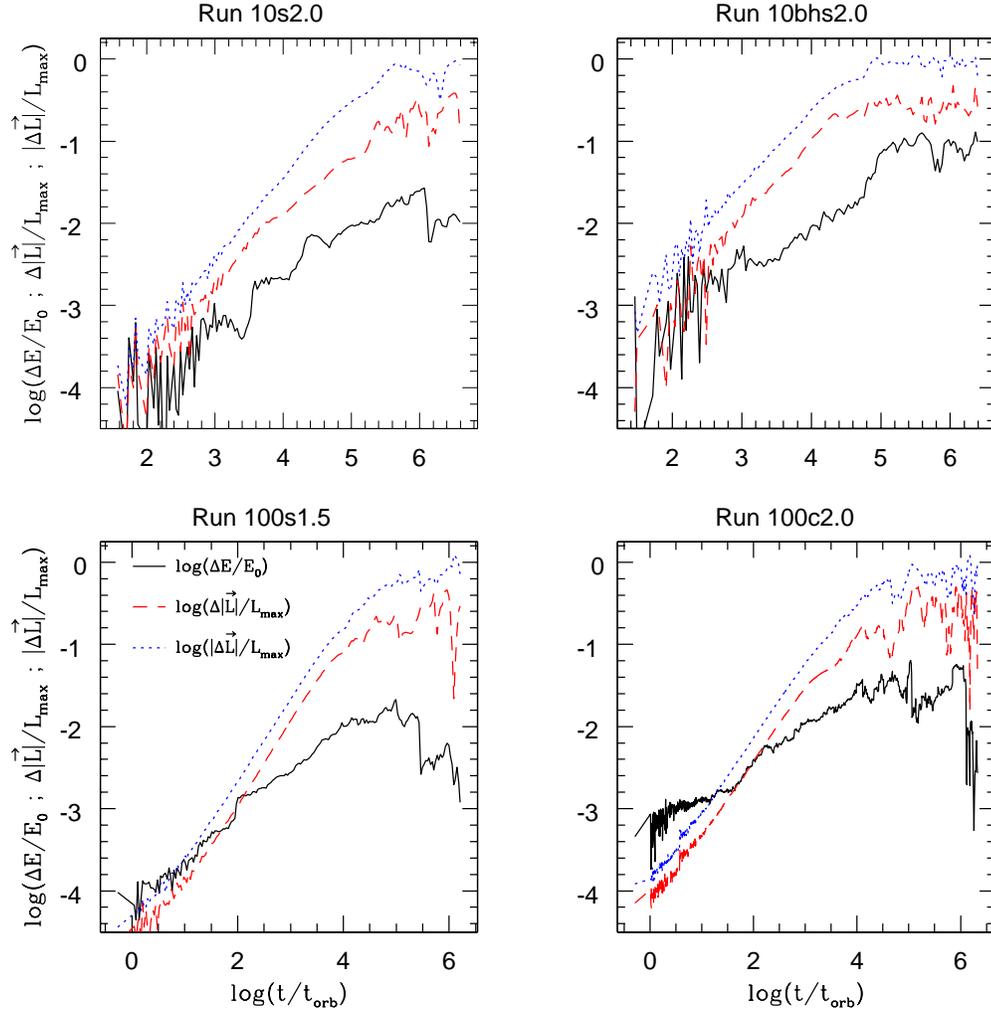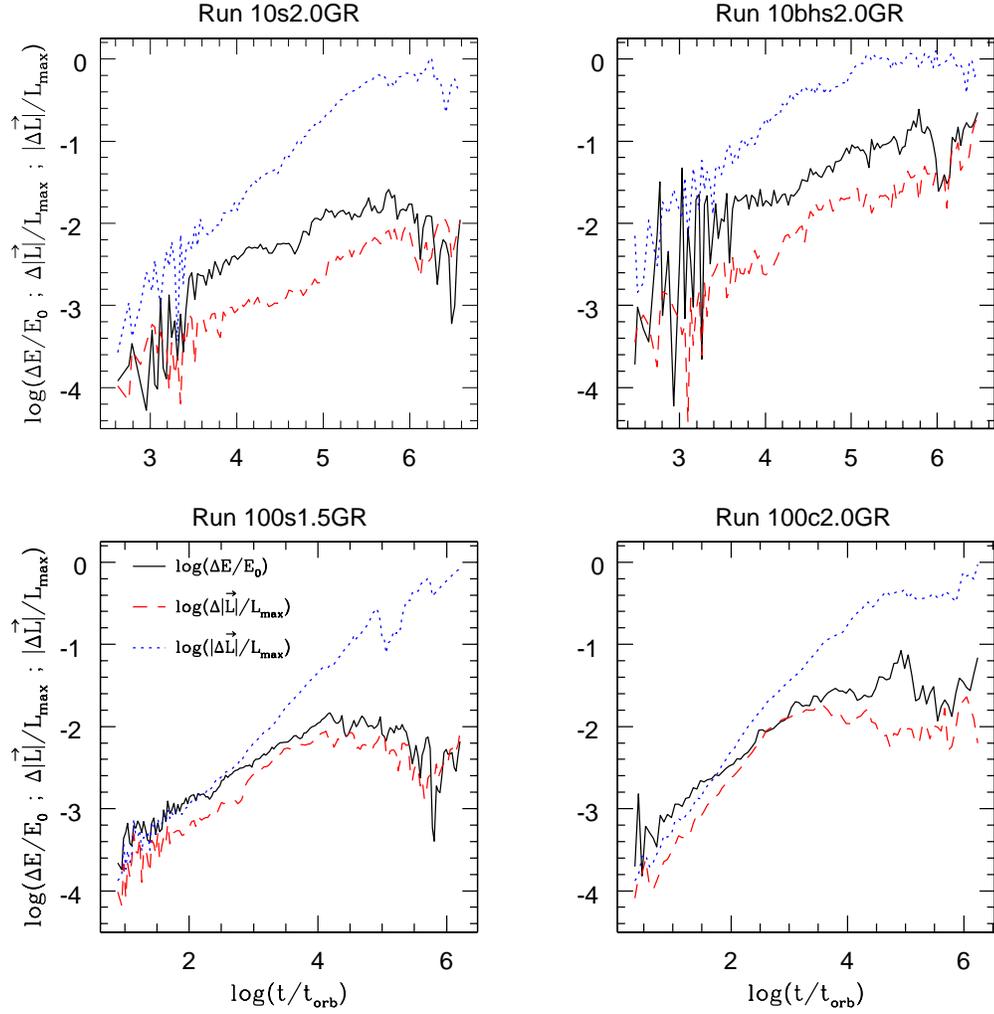
Figure 2.3: The evolution of the energy (black, solid line), scalar angular momentum (red, dashed line), and the vector angular momentum (blue, dotted line) for an identical set of four simulations as in Fig. 2.2 except for the addition of the first Post-Newtonian correction to the potential. Qualitatively, we can clearly see that the scalar angular momentum now mimics the evolution of the energy, rather than the vector angular momentum as it did in the purely Newtonian simulations.
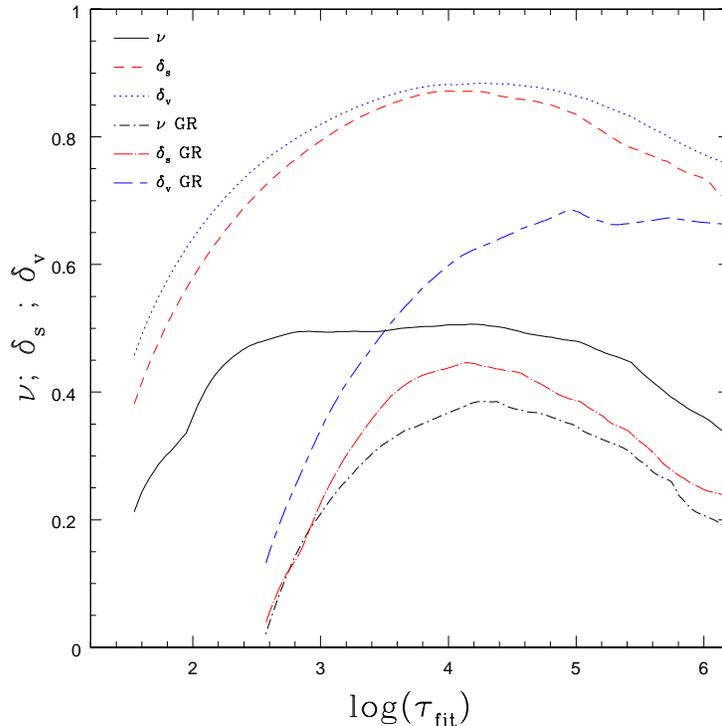
Figure 2.4: Evolution of the slope of the fractional change in energy ($\nu$), scalar angular momentum ($\delta_s$), and vector angular momentum ($\delta_v$) for simulation 100s1.5 and its GR counterpart, 100s1.5GR. Each slope is calculated from the beginning of the simulation to the value of $\tau_{fit}$ listed on the bottom axis.

Newtonian runs rise to $\sim 0.85$, which is lower than the 1.0 that we might expect from purely coherent growth, but still clearly distinct from the maximum values attained by $\nu$, which never rises much above 0.5. After reaching its maximum value, each scalar or vector angular momentum curve begins to decline for $t \gtrsim t_{prec}$ or $t \gtrsim t_{prec}^L$, respectively. Table 2.4 lists these maximum slope values along with the value of $\tau$ for which each was realized. In the Newtonian simulations, we see good agreement between these values and $t_{prec}$, as expected.

Comparing the two plots, we see several differences that can be traced to the
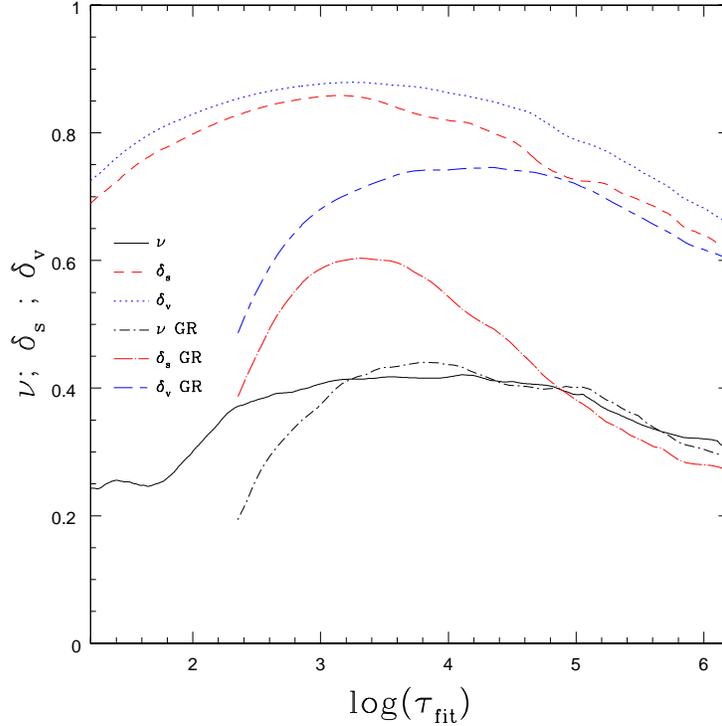
Figure 2.5: Linear fits to simulations 100c2.0/100c2.0GR as in Fig. 2.4. We note that the maximum slope of the angular momentum rises to $\sim 0.6$, suggesting that resonant relaxation may still play a role farther from the MBH.

particular initial conditions in each simulation. The peaks in both $\delta_s$ and $\delta_v$ are shifted to the right (corresponding to a longer period of coherence) in Fig. 2.4 due to the larger ratio of $M_\bullet/m_*$. We also note that the curve depicting $\delta_s(\tau)$ for simulation 100c2.0GR shows some evidence of resonant relaxation as it rises to $\sim 0.6$ at $\tau \sim 2 \times 10^3$, which is $\sim t_{prec,GR}$ for a typical object in the simulation. Because this simulation is spread out among a volume 8 times larger than in simulation 100s1.5GR ($a_{max} = 200$ AU instead of 100 AU), the mean timescale for pericenter precession is greater by a factor of 2. Longer periods of coherent torques leads to
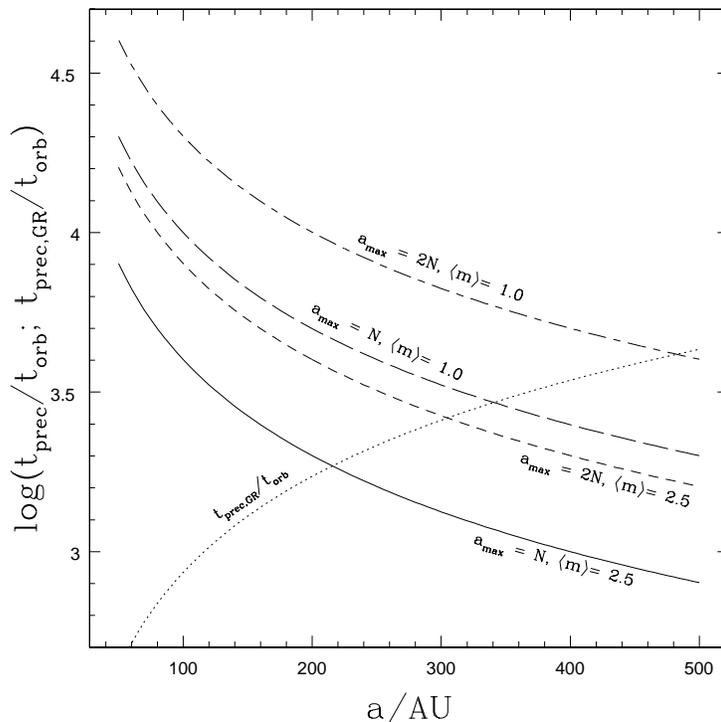
Figure 2.6: Relevant mass and GR apsis precession timescales as a function of radial distance from the MBH, and in the case of $t_{prec}$, the particular details of the mass distribution. Too close or far from the MBH one of these sources of precession will quench resonant relaxation.

more efficient RR, and we anticipate that further increases in the simulation volume would lead to a continuation of this effect.

Fig. 2.6 plots the both $t_{prec}$ and $t_{prec,GR}$ as a function of semimajor axis for a variety of the models we used in the first group of simulations. Very far from the MBH, the accumulation of other enclosed masses will induce significant precession; similarly, too close to the MBH we see rapid GR pericenter precession. Fig. 2.6 and the results of simulation 100c2.0GR suggest that there may be a middle ground where $t_{prec} \sim t_{prec,GR}$, and neither is low enough to prohibit some enhancement of

Table 2.6: Relaxation Properties of Five of Our 50-Object Simulations

| Sim | $t_{final}$ (yr) | $\left(\frac{\Delta E}{E_i}\right)_{pred}$ | $\langle\frac{\Delta E}{E_i}\rangle$ | $\langle\frac{|\Delta L|}{L_{max}}\rangle$ | Error (E) | Error (L) |
|---|---|---|---|---|---|---|
| 1 | $1.5 \times 10^5$ | 0.07 | 0.20 | 0.24 | $5.3 \times 10^{-4}$ | $10^{-2}$ |
| 2 | $5.3 \times 10^5$ | 0.13 | 0.30 | 0.27 | $5.8 \times 10^{-5}$ | $10^{-2}$ |
| 3 | $7.0 \times 10^5$ | 0.15 | 0.45 | 0.32 | $4.2 \times 10^{-5}$ | $10^{-2}$ |
| 4 | $9.2 \times 10^5$ | 0.17 | 0.45 | 0.26 | $-1.0 \times 10^{-4}$ | $10^{-2}$ |
| 5 | $1.0 \times 10^6$ | 0.18 | 0.37 | 0.32 | $-5.1 \times 10^{-6}$ | $4 \times 10^{-3}$ |

scalar angular momentum relaxation. In fact, given Eq. 2.10, it is possible for a partial cancellation to lead to even less orbital precession than either process alone in some parts of the system. This realization suggested that exploring larger volumes would be necessary to determining the full impact of RR on the EMRI rate for our second set of simulations.

## 2.4.2 Second Set of Simulations

Our second set of simulations were geared towards making a reasonable estimation of the EMRI rate, so we will focus on that rather than zeroing in on RR as in the previous section. As such, we aimed to balance getting maximum integration time with the error accumulations described in Sec. 2.3.2. Tab. 2.5 lists the average time for which we were able to integrate before reaching our predetermined fractional error threshold of $10^{-2}$. Although we had hoped to get to around $10^6$ yr for each of the simulations, we actually terminated them at about half of that value on average. There was significant variation in the integration time lengths in both the 50 and 100-object simulations - a few of them were cut off at $\sim 1 \times 10^5$ yr, while a few others made it all the way to $10^6$ yr while only accumulating fractional errors of a few $\times 10^{-3}$. In total, we had just over $10^7$ yr of integration time.

The overall evolution of our systems occurred significantly faster than our ex-

pectations. The relaxation time of our systems as given by Eq. 2.2 is a few $\times 10^7$ yr for our 50-object simulations, and twice as long for our 100-object simulations. We calculated the average fractional change in $E$ and $L$ as in Eq. 2.1 for the objects in our simulations and compared them to the expected values; the results are shown in Tab. 2.6 for the first group of 5 50-object simulations from Tab. 2.5.

In the case of both the angular momentum and the energy, the relaxation is taking place at a rate that is significantly faster than predicted. Despite the comparatively higher errors accumulated in the angular momentum, its evolution more closely matches our expectations, while the energy relaxation is greater still across the board. This does, however, seem to confirm our assessment that resonant relaxation is not a dominant physical process, as the changes in $L$ are clearly not dominant over the changes in $E$.

Since the total energy and angular momentum of our systems are reasonably well-conserved, it seems likely that the error from Sec. 2.3.2 is artificially enhancing the relaxation via the small kicks given to the other orbiting objects during a close pericenter passage. These seem to not have a significant impact on the total energy conservation, as we can see that it is several orders of magnitude better than the angular momentum conservation.

We do note that we ran one simulation that was a purely Newtonian analog to those in Tab. 2.6, and the energy relaxation was also significantly greater than we would expect from Eq. 2.2. Possibly this is an indication that our initial assessment of the 2-body relaxation time is an overestimation. Still, we will have to keep this discrepancy in mind when attempting to estimate the EMRI rate - the spurious addition of relaxation to the system could have a significant positive effect on the rate by allowing more objects to change their orbits toward a lower semimajor axis (and thus a lower value of $t_{merge}$). As only one of the five simulations in Tab. 2.6
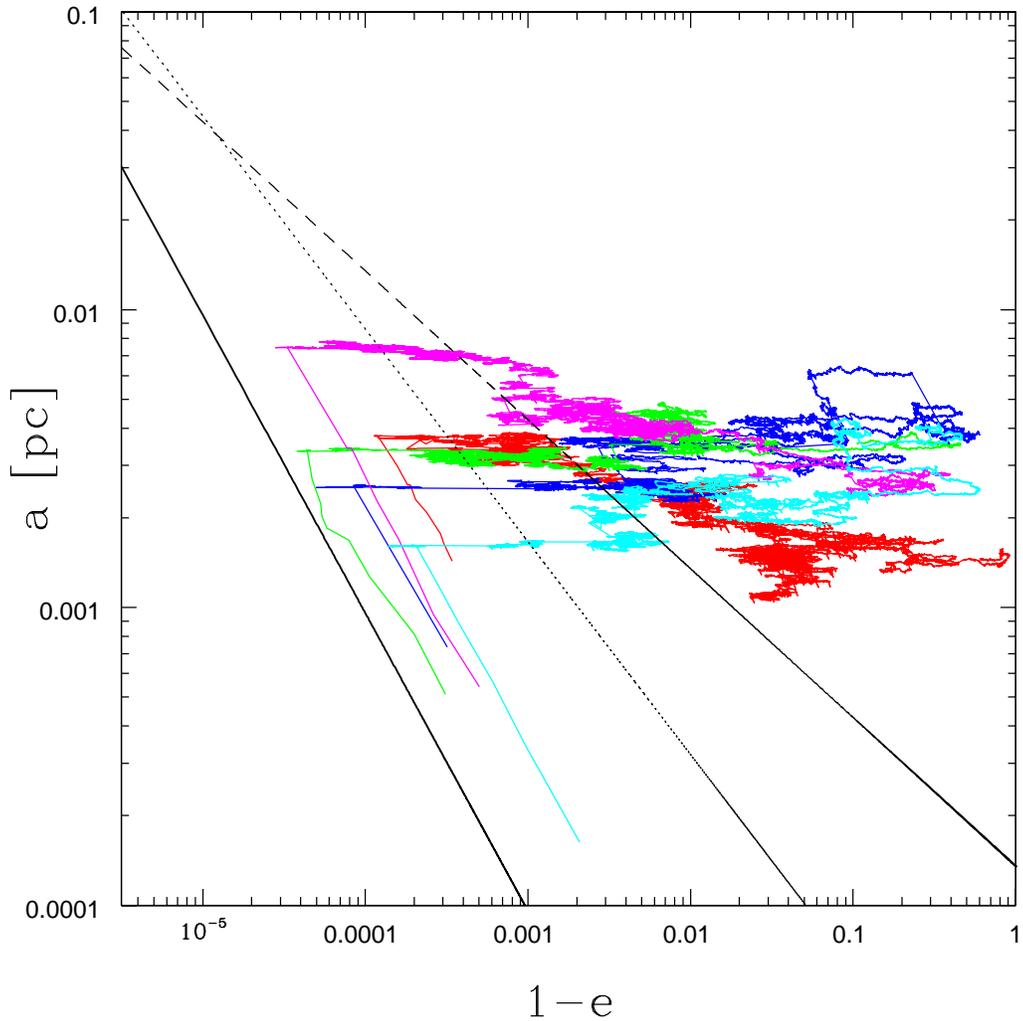
Figure 2.7: Evolutionary tracks in $a-e$ space of the 5 objects that crossed the Schwarzschild barrier (dashed black line), the critical eccentricity line (Eq. 2.7 with $C_{EMRI} = 0.1$, dotted black line), and became merger events before hitting the plunge line (solid black line).

resulted in an EMRI, this also provides further evidence that objects can cause problems prior to reaching low enough pericenters to merge.

In total, six objects in our simulations crossed the Schwarzschild barrier; the

Table 2.7: Orbital Properties of the EMRI-event Objects.

| $m/M_\odot$ | $a_i$/AU | $e_i$ | $t^L_{rlx,i}$/yr | $t_{merge}$/yr | $a_{SB}/AU$ | $a_f$/AU | $e_f$ | $r_{p,f}/(GM/c^2)$ |
|---|---|---|---|---|---|---|---|---|
| $50^1$ | 784 | 0.398 | $2.56 \times 10^7$ | $6.0 \times 10^5$ | 519 | 26.3 | 0.9981 | 4.8 |
| 50 | 301 | 0.387 | $1.60 \times 10^7$ | $7.4 \times 10^5$ | 769 | 257.0 | 0.9996 | 10.2 |
| $25^1$ | 736 | 0.894 | $1.18 \times 10^7$ | $3.1 \times 10^5$ | 689 | 51.5 | 0.9994 | 3.1 |
| $25^1$ | 735 | 0.750 | $2.57 \times 10^7$ | $4.9 \times 10^5$ | 342 | 9.7 | 0.9930 | 6.8 |
| 25 | 595 | 0.970 | $3.13 \times 10^6$ | $4.5 \times 10^5$ | 1602 | 46.5 | 0.9988 | 5.6 |

———————————————

Note. — The objects with a superscript 1 were integrated relatively longer prior to being removed from their respective simulations. This came as a result of the changing the threshold in ratio between merger time and relaxation time to 25 from 100.

orbital evolution of the five that became EMRI events is shown in Fig. 2.7. All six objects flirted with the Schwarzschild boundary for a while, crossing briefly back a few times as their orbital parameters were jostled by 2-body relaxation. Further detail about the 5 objects that became EMRIs is given in Tab. 2.7. Although not included in the table, each of them crossed the barrier with $e \gtrsim 0.999$, as expected. For comparison's sake, we have plotted the tracks of six random objects from one of the 50-object simulations in Fig. 2.8 - we can see that none of them approaches the barrier.

The barrier penetrations that we see in our simulations occur where we expected them. The $6^{th}$ column of Tab. 2.7, $a_{SB}$, denotes the semimajor axis at which the object penetrated the Schwarzschild barrier for the final time. We note that all but one of them crossed at a significantly lower value of $a$ than we originally predicted in Eq. 2.30, but in good agreement with both the minimum value given in Eq. 2.31 and with the distribution of semimajor axes for barrier penetrations given in Merritt et al. (2011). After successfully crossing the barrier, each of the five colored lines made their way across the critical eccentricity line (Eq. 2.7 with $C_{EMRI} = 0.1$, dotted black line), and eventually began losing energy and angular momentum and
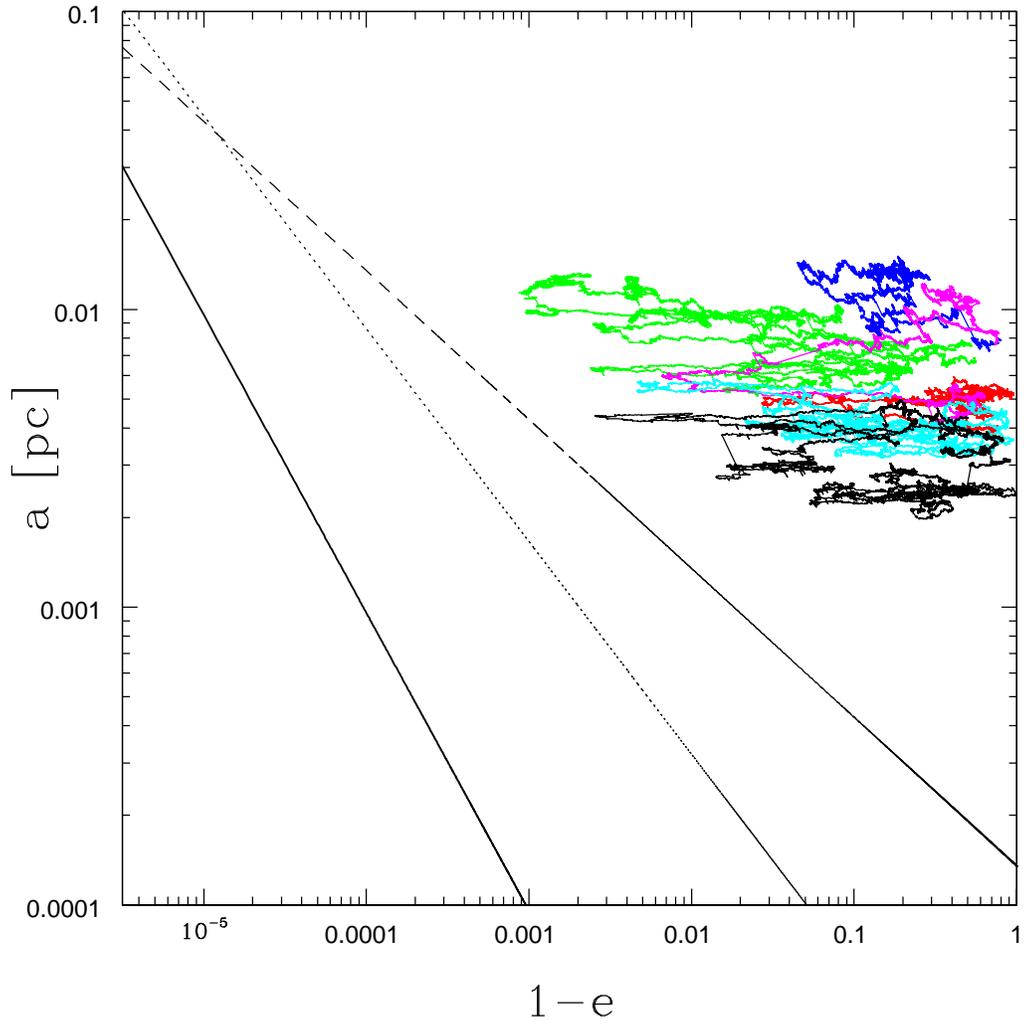
Figure 2.8: For comparison with Fig. 2.7, we plot the orbital evolution of six normal objects from one of our 50-object simulations. As in Fig. 2.7, also depicted are the Schwarzschild barrier (dashed black line), the critical eccentricity line (dotted line), and the plunge line (solid black line).

were removed from the simulations.

The results of our simulations differed from our expectations in one significant way. Hopman & Alexander (2005) find that the majority of EMRI candidates originate from the outer edge of our simulation volume (or even outside of it) with highly eccentric orbits. Instead, we found that all of our eventual mergers originated within the inner third of our range of $a$, and only one began its existence with a large eccentricity. This provides us with two questions - why we do not see their population of EMRI candidates, and why they do not see ours.

We can think of a few possible explanations for the first discrepancy. Because the simulations from Hopman & Alexander (2005) and others were not done using a direct N-body code, they were able to model the entire radius of influence - the finite extent of our simulations may be preventing us from including all of the relevant forces. These objects are on the outer boundary of our simulation and would, in reality, experience forces due to interactions with objects with $a \gtrsim 2000 AU$ that we were unable to include. If this is indeed partially responsible, we might expect mergers from this population in addition to (rather than instead of) those that we are seeing in our simulations. It is also possible that, being the farthest from the MBH (and thus having the smallest velocities in the system), our outer objects are most affected by the unphysical kicks delivered by our code problems. One could imagine that this is somehow preventing them from attaining high enough eccentricities to approach the critical eccentricity threshold.

We suspect that the simulations in the literature do not find mergers like those we see in our simulations because their approximate methods cannot include all of the relevant physics. While the results of this work and Merritt et al. (2011) both suggest that the Schwarzschild barrier will prevent resonant relaxation from having a large impact on the EMRI rate, it may still have a nontrivial impact by allowing
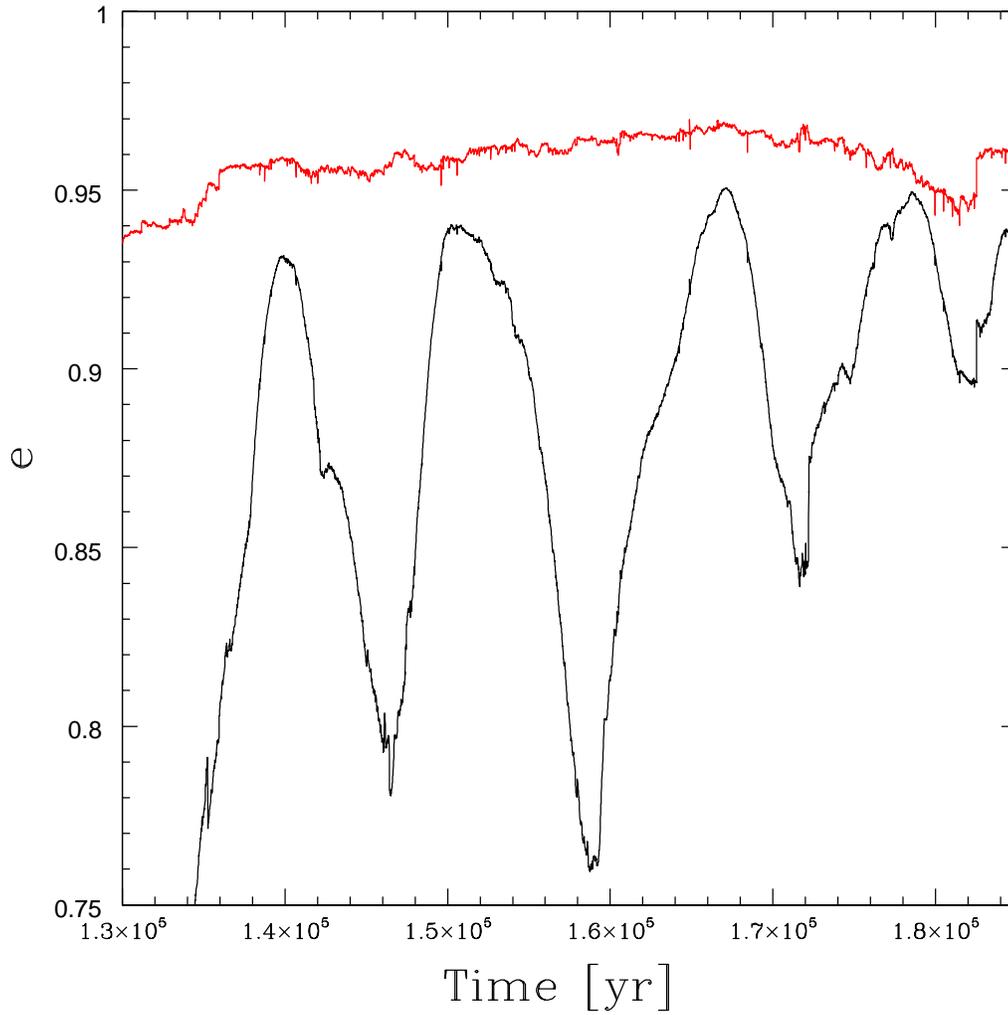
Figure 2.9: Variation in the eccentricity (black line) of an object near the Schwarzschild barrier (red line) due to the "bounce" effect of Sec. 2.2.3. While the background torque remains constant, the changing angle of the orbital eccentricity vector due to apsis precession varies the torque on the orbit in such a way to alternately lower and raise the angular momentum, causing an oscillation.

objects to oscillate near the barrier, giving them multiple opportunities to cross and eventually merge. Given the slow rate at which 2-body relaxation will create highly eccentric orbits when $a < 1000$ AU, this could still provide a significant boost.

Fig. 2.9 shows the angular momentum oscillations experienced by one of our objects (black line) near the predicted Schwarzschild barrier (red line, Eq. 2.24). The average period time peaks comes out to around $1.3 \times 10^4$ yr; this is slightly greater than the timescale for the object's precession due to GR at its maximum value in eccentricity, which is about $9 \times 10^3$ yr. We expect it to be somewhat greater, since the object's precession will be, on average, slower than its value at the eccentricity maximum. This agreement provides strong evidence that this "bounce" effect is responsible for these oscillations.

Even if a barrier crossing is unlikely for each time an object is brought near the boundary, one could imagine that this would still provide an enhancement to the rate of EMRIs from objects at fairly low semimajor axis. We suspect this might explain the difference between our results and those from previous simulations in the literature. However, again we must note that since we do not know all of the impacts of spurious energy and angular momentum relaxation described earlier in this Section, we cannot rule out the possibility that they are responsible for this discrepancy.

### 2.4.3    Conclusions About the EMRI Rate and Orbital Parameters

As our original goal in undertaking this project was to better constrain the EMRI rate and possibly make a statement about the orbital elements of likely merger objects, we now endeavor to interpret our results in light of that goal. The overall rate of mergers derived from our simulations is around $4 \times 10^{-7} \text{yr}^{-1}$ per galactic

Table 2.8: Final Eccentricities of EMRI Objects At $P_{LISA}$

| $a_f$/AU | $e_f$ | time to EMRI (yr) | $e_{EMRI}$ |
|---|---|---|---|
| 26.3 | 0.9981 | 100.7 | 0.896 |
| 257.0 | 0.9996 | 664.2 | 0.795 |
| 51.5 | 0.9994 | 4.4 | 0.935 |
| 9.7 | 0.9930 | 25.3 | 0.860 |
| 46.5 | 0.9988 | 32.6 | 0.885 |

Note. — All objects finish with a semimajor axis of $a_{LISA} = 0.465$ AU.

center. Despite the myriad of differences between both the nature of the simulations we performed, and the nature of the actual mergers we observed in our simulations, the rate we derive is comfortably within the range derived in the literature ($10^{-6} - 10^{-8}\mathrm{yr}^{-1}$ per galactic center).

Our initial conditions were designed to reasonably replicate the mass density distribution that we expect to find at a typical galactic center, although it is quite likely to be divided among more objects. With the caveat that our numbers are small and thus subject to random fluctuations, we note that spreading the mass over twice as many objects in our simulations did not result in a decrease in the rate (actually, it went up from $2.2 \times 10^{-7}$ to $9.7 \times 10^{-7}\mathrm{yr}^{-1}$). While we surely cannot use our limited sample to suggest that extrapolation to further spreading of the mass distribution will continue to increase the EMRI rate, it seems likely that it will not systematically decrease it.

Due to the fact that our simulations revealed a different class of merging objects from the literature, we expect significantly different orbital elements for these objects when they reach the LISA detection threshold ($P_{LISA} \sim 10^4$ sec, corresponding to an orbital semimajor axis of $a_{LISA} = 0.465AU$). As we removed our merger objects from the simulations prior to this level of energy loss (mostly for computational

convenience), our final values for the semimajor axis and eccentricity of the orbits are not necessarily representative of those that would be viewed by LISA. In an attempt to make our results more useful for this purpose, we used the Peters (1964) equations to integrate our final orbital elements forward in time until the period of orbit reached $P_{LISA} \approx 10^4$ sec. The results of these integrations are given in Tab. 2.8. While all of our objects were removed from the code with high orbital eccentricities, they exhibited a wide range of semimajor axes. This translates to a fairly large range in eccentricities at the point of the LISA detection threshold $(0.8 - 0.93)$.

Unfortunately, our limited integration time has prevented us from recording more events, and it is unlikely that we have a enough for a statistically meaningful sample. However, the fact that we are probing a population of mergers that is significantly different from the previous results is likely a step in the right direction. As we pointed out in Sec. 2.4.2, our Schwarzschild barrier crossings were very consistent with those observed in Merritt et al. (2011), suggesting that our results are reasonable despite the potential pitfalls created by our code errors.

We also note in passing that our criteria for establishing that an EMRI has taken place are different from those used by Merritt et al. (2011): an instantaneous separation of $r \leq 8GM/c^2 \approx 0.08$ AU and a semimajor axis of $a_{merger} \leq 2.0$ AU. They record anything with the critical separation but not low enough semimajor axis as a plunge. By these criteria, it is possible that some of our merger events would have been recorded as plunges. However, given that we did not use HNDrag for the entirety of our integrations due to the significant increase in computation time associated with including the radiation reaction terms, it is unclear exactly what would have happened if these objects were allowed to shed energy and angular momentum during the entirety of their time across the Schwarzschild barrier.

All in all, our results, while limited in nature, do indicate that a significant population of mergers is possible with semimajor axes well below previously predicted values. This population of EMRI events continues to exist as the mass in our simulations is spread amongst twice the number of objects. While we do not see mergers in our simulations with $a \sim .01$ pc, these objects are on the boundary of our simulation volume and may not be properly handled due to edge effects. As such, it is possible that this new population of events will add to (rather than take the place of) previous estimations of the rate when computational advances allow simulations of a larger number of objects.

After the original draft of this document, further research was done. The problem causing the spurious accumulation of angular momentum errors was located and removed, and simulations were performed with the new code. The details of the changes and new results are given in Appendix C

# Chapter 3

# The Impact of an Intermediate-Mass Black Hole on Mass Segregation in Star Clusters

## 3.1 Introduction

In this Chapter, we shift our attention from the MBHs at the center of galaxies to the possibility of finding intermediate-mass black holes (IMBHs) that are less massive than MBHs, but still much greater than stellar-mass. While they are not gravitationally dominant to the extent that a MBH is over the central $\sim$ 1pc at the center of a galaxy, IMBHs, with likely masses that are $\sim$ 1% of the total cluster mass, still have considerable influence on the dynamics of their host.

Previous work has focused on global properties that are easily observable, such as the core radius and the surface brightness profile, as a way to distinguish clusters with an IMBH from those without. In this Chapter, we examine a different influence that an IMBH exerts on its host - limiting the amount of mass segregation

that occurs, even in visible main sequence stars. We present the results of a host of modern N-body simulations, and in doing so build a theoretical framework for applying this technique to Galactic globular clusters.

## 3.2 Numerical Simulations

The numerical simulations presented in this paper have been carried out with a state-of-the-art direct N-body code for star cluster dynamics, NBODY6 (Aarseth 2003). NBODY6 has been modified as discussed in Trenti et al. (2007a) to improve accuracy in the presence of an IMBH, and uses regularization of close gravitational encounters without any softening. This makes it optimal to follow interactions within the sphere of influence of the IMBH.

### 3.2.1 Units and timescales

NBODY6 uses the standard system of units of Heggie (1986) in which $G = M = -4E_T = 1$, where G is the gravitational constant, M is the total mass and $E_T$ is the total energy of the system. In this system of units, the half-mass relaxation time, which is the relevant timescale for mass segregation and energy equipartition is defined as follows (Spitzer 1987):

$$t_{rh} = \frac{0.138 N r_h^{3/2}}{\ln(0.11N)},$$

(3.1)

where $N$ is the number of stars in the system and $r_h$ is the half-mass radius. In physical units, $t_{rh}$ can be expressed as (Djorgovski 1993):

$$t_{rh} = \frac{8.9 \cdot 10^5 yr}{\ln(0.4N)} \times \left(\frac{1 M_\odot}{\langle m_* \rangle}\right) \times \left(\frac{M}{1 M_\odot}\right)^{0.5} \times \left(\frac{r_h}{1pc}\right)^{1.5},$$

(3.2)

where $\langle m_* \rangle$ is the average mass of a star.

### 3.2.2 Initial conditions

Galactic GCs are made of some of the oldest stars in our galaxy (e.g., see Krauss & Chaboyer 2003) and are collisionally relaxed systems. Their two-body half-mass relaxation times $t_{rh}$ are shorter than their age (e.g., see Heggie & Hut 2003), thus their initial conditions are largely unknown. However, the evolution on a relaxation timescale is only weakly dependent on the initial configuration as the system evolves toward a self-similar configuration where the density and light profiles are determined primarily by the efficiency of kinetic energy production in the core due to gravitational encounters (Trenti et al. 2007a,b; Vesperini & Chernoff 1994). In this paper, we explore a number of different initial configurations, varying the initial mass function, the initial density profile, the strength of the galactic tidal field, and the fraction of primordial binaries to verify that the evolution of the system is indeed independent of the initial configuration. The initial density profile is always that of a single-mass King (1966) model, but we use a full mass spectrum in the N-body calculations. The number of particles is varied from $N = 8192$ to $N = 32768$ to quantify the evolution of mass segregation with and without an IMBH. The details of our runs are reported in Table 3.1.

Initial stellar masses were drawn from either a Salpeter (1955) or Miller & Scalo (1979) initial mass function (IMF, hereafter), that is:

$$\xi(m) \propto m^{\alpha}, \tag{3.3}$$

with $\alpha = -2.35$ and $m \in [0.2 : 100]M_\odot$ for the Salpeter IMF, while for the Miller & Scalo IMF the power law slope is the following: $\alpha = -1.25$ for $m \in [0.2 : 1]M_\odot$, $\alpha = -2.0$ for $m \in [1 : 2]M_\odot$, $\alpha = -2.3$ for $m \in [2 : 10]M_\odot$, $\alpha = -3.3$ for $m \in [10 : 100]M_\odot$. In addition, we have also carried out control runs that extend the IMF down to $0.1M_\odot$, as such stars exist in GCs, but are not bright enough to

be detected in most of the cluster.

We handled stellar evolution by assuming a turnoff mass $M_{T.O.} = 0.8 M_\odot$, and instantaneously reducing all stars to their final state at the beginning of the simulation. Stars with masses $0.8 M_\odot \leq m < 8.0 M_\odot$ were assumed to become white dwarfs and reduced to a final mass as prescribed in Hurley et al. (2000). Stars in the ranges $8.0\text{-}25.0 M_\odot$ and $25.0\text{-}100.0 M_\odot$ became neutron stars (unity retention fraction assumed) and black holes, and were reduced linearly to $1.3\text{-}2.0 M_\odot$ and $5\text{-}10 M_\odot$, respectively. Our model makes the approximation that most of the relevant stellar evolution occurs on a timescale shorter than a relaxation time. This choice is appropriate to model the dynamics of an old GC on a relaxation timescale with only a limited number of particles and is more realistic than using an unevolved mass spectrum appropriate for young star clusters when $N \lesssim 30000$ (Trenti et al. 2008).

In addition, about half of our runs included primordial binaries, an important component of many GCs (e.g., see Pulone et al. 2003) that can influence the evolution of mass segregation. In fact, binaries are on average twice as massive as singles and thus tend to segregate in the core of the system (e.g., see Heggie et al. 2006). We define the fraction of binaries to be

$$f_b = n_b/(n_s + n_b) \tag{3.4}$$

where $n_s$ and $n_b$ are the initial number of single stars and binaries, respectively. Thus, a run with $N = n_s + n_b = 8192$ and $f_b = 0.1$ actually has $8192 + 819 = 9011$ objects. As the dynamical influence of binaries tends to saturate for $f_b \approx 0.1$ (Heggie et al. 2006; Vesperini & Chernoff 1994), all our runs with primordial binaries have $f_b = 0.1$, a number similar to the observed binary fraction of many old GCs (e.g., Albrow et al. 2001). Binaries were initialized as in Heggie et al. (2006), i.e. from a flat distribution in binding energy from $\epsilon_{min}$ to $133\epsilon_{min}$, with $\epsilon_{min} = \langle m_* \rangle \sigma_c(0)$.

Here, $\sigma_c(0)$ is the initial central velocity dispersion of the cluster.

To half of the simulations, we added an IMBH with mass $M_{IMBH} \approx 0.01$ ($\approx 1\%$ of the entire cluster), the same ratio as a $\sim 10^3 M_\odot$ black hole would have to a GC of mass $10^5 M_\odot$. In some of the simulations (see Tab. 3.1), we increased the mass of the IMBH to study the dependence of mass segregation on this parameter.

All objects in our runs were treated as point masses, thus neglecting stellar evolution and collisions as well as any growth of the IMBH due to accretion of tidally disrupted stars. These effects have only a minor influence on the late-time dynamics of the cluster, since actual collisions are rare after massive stars have evolved, and accretion onto the IMBH is minimal (e.g. see Baumgardt et al. 2004).

The evolution of the clusters includes the tidal force from the parent galaxy, assuming circular orbits with radii such that the tidal cut-off radius is self-consistent with the value of the King parameter $W_0$ used. The galactic tidal field is treated as that due to a point mass, and the tidal force acting on each particle is computed using a linear approximation of the field. Particles that become unbound are removed from the system. For full details of the tidal field treatment see Trenti et al. (2007b).

For validation purposes, we also analyzed a few snapshots from three runs with $N = 131072$ carried out by Baumgardt & Makino (2003) and by Baumgardt et al. (2004) with and without a central IMBH, kindly made available by the authors. These runs include full stellar evolution using the Hurley et al. (2000) tracks, but no primordial binaries. In addition, accretion of tidally disrupted stars onto the IMBH is included. The initial star positions and velocities from these runs were also drawn from a King model with $W_0 = 7.0$, but instead the mass spectrum was drawn from a Kroupa (2001) IMF, with $\alpha = -1.3$ for $m \in [0.1 : 0.5]M_\odot$ and $\alpha = -2.3$ for $m > 0.5 M_\odot$. The upper cut-off mass was $15 M_\odot$ for run 128kk.1, $30 M_\odot$ for run 128kkbh.1a, and $100 M_\odot$ for run 128kkbh.1b. These snapshots provide us with a

control group against which we can test the validity of our own models, and also allow us to probe the extrapolation of our results to higher N.

## 3.3 Results

### 3.3.1 Overall evolution of the star clusters

A star cluster with single stars only and no central IMBH evolves toward core collapse within a few relaxation times. The collapse is eventually halted when the central density is high enough to dynamically form binaries. At this stage gravothermal oscillations set in and the density profile of the cluster remains self-similar until the final stages of tidal dissolution of the system. The existence of either primordial binaries or an IMBH serves as an energy source to counteract the collapse, resulting in a more significant core (Trenti et al. 2007a). This is confirmed in all models (for example, see Fig. 3.1 for the evolution of the core and half mass radius in our 32k simulations). Here, we use the Casertano & Hut (1985) definition of the core radius, namely

$$r_c = \frac{\sum_{i=1}^{N} r_i \rho_i m_i}{\sum_{i=1}^{N} \rho_i m_i},$$ (3.5)

where $m_i$ is the mass of the $i$th star, $r_i$ is its from the cluster center of mass, and the density $\rho_i$ around each particle is calculated using the distance to the fifth closest neighbor.

As expected from previous investigations based on equal mass particles (Trenti et al. 2007b), the density profile of our clusters progresses to a self-similar configuration, which is independent of the initial configuration of the stars and the IMF. This independence justifies our treatment of stellar evolution at the beginning of the simulations, and provides further evidence of the erasure of initial conditions after a few relaxation times. The overall evolution of star clusters with and without an

Table 3.1: Summary of the initial globular cluster N-body simulations.

| Name | N | $M_{IMBH}/M_{tot}$ | $M_{IMBH}/M_\odot$ | $f_b$ | $\langle\Delta\langle m\rangle\rangle$ | $\Delta\langle m\rangle_{min}$ | $\Delta\langle m\rangle_{max}$ |
|---|---|---|---|---|---|---|---|
| 8ks | 8192 | N/A | N/A | 0 | 0.07 | 0.040 | 0.112 |
| 8km | 8192 | N/A | N/A | 0 | 0.13 | 0.095 | 0.167 |
| 8kbs5 | 8192 | N/A | N/A | 0.1 | 0.09 | 0.029 | 0.138 |
| 8kbs | 8192 | N/A | N/A | 0.1 | 0.10 | 0.071 | 0.143 |
| 8kbs11 | 8192 | N/A | N/A | 0.1 | 0.09 | 0.037 | 0.116 |
| 8kbm | 8192 | N/A | N/A | 0.1 | 0.09 | 0.048 | 0.130 |
| 16ks | 16384 | N/A | N/A | 0 | 0.11 | 0.071 | 0.158 |
| 16ks.1 | 16384 | N/A | N/A | 0 | 0.14 | 0.112 | 0.191 |
| 16km | 16384 | N/A | N/A | 0 | 0.14 | 0.112 | 0.174 |
| 16kbs | 16384 | N/A | N/A | 0.1 | 0.09 | 0.060 | 0.140 |
| 16kbm | 16384 | N/A | N/A | 0.1 | 0.10 | 0.067 | 0.127 |
| 32km | 32768 | N/A | N/A | 0 | 0.14 | 0.108 | 0.161 |
| 128kk.1 | 131072 | N/A | N/A | 0 | 0.13* | N/A | N/A |
| 8ksBH | 8193 | 0.03 | 104.0 | 0 | 0.05 | 0.014 | 0.091 |
| 8kmbh | 8193 | 0.01 | 42.1 | 0 | 0.07 | 0.036 | 0.121 |
| 8kmBH | 8193 | 0.03 | 129.3 | 0 | 0.06 | 0.011 | 0.097 |
| 8kbsBH | 8193 | 0.03 | 114.4 | 0.1 | 0.04 | -0.014 | 0.080 |
| 8kbmbh | 8193 | 0.015 | 69.5 | 0.1 | 0.04 | -0.021 | 0.079 |
| 16ksbh | 16385 | 0.015 | 103.1 | 0 | 0.05 | 0.023 | 0.090 |
| 16ksbh.1 | 16385 | 0.015 | 60.9 | 0 | 0.06 | 0.013 | 0.118 |
| 16kmbh | 16385 | 0.015 | 128.2 | 0 | 0.08 | 0.027 | 0.113 |
| 16kbsbh | 16385 | 0.01 | 113.4 | 0.1 | 0.04 | 0.015 | 0.078 |
| 16kbmbh | 16385 | 0.01 | 141.0 | 0.1 | 0.05 | 0.015 | 0.084 |
| 32kmbh | 32769 | 0.01 | 240.0 | 0 | 0.07 | 0.051 | 0.101 |
| 128kkbh.1a | 131072 | 0.013 | 1000.0 | 0 | 0.09* | N/A | N/A |
| 128kkbh.1b | 131072 | 0.009 | 1000.0 | 0 | 0.06* | N/A | N/A |

Note. — We calculated the average, maximum and minimum values for $\Delta\langle m\rangle$ (in solar mass units) between 5 and 12 relaxation times for each run. Starred values are not averages, but are from a single snapshot. The name of each run indicates:

- The number of stars in the simulation (8k, 16k, 32k or 128k)

- The presence of primordial binaries (b if $f_b > 0$)

- The IMF (m for Miller & Scalo, s for Salpeter, and k for Kroupa)

- The presence of an IMBH (absent for none, bh for small BH mass, and BH for larger - see also fifth column)

- The value of $W_0$ if different from 7.0

- Control run with IMF lower cut-off at $0.1 M_\odot$ (.1 suffix).
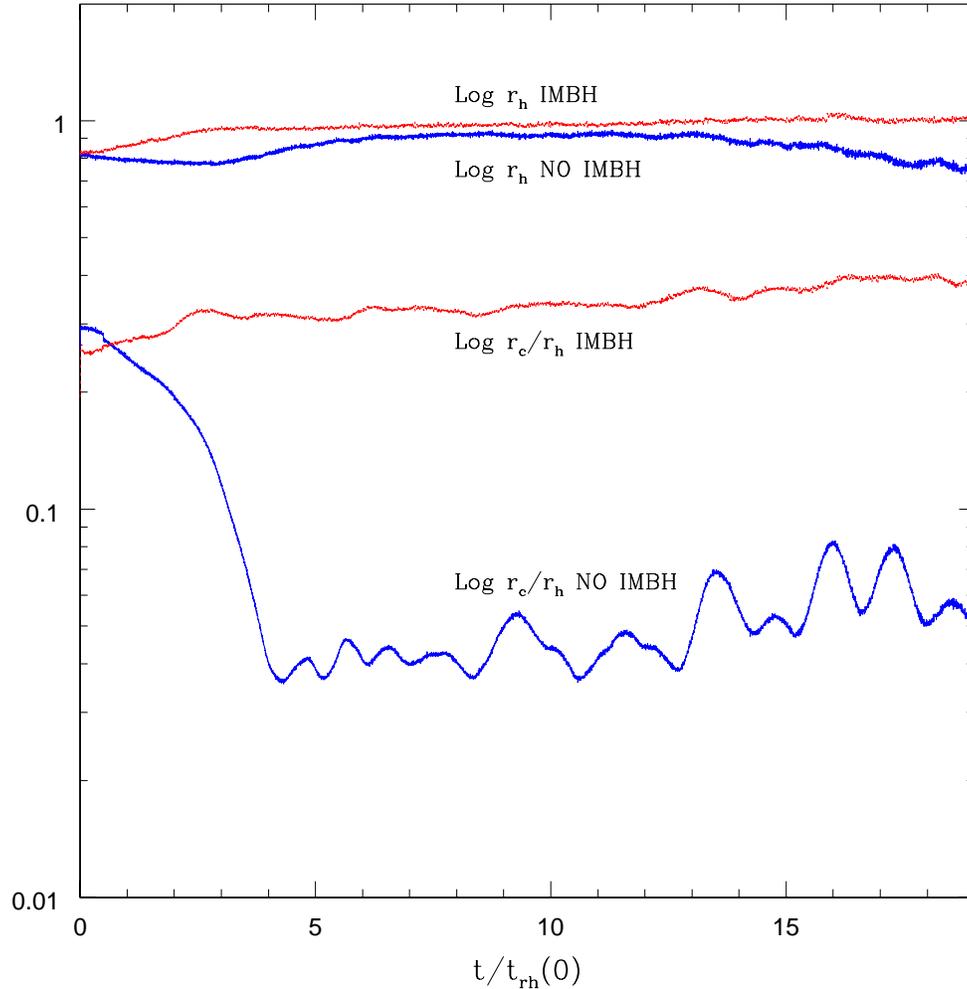
Figure 3.1: Evolution of the three dimensional half mass radius ($r_h$) and of the core to half mass radius ratio ($r_c/r_h$) in NBODY units for our $N = 32769$ simulations with (red curves) and without an IMBH (blue curves). The presence of an IMBH prevents core collapse. We have smoothed the curves by applying a triangular smoothing window of size $1.0 t_{rh}(0)$.

IMBH and/or primordial binaries has been discussed in the literature (Baumgardt & Makino 2003; Baumgardt et al. 2004; Fregeau & Rasio 2007; Heggie et al. 2006; Hurley 2007; Trenti et al. 2007a,b). Here we focus instead on a novel aspect that has a promising observational signature, namely the evolution of mass segregation for runs with an IMBH.

### 3.3.2 Mass segregation

As our overarching goal is to propose a viable observational test to identify a star cluster that is likely to harbor an IMBH, we took steps throughout our analysis to replicate observational data as closely as possible. We limited our analysis to data projected onto two dimensions, and excluded stellar remnants from our calculations of observationally accessible quantities. Most of our runs did not have stars with masses below $0.2M_\odot$, because these are generally too dim to detect with a high completeness. However, we did perform two 16k control runs with masses down to $0.1M_\odot$ to ensure that the presence of smaller, undetectable stars did not affect the mass segregation. For a proper comparison to the other runs, we did exclude the stars with masses between 0.1 and $0.2M_\odot$ from the calculation of the observationally accessible quantities for these runs.

Binary systems were handled by only including the brighter member in the analysis of the observationally accessible quantities. This choice is motivated by the fact that for real observations, masses will need to be estimated from luminosities. Since binaries in GCs are typically not resolved (the separations are below a few astronomical units for the range of binding energies considered), we observe mainly single sources. Because the luminosity of a main sequence star is highly sensitive to its mass ($L \sim M^{3.5}$ for stars around $1M_\odot$), the lighter star contributes very little to the overall luminosity in many cases, and thus the total luminosity will be very similar to that of the brighter member.

To quantify the effects of mass segregation, we examined the radial variations in average stellar mass — or equivalently — in the slope of the mass function (if the mass function is a power law in the mass range considered, then there is a one-to-one relation between the average mass and the slope). As a consequence of

energy equipartition, heavier particles sink to the center of the cluster within a few relaxation times, increasing the difference in average mass between the center and the halo of the cluster. As our main diagnostic of mass segregation, we define

$$\Delta\langle m\rangle = \langle m\rangle\ (r=0) - \langle m\rangle(r=r_{hm}) \tag{3.6}$$

where $r_{hm}$ is the projected half-mass radius of the cluster (computed using only visible stars), and $\langle m\rangle$ is the average mass for main sequence stars with $m \in [0.2 : 0.8]M_\odot$. Both of these measurements are taken from projected radial bins each containing 5% of the cluster's visible stars. Because nearly all of the deviation in $\langle m\rangle(r)$ occurs within this radial range, we are maximizing our baseline for measuring mass segregation while using fields with a reasonable number of stars. This definition also allows for a straightforward comparison to observational data as only two fields per cluster are sufficient.

Fig. 3.2 depicts the evolution of $\Delta\langle m\rangle$ for our $N = 16384$ to $N = 32768$ runs without primordial binaries. For each run, we analyze the configuration of the system every 15 Nbody units (which corresponds to more than 10 measurements per relaxation time). Runs with an IMBH are represented as red points, while runs without are blue points. Because they were drawn from single-mass King models, our clusters begin out of equilibrium. On a relaxation timescale, we see them evolve towards a new quasi-equilibrium state. After $\sim 5t_{rh}(0)$, most clusters have settled into this equilibrium, with those harboring an IMBH showing a smaller amount of mass segregation, i.e. smaller values of $\Delta\langle m\rangle$. The points from the control snapshots 128kk.1, 128kkbh.1a and 128kkbh.1b, as well as the two 16k control runs (16ks.1 and 16ksbh.1) are also plotted in Fig. 3.2, and are in good agreement with those from our models. The data in Fig. 3.2 come from a variety of initial configurations, not only in terms of the particle number but also in terms of initial mass function. The use of a differential indicator for mass segregation allows us to cancel out the
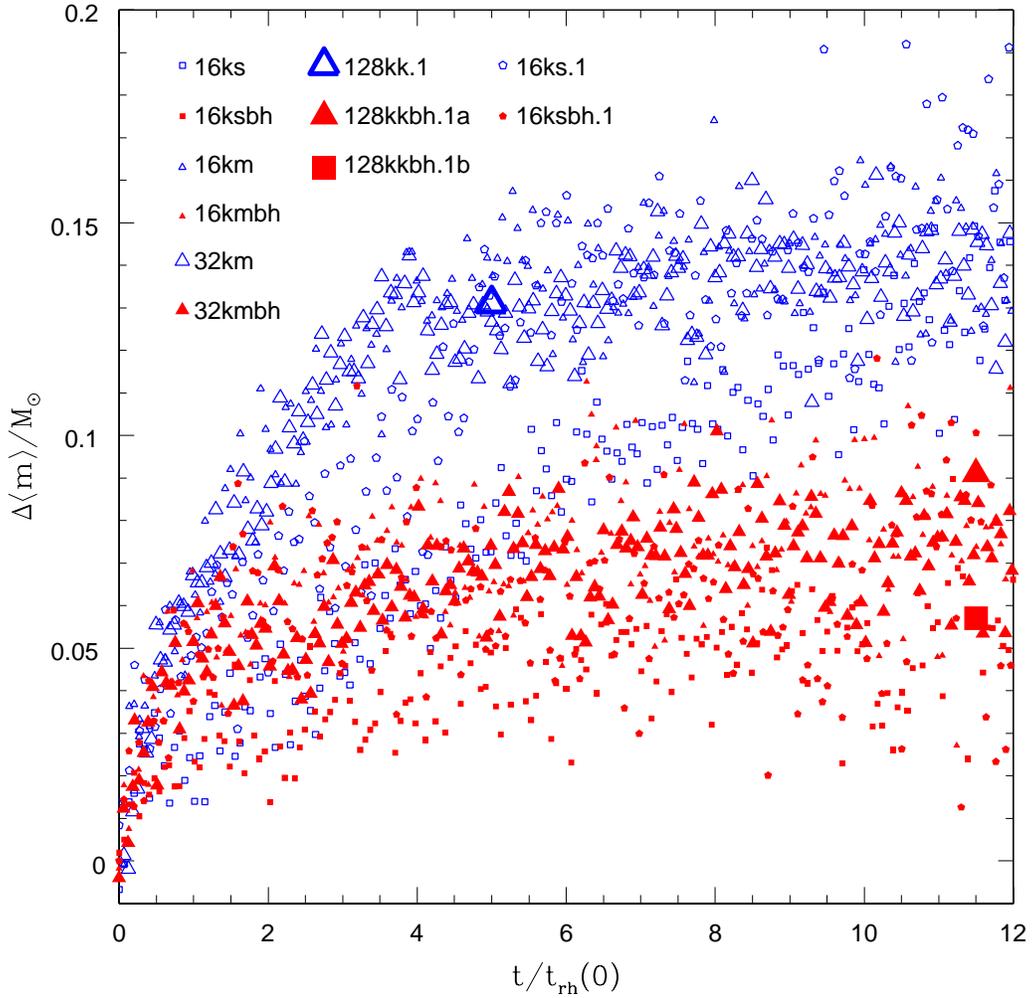
Figure 3.2: Evolution of mass segregation (via $\Delta\langle m\rangle$, expressed in $M_\odot$) across the span of all N-body simulations with $N \geq 16384$ and $f_b = 0$. Red points are from simulations with an IMBH, while blue points represent runs with no massive central object. The runs have no primordial mass segregation ($\Delta\langle m\rangle = 0$), but on a relaxation timescale, the systems settle to a quasi-equilibrium configuration with varying degrees of mass segregation. A central IMBH quenches the mass segregation and keeps $\Delta\langle m\rangle \lesssim 0.09 M_\odot$. See Tab. 3.1 for details on all of the simulations shown.

dependence on the global value of $\langle m \rangle$ (or on the global mass function slope).

Simulations with a Salpeter IMF (16ks, 16ksbh) contain many more massive remnants than the number allowed by a Miller & Scalo IMF (16km, 16kmbh, 32km, 32kmbh). For example, a 16k simulation with a Salpeter IMF and $m \in [0.2 : 100]M_\odot$ initially contains $\sim 20$ stellar mass black holes, whereas a Miller & Scalo IMF will only have $\sim 1$. This difference causes us to observe a slower growth of $\Delta\langle m \rangle$ in the Salpeter IMF runs, as a central cluster of stellar mass black holes partially quenches mass segregation of visible stars, much like an IMBH. However, stellar mass black holes eject each other from the system within a few relaxation times (see also Merritt et al. 2004), so eventually these systems fully develop the amount of mass segregation observed in runs starting from a Miller & Scalo IMF.

The control runs also reflect this trend. The 128k run without an IMBH (128kk.1) has a maximum allowed IMF mass of $15M_\odot$, meaning there are essentially no massive remnants. After 5 relaxation times, it is in good agreement with our simulations drawn from a Miller & Scalo IMF, which also produces very few massive remnants. The runs with an IMBH (128kkbh.1a and 128kkbh.1b), which have maximum initial masses of $30M_\odot$, and $100M_\odot$, respectively, are both consistent with our other runs with an IMBH. However, 128kkbh.1a's lower maximum mass results in fewer massive remnants, and thus a value for $\Delta\langle m \rangle$ closer to 16kmbh, which also contains few stellar mass black holes. 128kkbh.1b has more massive remnants and behaves similarly to 16ksbh, as we would expect. Finally, we see that our 16k control runs with a lower IMF cut-off at $0.1M_\odot$ fall somewhere between the Miller & Scalo runs and the Salpeter runs as far as mass segregation is concerned. Although we draw from a Salpeter IMF in the control runs, the lower minimum IMF mass in these simulations results in fewer massive remnants than the other Salpeter runs ($\sim 8$ stellar mass black holes instead of $\sim 20$), but more than a Miller & Scalo IMF would produce.

We also note the increased scatter in these two runs as a result of excluding the large number of main sequence stars with masses $0.1 M_\odot < m < 0.2 M_\odot$ in the calculation of the observationally accessible quantities.

The situation is very similar when primordial binaries are included (see Fig. 3.3): runs with and without an IMBH again become well separated after $\sim 5 t_{rh}(0)$. As expected, primordial binaries carry lighter particles toward the center of the cluster (e.g., a $0.6 + 0.2 M_\odot$ binary will sink to the center like a $0.8 M_\odot$ single star, but will be observed as a single unresolved source with the approximate luminosity of a $0.6 M_\odot$ star). Hence, mass segregation is partially suppressed when compared to the runs where $f_b = 0$. This difference in $\Delta \langle m \rangle$ is more significant in the runs with a Miller & Scalo IMF as compared to runs with a Salpeter IMF. Because the runs drawn from a Miller & Scalo IMF lack massive remnants, binary stars become more gravitationally dominant, and therefore have a more significant impact on the dynamics. Fortunately, the binary-driven quenching of mass segregation is weak when compared to IMBH-driven quenching and thus it is possible to discriminate between systems with and without an IMBH on the basis of $\Delta \langle m \rangle$, without the need of assuming a binary fraction.

Combining the data from all our simulations with and without binaries, we can identify three regions for the value of $\Delta \langle m \rangle$ in a collisionally relaxed GC, irrespective of its binary fraction:

- $\Delta \langle m \rangle \gtrsim 0.1 M_\odot$. The system is unlikely to contain a central IMBH.

- $\Delta \langle m \rangle \lesssim 0.07 M_\odot$. The system is a good candidate to harbor an IMBH.

- $0.07 M_\odot \lesssim \Delta \langle m \rangle \lesssim 0.1 M_\odot$. The system may or may not contain an IMBH, depending on its binary fraction and on the global IMF (and in particular on the number of massive dark remnants).
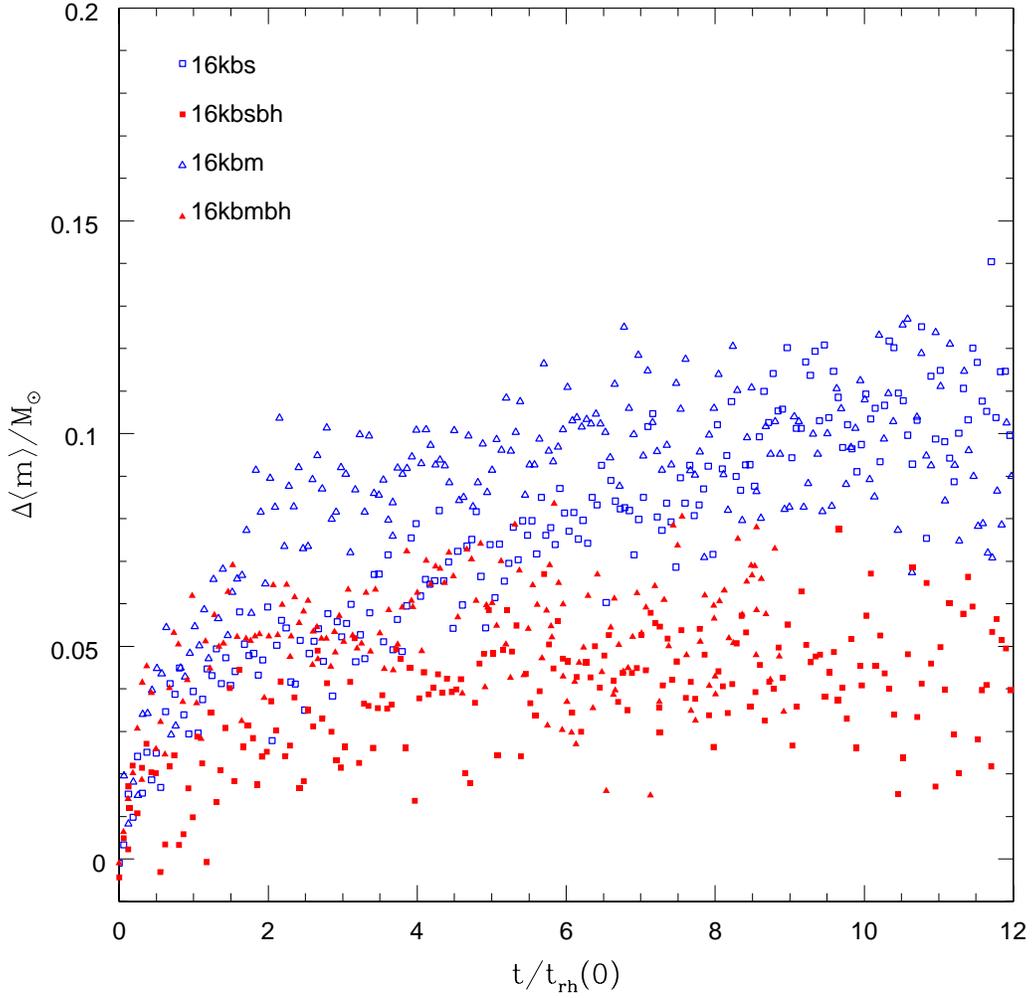
Figure 3.3: Evolution of mass segregation as in Fig. 1, but for our $N \geq 16384$ simulations *with* primordial binaries. Qualitatively, we see that the results are similar to those of the runs with single stars, but the equilibrium values of $\Delta\langle m\rangle$ are marginally lower at later times when compared to those where $f_b = 0$.

In addition, an estimate of the binary fraction based on the presence of a parallel main sequence in the color-magnitude diagram is possible for many observed clusters (Milone et al. 2008). Application of the mass segregation diagnostic therefore can account for the actual number of binaries, resulting in a further reduction in the size of the region of uncertainty.

Including the set of runs with $N = 8192$, not shown in the plots but whose

$\Delta\langle m \rangle$ is reported in Tab. 3.1, we see no trends in $\Delta\langle m \rangle$ caused by an increase in the number of objects in a cluster up to $N = 32768$. In addition, the $N = 131072$ control snapshots are consistent with our results, strengthening the independence in the evolution of $\Delta\langle m \rangle$. An increase in the number of particles reduces the deviation from snapshot to snapshot. This actually improves the application of this indicator to actual GCs, where the number of stars is significantly larger than in our runs. Similarly, we see no significant trends in $\Delta\langle m \rangle$ caused by increasing the IMBH mass up to $M_{IMBH} = 0.03$, that is 3% of the entire cluster (see Tab. 3.1). This suggests that reducing $M_{IMBH}$ below 0.01 would still result in a quenching of mass segregation.

### 3.3.3   The origin of IMBH-induced quenching of mass segregation

The onset of mass segregation along with the initial contraction of the cluster brings the most massive stars and remnants into a dense environment. Even in clusters with only single stars, the dynamical formation of binaries is inevitable. Because $M_{IMBH}$ is much larger than the typical stellar mass, the IMBH has an extremely high probability of exchanging into a binary in a close 3-body encounter. It therefore spends much of its lifetime in a binary or stable higher-N system (in more than 90% of our snapshots, the IMBH is a member of a multiple system). As a result, when massive main sequence stars in our simulations sink to the core after energy exchanges with other stars, they are efficiently "heated up" and scattered away from the core in encounters with the IMBH and any companions it has. The IMBH stochastically moves around the core as a result of these encounters and this further enhances the interaction rate because the scatter cone is continuously replenished. This mechanism for quenching mass segregation naturally explains the lack of de-

pendence of $\Delta\langle m\rangle$ on the number of particles used and the minimal dependence on $M_{IMBH}$, as well as suggesting an additional explanation as to why the presence of primordial binaries further reduces mass segregation.

## 3.4 Discussion and Conclusions

We have carried out a large set of direct N-body simulations of star clusters with and without an IMBH including a realistic mass spectrum and primordial binaries. While previous research has focused its attention mainly on the effects of an IMBH on the surface brightness and velocity dispersion profiles of the clusters — signatures that are difficult to observe — we searched instead for a different fingerprint of the presence of an IMBH. The existence of a massive, central object quenches mass segregation and this effect manifests itself in collisionally relaxed clusters through decreased radial variation in the average mass of main sequence stars. This effect does not depend on the mass of the black hole (as long as it is dominant over the typical mass of a star), nor does it depend on the details of the initial configuration of the system such as initial mass function, density profile and tidal field strength. The amount of mass segregation is only weakly dependent on the binary fraction of the cluster. This result allows us to use the amount of mass segregation to separate collisionally relaxed clusters with and without an IMBH without the need of additional modeling assumptions.

A critical requirement for the proposed signature is that the system be well-relaxed, so that it has already attained equilibrium with respect to mass segregation. From our simulations it turns out that this takes about $5t_{rh}(0)$. However we can only observe the current half-mass relaxation time and this might be shorter than its initial value if the system has lost a large fraction of its original mass. To compare

our simulations to observations, we must thus conservatively restrict ourselves to GCs that:

1. Are not too influenced by the galactic tidal field (that is, with a tidal to half-light radius $r_t/r_{hl} \gtrsim 10$, which corresponds to tidal fields weaker than the weakest field in our simulations).

2. Have half-mass (3D) relaxation times below $\approx 1.5$ Gyr, i.e. an age above $8t_{rh}$. This leaves room for a mass loss of about 50% of the initial mass while still giving an integrated age of about $5t_{rh}$. In terms of observable quantities this translates into a half-light relaxation time below $\approx 1$ Gyr.

Based on the Harris (1996) catalog, 31 galactic GCs satisfy these stringent requirements in terms of relaxation time and $r_t/r_{hl}$. The proposed diagnostic could probably be applied to more clusters after properly evaluating a dynamical model for their configuration and eventually accepting some uncertainty in the selection of likely candidates to harbor an IMBH. In addition, we note that this method can be applied to any cluster in an attempt to rule out the presence of a massive central object - a cluster with a low dynamical age but still a high ($\Delta\langle m\rangle \geq 0.1M_\odot$) degree of mass segregation actually provides a stronger null result.

Thanks to the HST treasury survey of galactic GCs, data exist for the cores of many clusters that explore deep enough to see main sequence stars down to around $0.2M_\odot$. Along the same lines, De Marchi et al. (2007), among others, have also acquired images of clusters around the half-light radius, in order to calculate the global mass function of the system. The existing data from De Marchi et al. (2007) are sufficient to apply this diagnostic to a few actual clusters. In Chapter 4, we demonstrate the feasibility of this method by applying it to previously existing HST ACS data for two clusters.

# Chapter 4

# The Application of the Mass

# Segregation Method to NGC 2298

# and NGC 6254

## 4.1 Introduction

In the previous chapter, we demonstrated the theoretical feasibility of using mass segregation in well-relaxed Galactic GCs as an indication of the presence or absence of an IMBH. Fortunately, data sufficient for this exercise exist for a number of clusters due to previous HST observations. In this Chapter, we present the application of the previous Chapter's mass segregation method to NGC 2298 (Sec. 4.2), and NGC 6254, also known as M10 (Sec. 4.3).

For each cluster, we make a thorough description of the observations and observational data analysis, as well as the further steps we took on the simulation end to make our comparison as thorough and realistic as possible. Sec. 4.2 appeared as its own paper in *The Astrophysical Journal* as *Mass Segregation in NGC 2298:*

*Limits on the Presence of an Intermediate Mass Black Hole* (Pasquato et al. 2009), and Sec. 4.3 in the same publication as *The Dynamical State of the Globular Cluster M10*(Beccari et al. 2010). My contributions to these projects were mostly on the simulation end - performing the majority of the simulations and writing most of the code used to initialize them and analyze their results. While I assisted in the preparation of both texts for publication, I was not a primary author on either paper. As such, I have summarized both papers for inclusion in this thesis.

## 4.2   NGC 2298

### 4.2.1   Observations and Cluster Properties

For our analysis of NGC 2298, we were fortunate to use already existing high-quality deep HST observations taken with the Advanced Camera for Survey (ACS) in the F606W and F814W bands (de Marchi & Pulone 2007). The ACS field covers an area on the sky of $3.4 \times 3.4$ arcmin$^2$ about the center of the cluster, and has $10\sigma$ detection limits of $m_{F606W} \approx 26.5$ and $m_{F814W} \approx 25$ with a completeness over 50% at the detection threshold. de Marchi & Pulone (2007) find that the contamination from background sources for NGC 2298 is negligible, simplifying the identification of cluster stars.

Fig. 4.1 shows the negative image of NGC 2298 viewed in the F606W band. Due to the small size of the cluster, the observations naturally extend to more than twice the cluster's half-light radius, $r_{hl}$, which is found to be around $45 - 47$ arcsec (Harris 1996; McLaughlin & van der Marel 2005). de Marchi & Pulone (2007) describe the data reduction methodology used and derive a color-magnitude diagram for NGC 2298 used throughout this analysis, which assumes a distance modulus of 15.15 mag (thus a distance of 12.6 kpc) and a color excess $E(B-V) = 0.14$ as in Harris (1996).
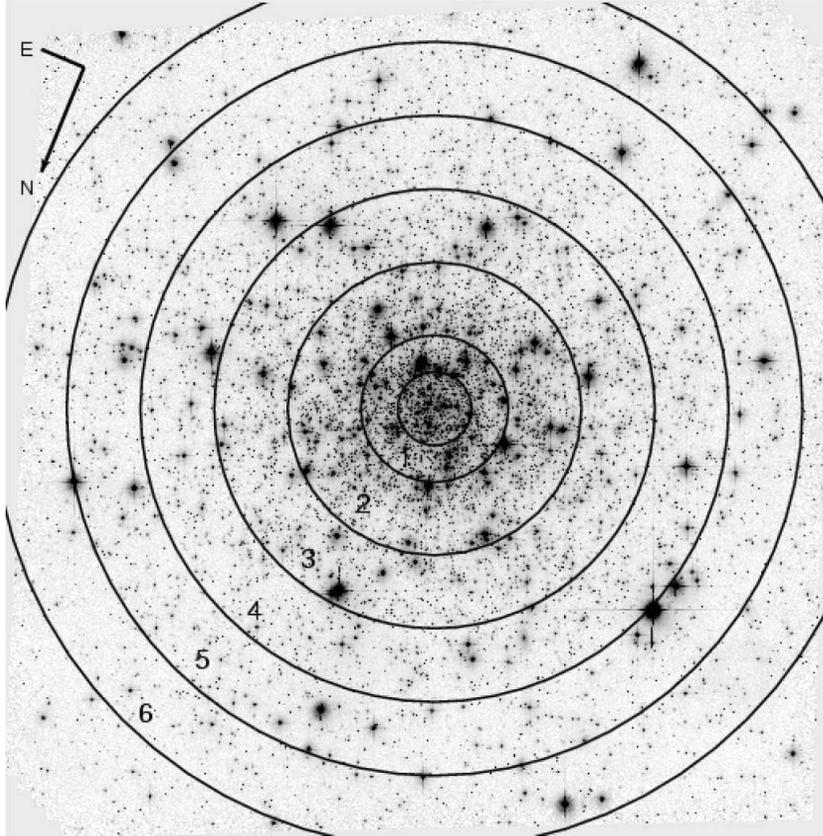
Figure 4.1: **(Figure Credit: de Marchi & Pulone (2007))** Negative image of NGC 2298 in the F606W band. The field of the camera is 3'.4 on a side, and we also show the 6 concentric annuli into which the data were divided for photometric analysis.

Individual masses are then inferred from the luminosity of each point source, given an assumed metallicity $[Fe/H] = -1.85$ (Harris 1996) using the fitting functions of Baraffe et al. (1997). The fitting covers a range of 0.2 - 0.8$M_{\odot}$, where the upper limit is set by the turnoff mass of the cluster, and the lower limit by the completeness threshold of the observations.

NGC 2298 is one of the smallest Galactic GCs; McLaughlin & van der Marel

(2005) find a mass of $3.09 \times 10^4 M_\odot$ through fitting a single-mass King (1966) model to the surface brightness profile, while de Marchi & Pulone (2007) use a multimass dynamical model to derive a mass of $5 \times 10^4 M_\odot$ and a half-mass radius $r_{hm} = 72$ arcsec. Using these various measurements we can use Eq. 3.2 (Djorgovski 1993) to derive the value of the half-light relaxation time of the cluster. The McLaughlin & van der Marel (2005) parameters lead to a current value of $t_{rh} = 10^{8.41} yr$, while those derived by de Marchi & Pulone (2007) yield $t_{rh} = 10^{8.76} yr$, both assuming an average stellar mass of $0.5 M_\odot$. Despite the evidence for significant mass loss, the cluster is still dynamically old enough to serve as a candidate for the mass segregation method, even if it was originally twice as large and four times as massive (Baumgardt et al. 2008).

Furthering the evidence for the dynamical age of NGC 2298 is the depletion of low-mass stars. This phenomenon is expected in well-relaxed systems; mass segregation drives lighter objects away from the center of the cluster where they are either ejected entirely or tidally stripped by the Galaxy's gravitational field. The degree of depletion is indicative of a system that is likely to have undergone core collapse provided it lacks an energy source, such as a population of primordial binaries or an IMBH, to prevent the collapse (Trenti et al. 2007a,b).

## 4.2.2 Comparing the Observational Data With Simulations

**The Observational End**

Our comparison begins with a calculation of the projected half-mass radius of the cluster, $r_{hm}$, from the main sequence stars in the ACS field of view. We bin the objects by clustercentric radius and sum, applying the appropriate completeness correction for the given stellar magnitude and distance from the center. Given this

surface mass density profile, we then apply a nonparametric spline smoothing technique as described in Pasquato & Bertin (2008) to get the total mass of the system in main-sequence stars. Rather than attempt to extrapolate the mass distribution beyond the ACS field of view, we account for the finite size of the image in our simulations (see **The Simulation End**). From this technique, we calculate a value of $r_{hm} = 49$ arcsec, somewhat greater than the values for the half-light radius in the literature (Harris 1996; McLaughlin & van der Marel 2005). We expect this effect due to the domination of the light profile by red giant stars, whose large mass causes them to segregate to the center of the system (see, e.g., Hurley (2007)).

We then construct the mass segregation profile of NGC 2298 by constructing $\langle m \rangle_{MS}$ as a function of clustercentric radius as in Chapter 3. Given the existence of continuous data from the center of the cluster through more than twice the half-light radius, we construct a continuous $\langle m \rangle_{MS}(r)$ at given (projected) radial distance from the cluster center by

$$\langle m \rangle_{MS}(r) = \frac{\sum_i M_i / f(m_i, r_i)}{\sum_i 1 / f(m_i, r_i)}, \tag{4.1}$$

where $M_i$ is the star's inferred mass, and $f(m_i, r_i)$ is the completeness correction for a star of magnitude $m_i$ at a projected clustercentric radius $r_i$. We defined this continuous completeness correction function by bilinear interpolation from the discrete values for $f$ given in de Marchi & Pulone (2007). The value for $\langle m \rangle_{MS}$ at a given radius is obtained by summing over a projected annulus around that radial value. In accordance with the analysis of Chapter 3, we chose to sum over 20 such annuli, each containing 5% of the stars by number. This choice nicely balances minimizing the random fluctuations in a given bin while still allowing reasonable resolution of the radial changes in the value of $\langle m \rangle_{MS}$.

We use the bootstrap method (Efron 1979) to calculate the errors in each radial annulus. For each bin of $N$ objects, we create 100 new synthetic samples by uni-

formly sampling the existing mass values $N$ times, with replacement. We then apply Eq. 4.1 to each of the 100 samples to obtain $\langle m \rangle_{MS}$ for each sample, and define the $1\sigma$ error bars for each radial annulus as the standard deviation of these 100 values. The radial variation in $\langle m \rangle_{MS}(r)$ is normalized to the value of the average stellar mass around $r_{hm}$, and is shown in Fig. 4.2 as the red points along with the $1\sigma$ error bars.

## The Simulation End

We compare our observational data to simulation data from a subset of the simulations detailed in Chapter 3, the details of which are shown in Tab. 4.1. We restrict our attention to those simulations with 16k or 32k objects, and to those simulation snapshots between 7 and 9 $t_{rh}$, giving us a total of 324 simulations snapshots with which to compare the observational data. At this point, the clusters have certainly achieved equilibrium with respect to mass segregation, but have not yet lost more than half of their objects to tidal stripping. As described in Chapter 3, we remove all compact objects and main sequence stars below $0.2 M_{\odot}$, and use only data projected onto a 2-dimensional plane. In order to reduce noise and to increase the number of objects, we sum three independent projections of each simulation.

Once we have our catalog of objects, we identify the center of the cluster's visible mass, and make a preliminary estimation of $r_{hm}$. Then, to reflect the limited field of view of the ACS camera, we restrict our analysis to only stars within 2 $r_{hm}$ of the cluster center, then recalculate the center of visible mass and $r_{hm}$ taking into account only those stars that would actually fall within the observational data. Given this information, we bin into 20 concentric radial bins, and calculate the average stellar mass of the objects in that radial bin. Fig. 4.2 shows the 1 and 2-$\sigma$ contours of the radial variation in mass segregation of the 324 simulation snapshots, also normalized
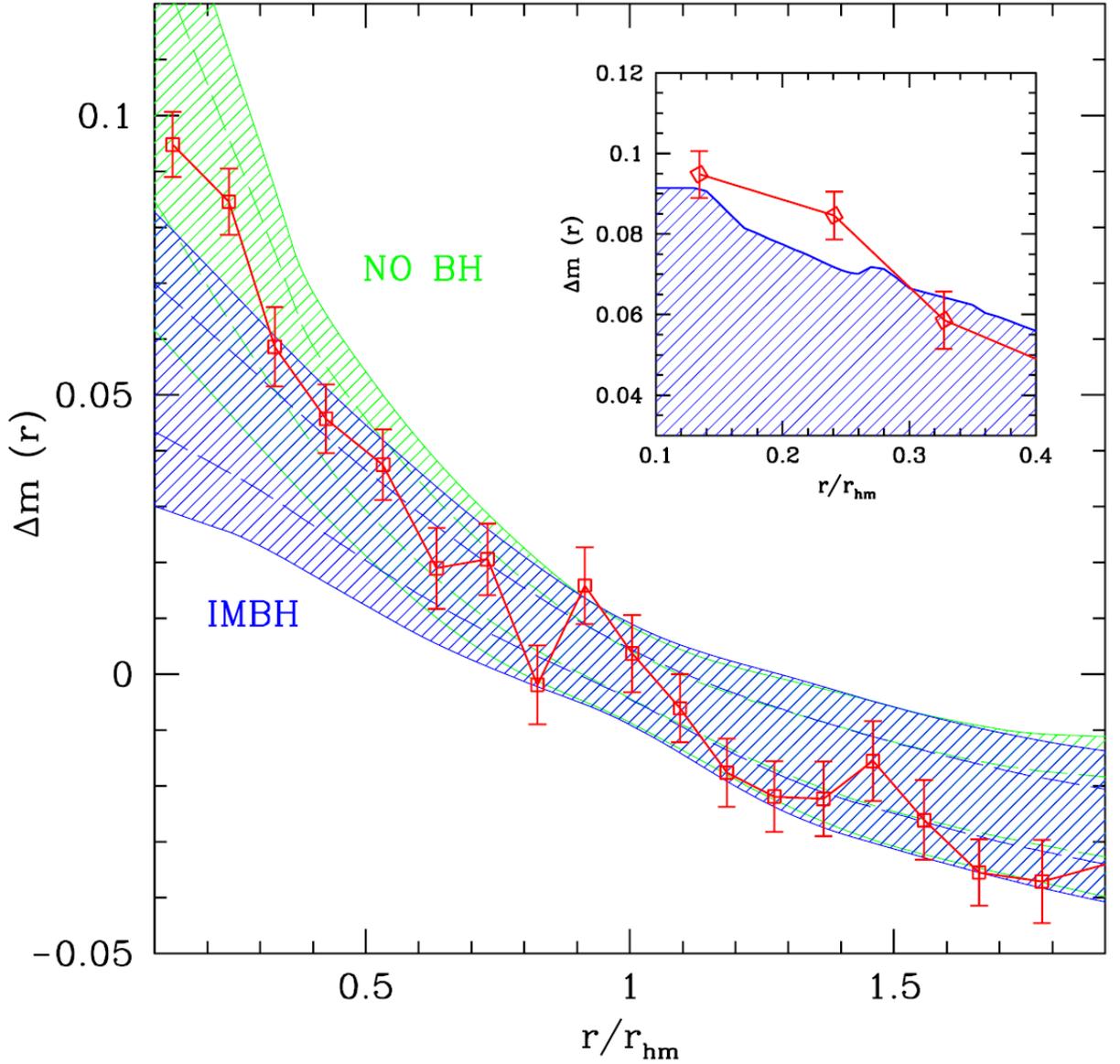
Figure 4.2: Comparison of mass segregation between numerical simulations with (blue hatched region with 1 and 2-$\sigma$ error bars) and without (green hatched region with 1 and 2-$\sigma$ error bars) an IMBH with our observations of NGC 2298 (red points with 1-$\sigma$ error bars). The inset shows the upper envelope of the innermost points of all our simulations with an IMBH, suggesting that the degree of mass segregation is normal for a cluster without a central MBH.

Table 4.1: Summary of the N-body simulations used in the NGC 2298 analysis

| ID | IMF | $M_{BH}/M_{tot}$ | $M_{BH}/M_\odot$ | $f_b$ | $\langle\Delta m\rangle_{Ch.3}$ | $\langle\Delta m\rangle_{Ch.4}$ | $\sigma_{Ch.4}$ | $\Delta m_{Ch.4}^{min}$ | $\Delta m_{Ch.4}^{max}$ |
|---|---|---|---|---|---|---|---|---|---|
| 16ks | Sal | N/A | N/A | 0 | 0.11 | 0.101 | 0.008 | 0.083 | 0.113 |
| 16ks.1 | Sal | N/A | N/A | 0 | 0.14 | 0.130 | 0.010 | 0.112 | 0.158 |
| 16km | M&S | N/A | N/A | 0 | 0.14 | 0.137 | 0.009 | 0.112 | 0.151 |
| 16kbs | Sal | N/A | N/A | 0.1 | 0.09 | 0.074 | 0.008 | 0.056 | 0.090 |
| 16kbm | M&S | N/A | N/A | 0.1 | 0.10 | 0.102 | 0.009 | 0.085 | 0.124 |
| 32km | M&S | N/A | N/A | 0 | 0.14 | 0.142 | 0.007 | 0.128 | 0.154 |
| 16ksbh | Sal | 0.015 | 103.1 | 0 | 0.05 | 0.048 | 0.006 | 0.037 | 0.060 |
| 16ksbh.1 | Sal | 0.015 | 60.9 | 0 | 0.06 | 0.060 | 0.010 | 0.041 | 0.078 |
| 16kmbh | M&S | 0.015 | 128.2 | 0 | 0.08 | 0.071 | 0.009 | 0.048 | 0.091 |
| 16kbsbh | Sal | 0.01 | 113.4 | 0.1 | 0.04 | 0.042 | 0.005 | 0.033 | 0.052 |
| 16kbmbh | M&S | 0.01 | 141.0 | 0.1 | 0.05 | 0.050 | 0.008 | 0.038 | 0.072 |
| 32kmbh | M&S | 0.01 | 240.0 | 0 | 0.07 | 0.069 | 0.005 | 0.058 | 0.083 |
| 16kmbh$^I$ | M&S | 0.015 | 128.2 | 0 | N/A | 0.069 | 0.008 | 0.055 | 0.083 |
| 16kmbh$^{II}$ | M&S | 0.015 | 128.2 | 0 | N/A | 0.063 | 0.010 | 0.040 | 0.079 |
| 16kmbh$^{III}$ | M&S | 0.015 | 128.2 | 0 | N/A | 0.055 | 0.009 | 0.042 | 0.074 |
| 16kmbh$^{IV}$ | M&S | 0.015 | 128.2 | 0 | N/A | 0.074 | 0.009 | 0.060 | 0.093 |

Note. — Contains information about the numerical simulations used in our comparison with NGC 2298 observational data. The first two groups of these are a subset of the simulations used in Chapter 3 (see Tab. 3.1), and their first 6 columns are recorded directly from there. The eighth column, $\langle\Delta m\rangle_{Ch.3}$ reports the time-averaged value of our mass segregation measure from Chapter 3 from all of the snapshots between $5t_{rh}$ and $12t_{rh}$ in each simulation. $\langle\Delta m\rangle_{Ch.4}$ denotes this quantity as per the normalization and analysis of Sec. 4.2.2, along with its standard deviation, minimum and maximum values for each simulation. In addition, we have added four runs drawn from the same initial conditions as run 16kmbh, detailed in the 3rd group.

to the value of the average stellar mass at $r_{hm}$.

## Putting the Two Together

In Fig. 4.2, we see that the observed data points corresponding to the mass segregation profile of NGC 2298 fall entirely within the region encompassed by our simulations without a central MBH, and fall outside the 2-$\sigma$ contours of our simulations with an IMBH for the innermost few data points. The inset of Fig. 4.2 shows that the observations of the innermost data points are inconsistent with the

upper envelope of all of our simulations with a central MBH. For this to be the result of a random fluctuation in a system with an IMBH would require two 2-$\sigma$ events simultaneously - one in the simulations and another in the data. Thus, we can conclude that such a scenario is unlikely at around the 3-$\sigma$ confidence level.

As a second test of our method we performed a slightly different analysis. Instead of treating the variations in initial conditions of our simulations as a source of random error, we instead derive the 2-$\sigma$ contours of each simulation separately and plot the envelope of these individual confidence regions in Fig. 4.3. Despite the fact that we will naturally get larger contours from this method of analysis, we can see that there is still a distinct difference between the simulations with and without an IMBH.

In addition to changing our methodology, we also added four more simulations to the analysis with identical initial conditions (but different random number seed) to run 16kmbh, the simulation from Chapter 3 with the highest degree of mass segregation with an IMBH (see Tab. 3.1). This simulation notably had a higher degree of mass segregation than the 8k and 32k runs with otherwise identical initial conditions, suggesting that this may have been the result of a random fluctuation. In fact, we see in Tab. 4.1 that none of the four identical simulations contained such a high degree of mass segregation, although they all produced qualitatively similar results.

Adding these simulations to our analysis provides us with a better feel for the run to run variation in the upper envelope of the degree of mass segregation in our simulations with an IMBH. Combined with the change in the error analysis methodology, this provides us with an even more strict test of the presence of a MBH in a cluster. Yet, as we can see in the inset to Fig. 4.3, the data from NGC 2298 are still inconsistent with the upper envelope of any of these simulations at the $\sim$3-$\sigma$ level (see the second data point from the center in Fig. 4.3).
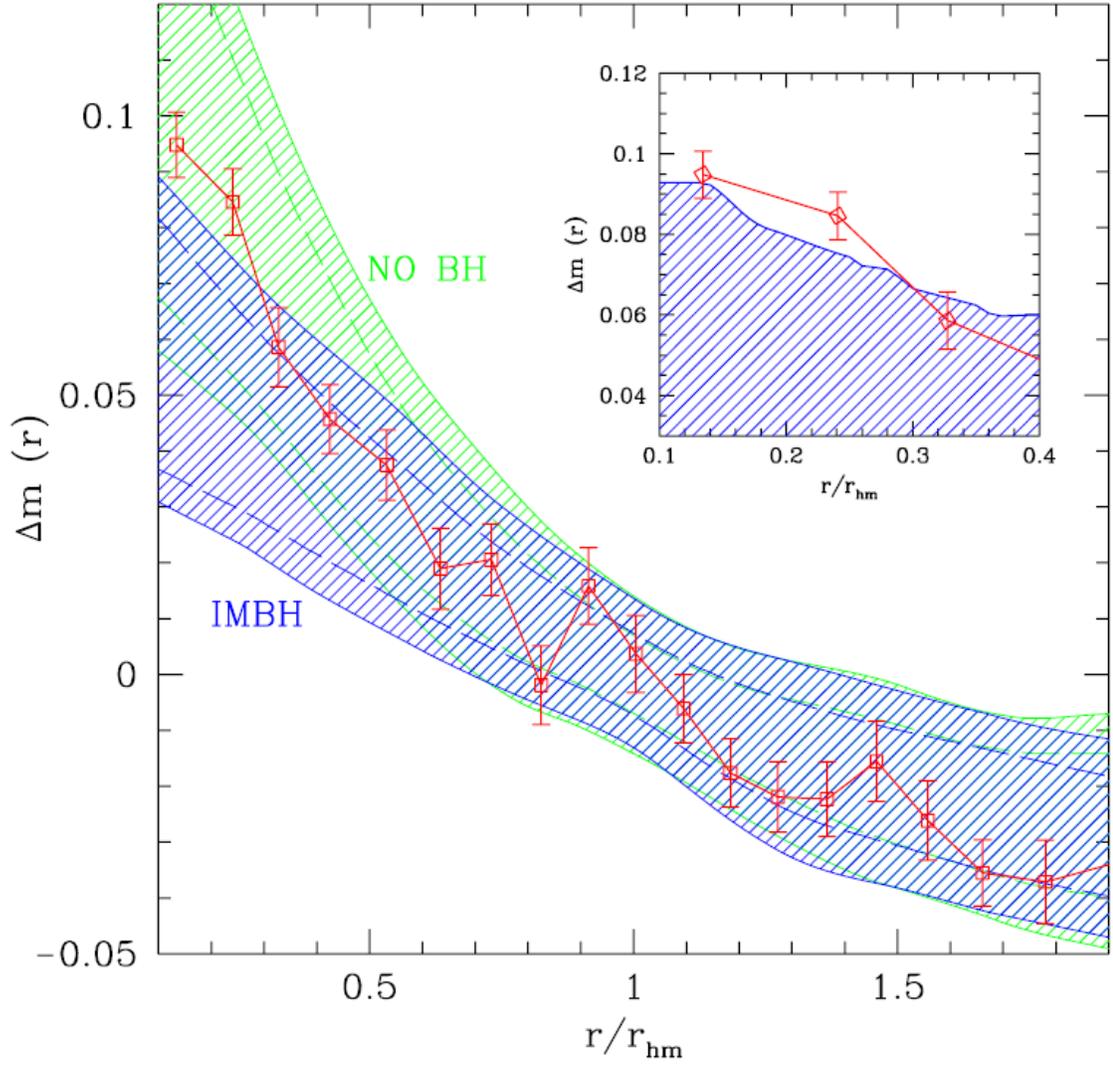
Figure 4.3: Identical plot to Fig. 4.2 except for two key differences. Firstly, in the analysis we treat the differences in initial conditions as systemic rather than random and take the global envelope of the 2-$\sigma$ contours of each individual run rather than taking the 2- envelope of all of the snapshots together. Secondly, this plot contains four extra N-body simulations drawn from identical initial conditions as simulations 16kmbh (see Tab. 4.1).

As a final test, we note that the shape of the mass function in NGC 2298 closely resembles that of our 32k simulation without an IMBH when it has lost around 75% of its mass, as is thought to have happened in NGC 2298 (Baumgardt et al. 2008). Both systems are depleted in low-mass stars, likely as a result of the combination of mass segregation and tidal stripping. The left panel of Fig. 4.4 shows a comparison of the mass functions of our 32km and 32kmbh simulations after 16 initial half-mass relaxation times have elapsed. We can see that the system with the IMBH is far less depleted in low-mass stars due to the quenching of mass segregation, resulting in a flat rather than an inverted mass function. This agreement between the simulations and data also provides us with an after-the-fact confirmation that NGC 2298 has likely reached equilibrium with respect to mass segregation, and therefore is a dynamically old system.

We repeat our previous analysis of Figs. 4.2 and 4.3 in the right-hand panel of Fig. 4.4 using only snapshots from our 32k Miller & Scalo (1979) simulations, restricted to times such that $t \in [15.5 : 16.5]t_{rh}$. We take care to project our snapshots along random lines of sight and "observe" the simulations by rejecting with probability $1 - f(m, r)$ the individual stars in the simulation with inferred magnitude $m$ and distance from the cluster center $r$. The much smaller contours of the simulations lead to our strongest rejection of the IMBH hypothesis, at about the 5-$\sigma$ level.

Our simulations had central MBHs of mass $\sim 1\%$ of the cluster mass, thus given our analysis we can likely exclude the presence of a black hole of mass greater than or equal to $3 - 5 \times 10^2 M_\odot$, depending on whether we use the De Marchi et al. (2007) or McLaughlin & van der Marel (2005) value for the total mass of NGC 2298.
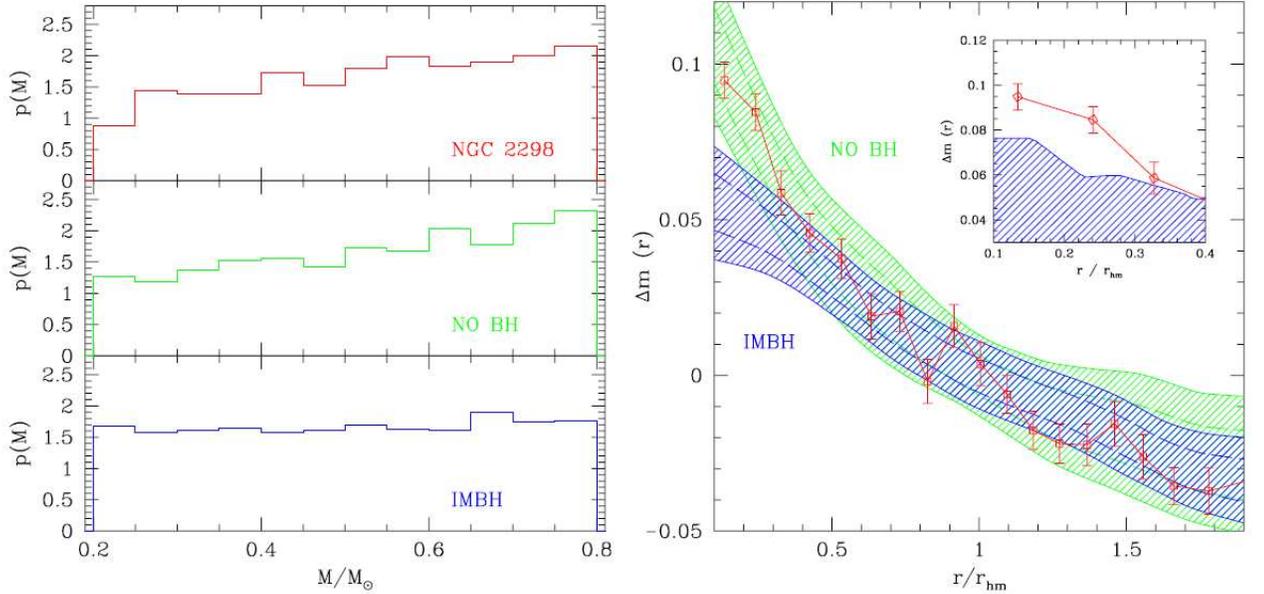
Figure 4.4: The left hand panel compares the mass functions of NGC 2298 to our 32k simulations with and without an IMBH (32km and 32kmbh in Tab. 4.1) at a time of $16t_{rh}$ after both systems have lost around 75% of their initial mass. The simulation without an IMBH has been depleted of lower-mass stars due to tidal stripping of the halo stars which are preferentially low-mass due to mass segregation. The presence of an IMBH impedes this process and thus a more even mix of stars are stripped, leading to a flatter mass function. In the right panel, we compare the observed mass segregation profile of NGC 2298 to the snapshots taken between 15.5 and $16.5t_{rh}$ in the two 32k simulations. The observed data are inconsistent with our simulations with an IMBH.

### 4.2.3 Sources of Systematic Uncertainty in Our Results

Most the possible systematic uncertainty in our analysis comes from the observations, as in our numerical simulations we have the ability to exactly observe the system without error. In order to make a realistic comparison between these two data sets, we had to choose a way to fix the scaling between them. This was accomplished by normalizing both the radial position within the cluster and the change in average stellar mass to their respective values at the half-mass radius. However, this choices means that any error we make in determining $\Delta m(r_{hm})$, either by a random local fluctuation in the data, or by a misdetermination of $r_{hm}$ could shift our entire data set up or down in Figs. 4.2, 4.3, and 4.4.

The former error is mitigated by our choice to calculate $\langle m \rangle (r_{hm})$ by averaging over all main sequence stars with $r \in [0.8, 1.2] r_{hm}$, rather than trying to determine the value at exactly $r_{hm}$. This choice smoothes out small-scale Poissonian fluctuations that might occur. When we replicated our analysis while using $r \in [0.9, 1.1] r_{hm}$, we reproduced our essential results but with more noise, as one might expect.

An error in our determination of $r_{hm} = 49$ arcsec could potentially have a serious impact on our analysis. To test this, we repeated our analysis twice after shifting our value of $r_{hm}$ by $\pm 4$ arcsec. While the results were slightly different, they fell comfortably within our previous 1-$\sigma$ error bars. As the plots show that the average stellar mass increases with decreasing radius, it is not surprising that the degree of measured mass segregation decreases as we decrease $r_{hm}$ (and thus increase the measured average stellar mass at $r_{hm}$). However, to significantly alter our basic null result requires $r_{hm} \leq 40$ arcsec.

A final possible source of error in our observational measurements is our deter-

mination of the center of the cluster. As Noyola & Gebhardt (2006) note, this can, in principle, be a difficult problem. However, this is unlikely to be a significant issue for this work because of the high quality of our data, and because analyzing mass rather than light tends to be more reliable because it is less prone to the small-scale fluctuations of a few very bright giant stars.

In principle, though, a misdetermination of the center of the cluster would cause the mass segregation profile to be artificially shallower. While this would actually strengthen our result, in the interest of being thorough we performed a Monte Carlo bootstrap analysis to assess the impact of this error on our results. We created 100 synthetic samples of our data by uniformly resampling the observed main sequence stars with replacement, and then calculated the center of mass in each new data set. The standard deviation of the differences was $\leq 0.4$ arcsec, suggesting this to be a very minor effect.

### 4.2.4 Discussion and Conclusions

As we noted at the end of Chapter 3, the applicability of the mass segregation method to a particular star cluster is dependent on having undergone at least 5 initial half-mass relaxation times to ensure that it has reached a reasonable equilibrium with respect to mass segregation. We proposed that having a current half-light relaxation time $t_{rh} \leq 1$Gyr and a ratio of tidal radius to half-mass radius $r_t/r_{hm} \geq 10$ would virtually guarantee that this criterion was met for a Galactic globular. NGC 2298 easily meets the first of these requirements with either the De Marchi et al. (2007) or McLaughlin & van der Marel (2005) modeling, but strictly speaking, it fails the second criterion, with a $r_t/r_{hm} \simeq 7$ (De Marchi et al. 2007; Harris 1996). However, several factors mitigate this.

Firstly, the criteria were chosen conservatively to allow an across-the-board es-

timation of whether each cluster would likely be a candidate for this analysis - it was intended to be a sufficient criterion, but not a necessary one. In addition, the inverted mass function of NGC 2298 strongly suggests that it is a dynamically old cluster, as does the analysis provided by Baumgardt et al. (2008) that was mentioned in Sec. 4.2.1. Finally, our analysis found a high enough degree of mass segregation to strongly suggest that NGC 2298 does not harbor an IMBH; if NGC 2298 had not undergone at least 5 initial half-mass relaxation times that would actually strengthen our conclusions. Conclusive proof of the dynamical age of a cluster would, however, be necessary to argue for the presence of an IMBH, as a low degree of mass segregation due to an IMBH would be indistinguishable from that due to the cluster not having yet attained equilibrium with respect to mass segregation.

## 4.3   M10 (NGC 6254)

### 4.3.1   Observations and Cluster Properties

Our data, as in Sec. 4.2.1, comes from deep HST observations, and is shown in Fig. 4.5. The primary observations of the cluster center were taken with the ACS in the F606W and F816W bands. As resolving smaller main sequence stars near the detection threshold (around 0.25 $M_\odot$ in this sample) with a completeness greater than 50% is important for our analysis, we limited our observations to those with long exposure times ($\geq$ 90s). Our data also includes a second set of observations in the F606W and F814W bands from the Wide-Field Planetary Camera 2 (WFPC2) during Cycle 5 in 1995 located around 3' Southwest of the center of the cluster, extending out to around twice the Harris (1996) value for the half-mass radius. The full details of the observations taken are shown in Tab. 4.2.

Our identification of stars between the various images was done with various data
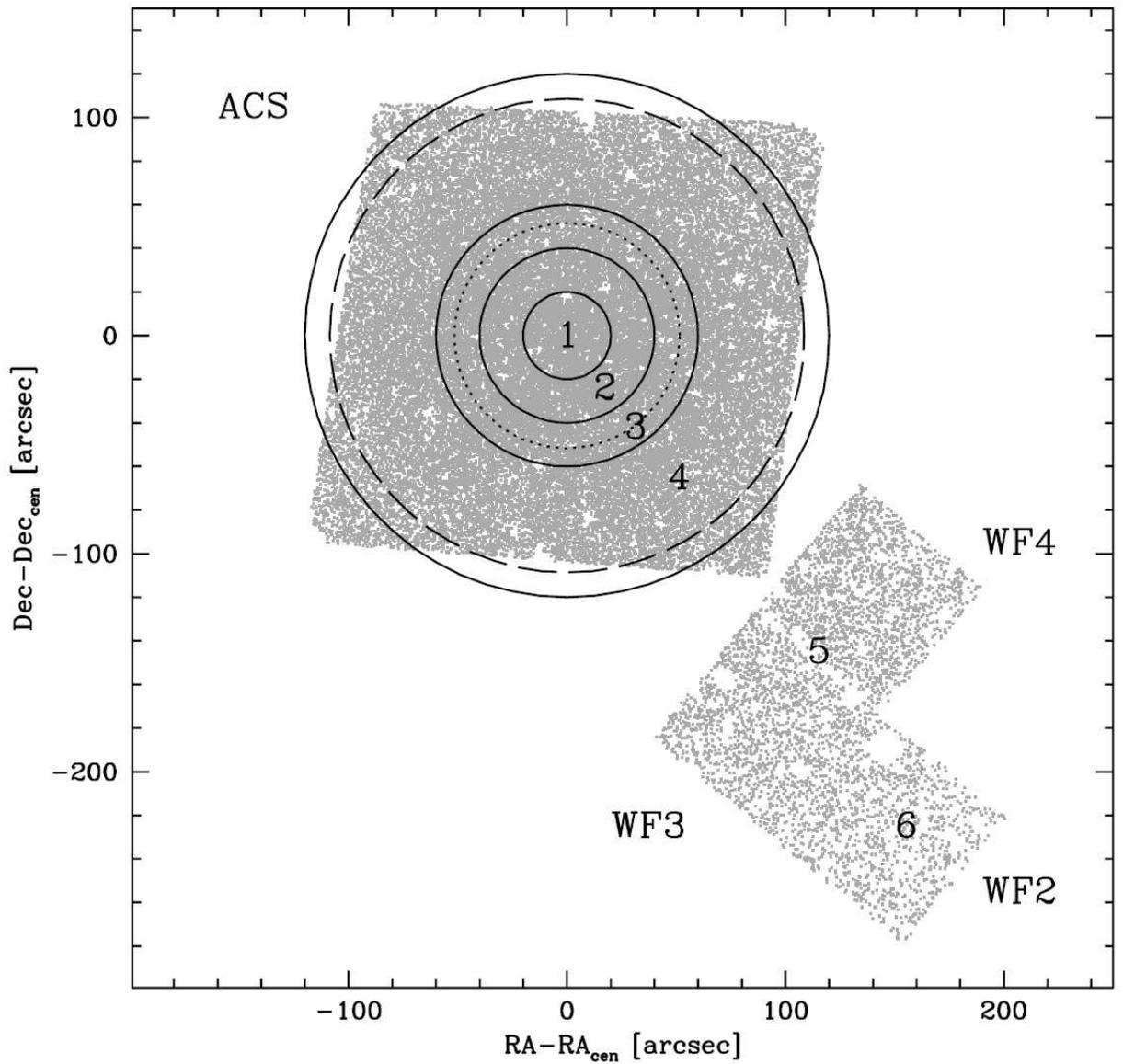
Figure 4.5: Photometry of NGC 6254 as seen through long HST exposures. Data around the cluster center are taken from 90s exposures through the ACS camera, while the data to the Southwest of cluster center were from the various (labeled) chips of WFPC2. Also shown are the Harris (1996) values for the core radius (dotted circle), and half-light radius (dashed circle) as well as the 6 regions into which we divided our data for photometric analysis.

Table 4.2: Summary of the observations of NGC 6254.

| Camera | Band | Exp. | Exp. Time |
|--------|------|------|-----------|
| ACS | F606W | 4 | 90s |
| - | F814W | 4 | 90s |
| WFPC2 | F606W | 1 | 1100s |
| - | F606W | 3 | 1200s |
| - | F814W | 1 | 1100s |
| - | F814W | 3 | 1200s |

reduction software. The Stetson (1987) DAOPHOTII/ALLSTAR routines were used to find stars, and then DAOMATCH/DAOMASTER to align the frames and match up the individual stars in the different images. After using DAOPHOT/FIND to obtain a full star list, ALLFRAME (Stetson 1994) was used to catalog the individual stellar luminosities. In order to eliminate artifacts due to saturated stars in the images, we used the Cool et al. (1996) method of eliminating object with values of the ALLFRAME sharpness parameter, $sh$, that fall outside the range $-0.15 < sh < 0.15$.

The resulting data set from the WFPC2 camera contains 4995 objects; this data has already been examined by De Marchi & Paresce (1996); Piotto & Zoccali (1999), and comparisons between the color-magnitude diagrams and luminosity functions reveal no apparent inconsistencies. The ACS data set contains substantially more objects, 56812, given both its wider field of view and image of the densest part of the cluster. In order to further clean the data and eliminate spurious objects, we followed the procedure of de Marchi & Pulone (2007) and calculated the main sequence mean ridge lines for each data set by fitting a 2nd order polynomial after removing those objects more than $2\sigma$ from the linear best fit, where $\sigma$ is the combined photometric error in the $V$ and $I$ bands derived from the application of the ALLFRAME routine. We then removed those objects that fell outside $2.5\sigma$ of the mean ridge line before

further calculation, reducing our data sets to 46407 and 4390 stars, respectively.

In Fig. 4.6, our derived MS mean ridge line is in very good agreement with the models of (Baraffe et al. 1997); this confirmation justifies our choice to use the fitting functions in that work to infer masses from luminosities as we did in Sec. 4.2. The best fit to the cluster parameters gives $[M/H] = -1.0$, $(m - M) = 14.21$ and color excess $E(B - V) = 0.26$, shown by the solid line in Fig. 4.6. These values are in good agreement with those of Piotto & Zoccali (1999) - $(m - M) = 14.20$; $E(B - V) = 0.29$ - and with $[Fe/H] = -1.41$ from Carretta & Gratton (1997), providing us with another consistency check for our data.

Unlike NGC 2298, NGC 6254 displays a large ratio of core to half-mass radius (McLaughlin & van der Marel 2005), which previous numerical simulations have found is an indication of the presence of an energy source capable of halting core collapse (Trenti et al. 2007a; Vesperini & Chernoff 1994). Its mass of $1.5 \times 10^5 M_\odot$ makes it large enough to support most IMBH formation scenarios (e.g., see Miller & Hamilton (2002), Portegies Zwart et al. (2004)), yet small enough to be dynamically well-relaxed with a current relaxation time $t_{rh} = 10^{8.86} yr$, and far enough away from the Galaxy to have avoided significant tidal stripping ($r_t/r_{hm} = 11.86$ Harris (1996)). This combination of factors ensures that NGC 6254 has undergone at least 5 initial half-mass relaxation times, making it an ideal candidate for the mass segregation method.

### 4.3.2 The Mass Segregation Profile of NGC 6254

We replicate our analysis performed in Sec. 4.2.2 for our NGC 6254 data. We calculate the (projected) half-mass radius of the main sequence stars in our catalog (with masses $0.26 - 0.8 M_\odot$) to be $r_{hm} = 124''$. As was the case in NGC 2298, this value slightly exceeds that in the literature (Harris (1996) finds a value of $108.6''$),
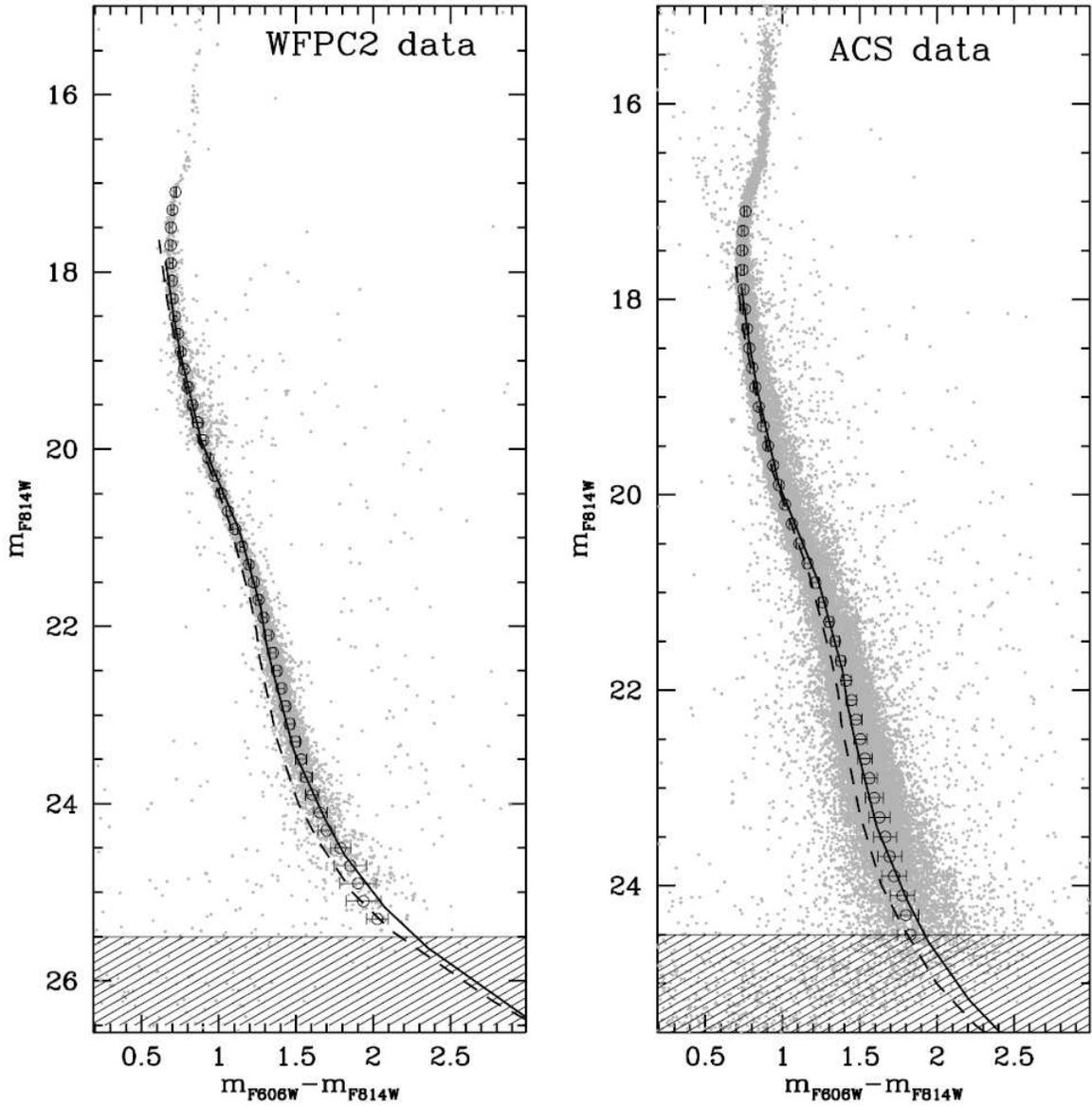
Figure 4.6: Color magnitude diagram of NGC 6254 for both the WFPC2 (left) and ACS (right) data. Also shown is our derived main sequence mean ridge line, along with $1\sigma$ error bars, as well as the fits from the Baraffe et al. (1997) models for $[M/H] = -1.3$ (dashed line) and $[M/H] = -1.0$ (solid line).

which is expected due to the disproportionate light emitted by giant stars that preferentially end up in the cluster core. We normalize our mass segregation profile to this value, as was done in Sec. 4.2.2, then compare with the identical set of simulations used there (see Tab. 4.1).

In the left panel of Fig. 4.7, we can see that the amount of mass segregation in NGC 6254 is significantly less than that found in NGC 2298 in Sec. 4.2. The inset to the left panel shows that the observational data clearly fall within the $2-\sigma$ envelope of our simulations that harbor an IMBH, meaning we certainly cannot rule out the possibility of finding an IMBH with any real confidence. However, the data are also fall comfortably within the envelope of our many simulations without an IMBH - our choice to explore all parts of the parameter space with a variety of initial conditions has made it more difficult to distinguish between models. In order to make a more conclusive statement about the dynamical state of the cluster, we were forced to consider subsets of our simulation data.

The right panel of Fig. 4.7 shows a comparison of the observational data to just those simulations with 32k objects, a Miller & Scalo (1979) IMF, and no primordial binaries - arguably the most realistic among our simulations both in number of objects and IMF. The data are inconsistent at $3-\sigma$ or better with either group of simulations, suggesting that neither model is a good representation of the cluster dynamics. However, since both envelopes are due to a single simulation each, it is possible that the small sample size affected the results to some degree.

The large envelopes in the left panel of Fig. 4.7 are partially due to the fact that simulations with and without primordial binaries are included together. Our initial simulations with binaries all had a fraction of $f_b = 10\%$, motivated somewhat by the existence of clusters with similar estimated binary fractions (e.g., see Albrow et al. (2001)), and also by the fact that higher choices of $f_b$ produce nearly identical
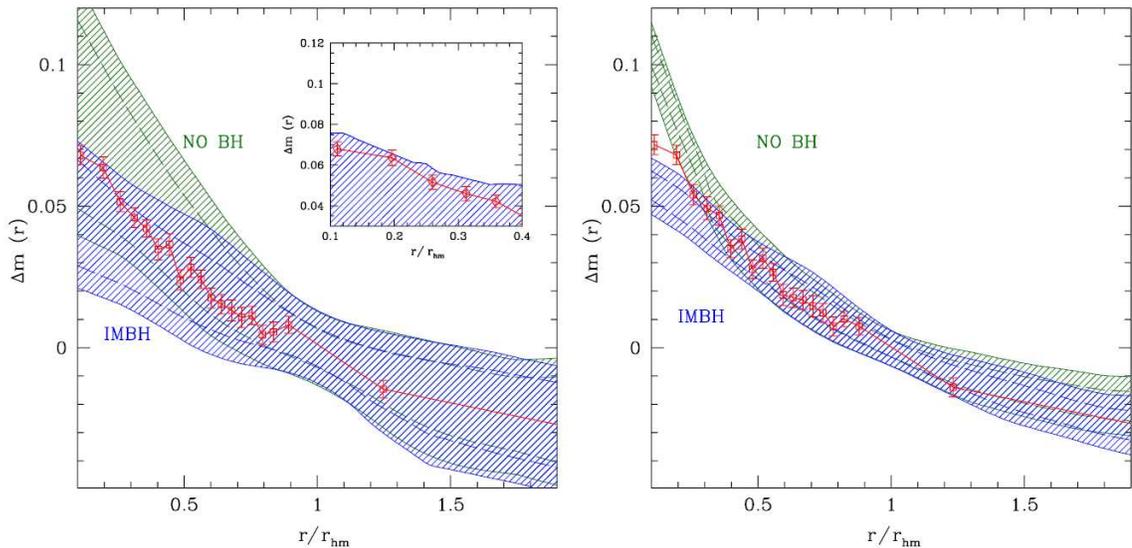
Figure 4.7: As in the plots of Sec. 4.2, compares the mass segregation profile of NGC 6254 (red dots with $1\sigma$ error bars) to the envelope of all of our numerical simulations (left panel) and to our 32k simulations with a (Miller & Scalo 1979) IMF and no primordial binaries (right panel). The inset in the left panel shows the consistency of the data with the ($2\sigma$) upper envelope of the all simulations with an IMBH present.

dynamical evolution (Heggie et al. 2006; Vesperini & Chernoff 1994). In order to better resolve the effects of our initial conditions on the mass segregation profile of our simulated clusters, we ran 3 additional simulations. The three simulations contained 32k objects, had masses drawn from a (Miller & Scalo 1979) IMF, and had binary fractions of 1%, 3%, and 5% respectively.

Fig. 4.8 compares our observational data to the envelopes of the new simulations with $f_b = 3\%$ and $f_b = 5\%$ for the left and right hand panels, respectively. In each case the IMBH envelope shown is identical to the one in the right panel of Fig. 4.7. In order to comfortably explain the low degree of mass segregation in NGC 6254,
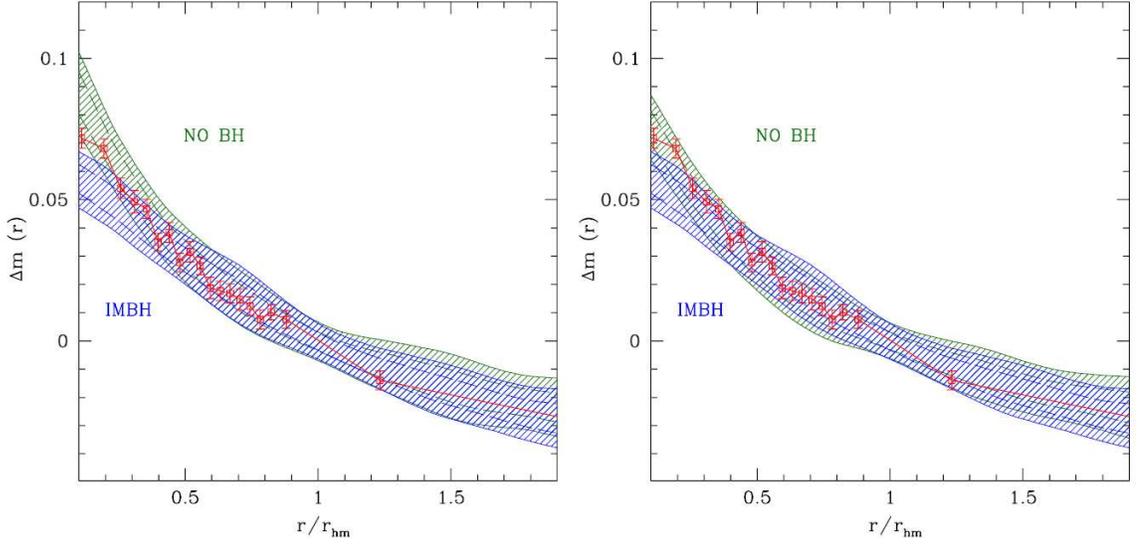
Figure 4.8: Identical to the right panel of Fig. 4.7 except the simulations with no IMBH contain initial binary fractions of 3% (left panel) and 5% (right panel).

we can see that a binary fraction of around 5% would be needed as an alternative explanation to the presence of an IMBH.

## 4.3.3 Discussion and Conclusions

As discussed in Chapter 3, as well as in the literature (e.g., Trenti et al. (2007a)), either binaries or an IMBH can act as an energy source in the core of a star cluster, although our simulations have shown that an IMBH does a more efficient job of "reheating" the cluster stars, leading to a larger core and qualitatively less mass segregation. In this case, it is clear that the data are inconsistent with our most realistic simulations without primordial binaries or an IMBH. Given that NGC 6254 is clearly dynamically old enough to have achieved equilibrium with respect to mass

segregation, the low amount observed is indicative that some force is ejecting massive stars from the core of the cluster and limiting the central average mass.

Unfortunately, given that the binary fraction of NGC 6254 is as of yet undetermined, we cannot make a comprehensive statement about the presence or lack of an IMBH. An estimation of the binary fraction could conceivably allow a more definitive statement to be made. In either event, this cluster is certainly a viable candidate for follow-up proper motion studies in the search for an undisputed IMBH detection, as some source of energy is halting core collapse and suppressing mass segregation.

# Chapter 5

# Conclusions

## 5.1 What We Have Accomplished

We set out in writing this dissertation with the goal of making a contribution to MBH research, a particularly crucial and fascinating aspect of modern astrophysics. The gravitational dominance of MBHs exerts vast influence on their host galaxy or cluster, shaping the evolution of up to billions of other bodies. Their ability to produce massive electromagnetic signals that outshine those same billions of other stars gives an indication of their importance in creating the universe we observe today. They can produce jets of particles accelerated to nearly the speed of light that burst out into the surrounding medium, perhaps affecting the fate of entire clusters of galaxies.

Despite the many ways in which MBHs appear to be critical to astrophysics as we know it today, there remain many unanswered questions. Much about the existing populations of these objects still eludes detection. What fraction of MBHs exist below $10^7 M_\odot$? $10^6 M_\odot$? Do even lesser black holes form in star clusters? Knowledge of just these few pieces of information would help answer many open questions pertaining to galaxy formation and evolution, and a host of other cosmological

questions.

As time progresses, our observational methods and capabilities will continue to improve, increasing the accuracy of current measurements. However, because of the inherent difficulties associated with making direct observations of these important astrophysical objects, we are forced to pursue alternative means of gathering information in the mean time. While the massive gravity exerted by these objects does not produce an electromagnetic signature itself, its influence can be viewed both by the gravitational radiation released during its encounters with other objects in its host system, or via signatures in the distributions of stars whose radiation can be observed. We have used numerical simulations in this work to predict these signatures, and, in the case of our simulations of globular clusters, compared these predictions to observational data.

In Chapter 2, we investigated dense stellar systems surrounding a MBH at the center of a typical galaxy. The particular details of the dynamics of these systems determine the rate at which compact objects will be perturbed onto high-eccentricity orbits. Such objects will shed energy and angular momentum through the emission of gravitational radiation during close passages by the MBH and, provided they remain undisturbed, will eventually reach a low enough period to emit at a frequency detectable by the future space-bound detector, LISA.

Complicating the computational nightmare associated with trying to coax a detection out of the complex LISA data stream are the vast uncertainties in the rate and orbital characteristics of these events. We performed a variety of direct N-body simulations with the goal of reducing these uncertainties that pushed the existing envelope of knowledge. Our inclusion of the first-order Post-Newtonian correction allowed us to correctly resolve the effects of resonant relaxation. Our simulation of up to $N = 100$ objects, while still well below the number needed

for a fully realistic model, represents a doubling of the previous maximum number included in a direct N-body simulation of this nature.

Our results provided a contrast to one of the prevailing wisdoms gleaned from previous approximate methods of simulating the dynamics of galactic centers. While the rate of EMRI objects found in our simulations ($\sim 4 \times 10^{-7}\text{yr}^{-1}$ per galaxy) is in good agreement with the literature, ($\sim 10^{-6} - 10^{-8}\text{yr}^{-1}$ per galaxy), the specific details of our merging objects differed considerably from the expected distribution. We expected to find that most EMRIs form on highly eccentric orbits with semimajor axes $\sim 2000$ AU. Our simulations showed otherwise; four of our five mergers had $a \lesssim 750AU$ when they began appreciably emitting gravitational radiation, and all five were initially formed on orbits with $a_i \lesssim 750AU$. Our findings affect the distribution of orbital eccentricities EMRI objects will have when they are detectable by LISA.

In Chapter 3, we joined the search for the first definitive detection of an IMBH in a Galactic globular cluster. While multi-year proper motion studies are likely needed to achieve this goal, the expensive nature of these observations necessitates careful selection of candidate clusters to increase the likelihood of detection. We presented a new method for suggesting the presence of an IMBH in a well-relaxed star cluster as a precursor to these studies.

Through N-body simulations, we found that by measuring the degree of mass segregation via the radial variation in average stellar mass, we were able to effectively separate clusters with and without a central black hole of mass $\sim 1\%$ of the total cluster mass. In particular, those clusters with an IMBH experienced a greatly reduced degree of mass segregation when compared with a similar cluster without an IMBH. This effect manifests itself in systems with a wide variety of initial conditions, spanning changes in the initial mass function, number of objects, and initial binary

fraction, as well as when we take care to replicate the realities of actually observing our simulations as if they were star clusters on the sky. We also found that a quick estimation of the degree of mass segregation can be obtained by measuring the average stellar mass at only two locations - the center of the cluster, and the half-mass radius.

The energy equipartition that leads to mass segregation still functions effectively despite the existence of an IMBH at the core of the cluster. However, as massive objects sink towards the center, they will encounter the IMBH, which spends the majority of its lifetime as a member of a binary or higher-order hierarchical system. These encounters will tend to impart energy to the sunken object, ejecting it from the core and remixing the stellar population. As they will also sink to the center and impart energy to massive segregated stars, a significant population of hard primordial binaries will also tend to limit mass segregation.

Because this effect is only visible in well-relaxed star clusters (those that have experienced $\gtrsim 5$ initial half-mass relaxation times), our method cannot be applied to all Galactic globular clusters to indicate the presence of an IMBH. Those that are (initially) too large may not have reached their equilibrium amount of mass segregation, thus providing an alternative explanation for a low degree of mass segregation.

Around 1/4 of the Galactic globular clusters meet our conservative requirements, and thanks to deep HST-ACS observations, data exist for many of them that are deep enough to allow our analysis. Chapter 4 details our application of this method to two of these clusters, NGC 2298 and NGC 6254 (M10).

As one of the smallest Galactic globular clusters, NGC 2298 is old enough dynamically to make it a good candidate for our analysis despite likely losing much of its mass to Galactic tidal stripping. It is also small enough that the observations

naturally extended to more than twice the half-mass radius, making it possible to examine the full radial mass segregation profile.

Taking care to replicate the observational realities as closely as possible while "observing" our simulations, we computed the average stellar mass at various clustercentric radii for each data set and compared them. The observations of NGC 2298 fell comfortably within the envelope of the subset of our simulations without an IMBH, and were inconsistent at around the $3 - \sigma$ level with our simulations with an IMBH. Thus, we concluded that NGC 2298 was very unlikely to harbor an IMBH, a result further strengthened by restricting our comparison to simulations that mimicked the NGC 2298 mass function.

In contrast to NGC 2298, NGC 6254 is significantly larger but far enough from the Galaxy to have retained nearly all of its initial mass. As such, it is still a good candidate for our analysis. Applying our method reveals a low degree of mass segregation that is inconsistent with our simulations without an IMBH or significant population of primordial binaries. Further observations that constrain the binary fraction could make a more definitive statement about the presence of an IMBH, but even lacking this information, NGC 6254 would be a good candidate for follow-up proper motion studies.

## 5.2    Potential Continuations of This Work

While we feel that we have made a contribution to MBH research, there is always more that can be done. Our results from Chapter 2 could be improved and expanded by resolving the errors described in Sec. 2.3.2. Unfortunately, we discovered the specific details of this problem late enough in the process of this work to prohibit a solution other than limiting the integration time, and thus the accumulated errors.

Provided our assessment of the nature of the error is correct, its elimination would immediately allow integration for significantly longer timescales, providing much better statistical data on the rate of EMRIs. This would also assuage concerns that this problem, which creates integration errors that are, to some degree, non-random, affects the validity of our results.

The results of Chapter 3 can be applied as in Chapter 4 to many other Galactic globular clusters. The requirements that we set out for selecting qualifying clusters were conservatively set; individual modeling of clusters that are reasonably close to our standards is likely to reveal that they qualify. Furthermore, the method can be applied to any cluster in an attempt to rule out the presence of an IMBH or large binary fraction. A high degree of observed mass segregation in a dynamically young cluster provides an even stronger null result. Application of this method to even a moderate fraction of Galactic globular clusters could help to constrain IMBH formation scenarios, as well as rates of IMBH-MBH merger events.

# Appendix A

# HNBDriver

We provide a full pseudocode of the HNBDriver code used to complete our second set of simulations including the particular details of the implementation. A few of the more important functions are given in all caps and then detailed below the main code.

SCANINPUTFILE

IF (restarting)

      - scan previous error accumulations from errors.dat

      - create an input file from the last HNBODY input and user input file

      - set t = restart time

ELSE

      - scan the initial conditions file

      - create an input file from the initial conditions file and user input

      - set t = 0

ENDIF

WHILE (t < finaltime)

      - call HNBODY

- copy body%.dat onto end of bodies/body%.dat

- get error from HNBODY output, add to current values

- print to log file and error file

- t += timestep


IF (CHECKFORPOSSIBLEEMRI)

    WHILE(1)

        - print input file to use HNDRAG with 1/10 original timestep

        - call HNDRAG

        - get error and print to log file and error file

        - t += timestep/10

        IF (MERGECHECK)

            - DELETEPARTICLE

            - create input file to run rest of original timestep

            - call HNBODY

            - get error and print to log file and error file

            - t += (appropriate fraction) * timestep

            BREAK

        ENDIF

        IF (mergetime > 1.25 * relaxtime)

            BREAK

        ENDIF

    ENDWHILE

ELSE

    print normal input file

ENDIF

ENDWHILE

SCANINPUTFILE - scans from the input file, driver.in. User specifies initial conditions input file, the initial number of objects, the mass of the MBH, the timestep and final integration time, the accuracy parameter of the HNBody integrations, the average mass of an object and the maximum semimajor axis (for calculating the local relaxation time), as well as whether or not we are restarting and if so from what time.

CHECKFORPOSSIBLEEMRI - checks each particle by comparing the local 2-body angular momentum relaxation time (Eq. 2.5 with the orbital semimajor axis replacing $r$), to its merge time due to gravitational radiation (Eq. 1.2). Returns 1 if any object has a merger time that's less, otherwise returns 0.

MERGECHECK - checks the particle for which we began integration with HN-Drag to see if it merits removal from the system. Our condition for removal is that its merger time be a small fraction of the local two-body angular momentum relaxation time - this fraction is specified by the used in driver.in, and was set at 25 for most of our simulations. While the object may still have thousands of years until the actual merger, this high ratio implies that it will be essentially dynamically isolated from the rest of the system and is extremely likely to inspiral and merge in peace.

DELETEPARTICLE - If the particle is to be deleted, we have to take care of merging the object, and giving the MBH a kick as it would get from an actual merger. In reality, the object would continue losing energy and angular momentum due to gravitational radiation until it reached the innermost stable circular orbit ($6GM/c^2$ for a non-spinning black hole), and then, to lowest order, plunge directly from there. We give our MBH a kick in a "random" direction (we actually choose the vector direction to the object at that exact moment for convenience) by calculating

the results of a perfectly inelastic collision between the MBH at that moment and the object if it were moving directly towards the MBH with velocity it would have as it crosses the innermost stable circular orbit. We increment the mass of the MBH by the mass of the merging object, decrement the number of objects in the system, and move the file containing the removed object's log to the folder /rmbodies. The files of each object with a particle number greater than the removed object's particle number are then decremented by one, as HNBody will always output the N small objects as body1.dat to bodyN.dat without skipping.

# Appendix B

# Our Experience with PKDGRAV

PKDGRAV was originally designed for cosmological simulations, but has since been adapted to a number of other applications due to its versatility. Several of the features of PKDGRAV suggested it would be well-suited to our purposes.

The code uses a leapfrog integration scheme to advance the positions and velocities of the objects in the system. It follows the following steps

1. Calculate the force of gravity $\vec{F}$ on each object at time $t$ from the positions of the other objects.

2. Calculate the velocity at the midpoint of the time step, $\Delta$, as $\vec{v}(t + 0.5\Delta) = \vec{v}(t) + 0.5(\vec{F}/m)\Delta$, where $m$ is the mass of the object.

3. Advance the position of the object with this new velocity: $\vec{x}(t + \Delta) = \vec{x}_0 + \vec{v}(t + 0.5\Delta)\Delta$

4. Recalculate gravity between the objects

5. Use the new forces to update the velocities: $\vec{v}(t + \Delta) = \vec{v}(t + 0.5\Delta) + 0.5(\vec{F}_1/m)\Delta$

6. Repeat steps 2-5.

While this integration scheme is fairly simplistic by comparison to other integration schemes, it has the nice feature of being time-reversible. The symplectic nature of the scheme implies that orbits that are well-resolved will return exactly to their original position and velocity (to machine precision). This means that the total energy deviation of the system is bounded, which would allow us to ensure limited error when integrating for long times as our application requires.

In addition to having nice energy conservation properties, PKDGRAV has two features that make it significantly faster than HNBody. The calculation of inter-particle forces consumes the vast majority of the computation time in direct N-body applications, resulting in the time of integration scaling as $t_{int} \propto N^2$ for a system of N objects. Tree codes calculate the force of gravity between close objects exactly but gain by calculating the force for distant particles using moments of the mass distribution (the full details of PKDGRAV's force calculations can be found in Stadel (2001)). This change changes the computation time scaling to $t_{int} \propto N\log N$. Besides this first enhancement, PKDGRAV also is a parallelized code, allowing the use of multiple processors simultaneously. This facet is especially efficient at decreasing computation time for higher numbers of objects.

While the potential to explore more objects for longer integration times made PKDGRAV an ideal base for our simulations, it began life as a purely Newtonian code. In order to fully resolve the effects of resonant relaxation, we needed to modify it to include the first-order Post-Newtonian correction to the potential. As a first attempt, we replaced the standard gravitational potential between our MBH and each other object by a modified potential:

$$\Phi(r) = \frac{GM}{r - \frac{3GM}{c^2}}, \tag{B.1}$$

where $M$ is the mass of the MBH. This potential approximately reproduces the precession of objects around the MBH, despite introducing a slight error into the mean

111

motion. While this solution proved to be reasonably accurate (usually well-within $\sim 10\%$ of the correct precession angle per orbit), accurately resolving encounters with pericenters low enough to be interesting for EMRI formation required reducing the timestep to prohibitively low values.

This general problem pervades nearly all N-body codes, as the difference between timescales of physical phenomena and desired integration time are frequently many orders of magnitude apart. Several common solutions to this problem exist, but are unsuited to our purposes. Artificial softening of the potential for close encounters between smaller objects and the MBH would succeed in eliminating unresolved encounters. However, it would also prevent the formation of any orbits close enough to form an EMRI, and thus would render the code useless. Many codes solve this problem by using variable timesteps, allowing for more accurate integration when it is needed. Unfortunately, this breaks the symplectic nature of the leapfrog integration, leading to unbounded (and rapid!) energy drift and neutralizing one of the advantages of PKDGRAV.

In an attempt to reconcile the vastly different time scales involved without introducing energy drift or softening, we created an adaptive, $4^{th}$-order Runge-Kutta (RK4) integrator to calculate the orbit of a test particle in the Schwarzschild metric. Objects that would venture within a user-specified radial threshold of the MBH during their next timestep are removed from the normal integration and calculated with the RK4 integrator. During this specialized integration, the object feels the full effects of both pericenter precession and radiation reaction, but is unaffected by forces from other objects in the system until it exits the threshold radius. Given the required proximity to the MBH before we invoke the RK4 integrator, this is an extremely close approximation to reality. Outside this critical radius, we simply apply the modified potential of Eq. B.1.
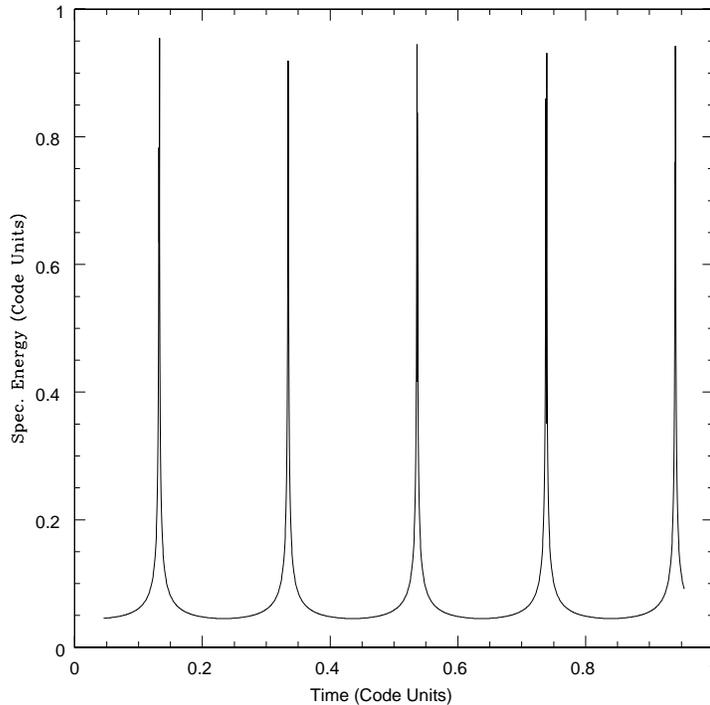
Figure B.1: Time-dependence of the negative specific Newtonian energy of a 10 $M_\odot$ particle orbiting a $1.0 \times 10^5 M_\odot$ MBH with a semimajor axis of 5.0 AU and an eccentricity of 0.95 in normal PKDGRAV. The spikes in the energy are occurring once an orbit, centered around the pericenter of the orbit. While other integrators will see a spurious drift in the energy over time, PKDGRAV will return to the same value each orbit (to machine precision).

Because of the nature of the leapfrog integrator that PKDGRAV uses, the incorporation of this RK4 subcode caused significant problems. Fig. B.1 shows the progression of the specific Newtonian energy of a particle in orbit around a MBH over a few orbital times. While the symplectic nature of the leapfrog integration ensures that there is no spurious energy drift over time in the orbit, we can see that the energy varies greatly throughout the orbit. In particular, it experiences a large

spike near pericenter, where we are focusing our attention. Because of this steep radial energy gradient, removing the particle from normal integration and returning it at approximately the same radius some number of timesteps later is insufficient. Despite the near-perfect energy conservation of the RK4 integrator, the particle will experience significant energy changes over only a few orbits as we put the particle back at a different place in the leapfrog's artificial potential well each orbit.

We tried several solutions to this problem, including fitting various functional forms to the radial variation in the particle's energy, then attempting to interpolate the energy at the exit radius on the assumption that the energy variation was symmetric about pericenter. As our final attempt to solve this energy problem, we tried reinserting the particle at precisely the radius at which it entered the RK4 integrator. Since this will occur between timesteps, we were introducing an error into the mean motion of the particle by artificially moving it forward or backward in time to sync it up with the rest of the system. This error will grow as a random walk in time, but given that the mean motion does not affect any of the physical quantities related to resonant or 2-body relaxation, nor the pericenter of the particle's orbit, it should not have a significant statistical effect on the rate of EMRI formation. However, even with this final modification, we still encountered a monotonic drift in the orbital energy of a particle that was removed and later replaced.

In addition to the problems with replacing the removed objects back into the system, we encountered another problem with the setup. In PKDGRAV, our MBH is actually not a particle in the system at all, but simply the potential well that is associated with a MBH fixed at the origin. In order to simulate the motion of the MBH, each step we calculate (assuming the modified potential)

$$\vec{a}_\bullet = \sum_{i=1}^{n} \frac{m_i}{\left(r_i - \frac{3Gm_i}{c^2}\right)^2} \hat{r}_i,$$
(B.2)

where $m_i$ is the mass of the particle, $r_i$ is its radial distance from the origin, and $\hat{r}_i$

is the unit vector from the origin to the particle. The sum components are simply the first derivatives of the modified potential from Eq. B.1 applied to each particle instead of the MBH. This acceleration is subtracted from the accelerations of all of the particles in the system, thus replicating the effective motion of the MBH.

The problem occurs because the presence of the RK4 integrator allows particles to repeatedly come very close to the origin - before this modification, such a particle would likely be ejected because the encounter was unresolved, or, if using softening, it would be sent on a different orbit. In either case it would not return for another close pericenter passage. A particle whose position is very nearly at the origin can deliver an unphysically large contribution to $\vec{a}_\bullet$ when the timestep is fixed, and thus an unphysically large acceleration to all of the other particles in the system. Repeated kicks of this nature will rapidly cause the outer particles in the system to become unbound. In order to prevent this, for all particles that are close enough to the origin to use the RK4 integrator, we replace that particle's contribution to the sum from Eq. B.2 with the actual average acceleration experienced by the MBH during that step:

$$\vec{a}_{real} = -\frac{m}{M_\bullet} \frac{\vec{v_f} - \vec{v_i}}{\Delta}, \qquad (\text{B.3})$$

where m is the mass of the small particle, and $\vec{v_i}$ and $\vec{v_f}$ are the velocities of the particle before and after integration with the RK4 code for a timestep $\Delta$. Because the calculation of $\vec{a}_{real}$ and the normal calculation of $\vec{a}_{MBH}$ happen at different points during a normal PKDGRAV step, significant modification was needed to implement this change. Below is a pseudocode of a normal PKDGRAV step after these modifications:

- Each step begins with the positions, velocities and accelerations of each particle synced. If a particle was integrated using the RK4 integrator on the last

step, its structure will have the previous $\vec{a}_{real}$ saved as well, which we will call $\vec{a}_{prev}$

- Call the function that drives the RK4 integrator:

a) Check each particle to see if it needs to be integrated separately. If not, ignore it

b) If so, flag it to be removed from normal integration and calculate its new position and velocity

c) Calculate $\vec{a}_{real}$ for that particle, and save it in the particle structure

d) Calculate $\vec{a}_{correction}$ for that particle - if we were outside the RK4 integrator the last time, then

$$\vec{a}_{correction} = \vec{a}_{real} - \frac{m}{\left(r - \frac{3Gm}{c^2}\right)^2}\hat{r}, \tag{B.4}$$

where $m$ is the mass of the particle, $r$ is its distance from the origin, and $\hat{r}$ is the unit vector to the particle from the origin. If the particle did use the RK4 integrator the last step, then

$$\vec{a}_{correction} = \vec{a}_{real} - \vec{a}_{prev} \tag{B.5}$$

e) Sum the $\vec{a}_{correction}$ values for each particle (if there happens to be more than one)

- Call a function that subtracts $\vec{a}_{correction}$ from each particle's acceleration - thus eliminating the old acceleration components that were previously added and replacing them with updated values.

- Now we resume normal leapfrog integration - first calculate the new velocities:
$\vec{v}_i(t + 0.5\Delta) = \vec{v}_i(t) + \frac{1}{2}\vec{a}_i(t)\Delta$

- Use the updated velocities to advance each particle to its new position:

  $\vec{r}_i(t + \Delta) = \vec{r}_i(t) + \vec{v}_i(t + 0.5\Delta)\Delta$

- Recalculate gravity, and thus each particle's acceleration. If the particle was integrated using the RK4 integrator during the step, we use the saved value of $\vec{a}_{real}$ instead of the contribution from Eq. B.2.

- Update the velocities to sync with the positions/accelerations:

  $\vec{v}_i(t + \Delta) = \vec{v}_i(t + 0.5\Delta) + \frac{1}{2}\vec{a}_i(t + \Delta)\Delta$

Despite these modifications, the problem of successfully applying the force on the center of mass of the system retroactively while using the RK4 subintegrator was never entirely solved. The integrated motion of the "MBH" (and thus the negative of the accelerations that were applied to other objects in the system) never remained near the origin of the system, resulting in the spurious ejection of loosely bound objects.

Due to these two complications never being adequately resolved, we were forced to abandon PKDGRAV despite the numerous potential advantages it provided.

# Appendix C

# Post-Defense Work

Due to uncertainties introduced by the code error described in Sec. 2.3.2, the results of Chapter 2 were limited in nature. In an attempt to rectify this uncertainty, we located and fixed the main source of angular momentum error in the code and performed numerous new simulations without a spurious and unavoidable accumulation of error. This Appendix details the results of these new runs.

## C.1   Modifications to HNBody and HNDrag

The source of the error in the previous version was due to the omission of the two terms in the original Newhall et al. (1983) implementation of the first-order Post-Newtonian correction (Eq. 2.32). The two terms omitted were those containing the barycentric acceleration of the other objects in the system, which are $\propto \ddot{\vec{r}}_j$ in Eq. 2.32. They were initially omitted because the original authors did not intend for the code to be used with the Post-Newtonian correction in a system with many massive particles. However, they are necessary for proper integration in barycentric coordinates.

With the inclusion of these terms, the error accumulation is slow enough that

we were able to integrate for more than twice as long, while incurring a factor of $> 10^3$ less error in the angular momentum. This not only increases our statistical significance by enlarging the sample size, but also greatly enhances our confidence in the robustness of the results.

While the integrations with HNBody went off without a hitch, the new changes caused a problem during the HNDrag integrations that prevented us from resolving the final state of our EMRI candidates. Shortly after beginning their integrations with HNDrag, which happens when their time to merge due to gravitational radiation is lower than the local 2-body relaxation time (see Appendix A for more details on HNBDriver), all objects with a low enough pericenter were ejected from their host system with a velocity greater than the speed of light. Obviously, this is unphysical and prevents us from following these objects as they lose energy and angular momentum to see if they do indeed end as EMRI events.

We were unable to ascertain the cause of these ejections (other than the very low pericenters of the orbiting objects involved), and were forced to simply remove the objects from the simulations after their ejection and document their orbital elements. Due to conservation of momentum, the central mass also received a large kick during these events, resulting in the ejection of a few of the loosely bound objects in the simulations. After experiencing such an event, the systems soon settled down to a new equilibrium, so we allowed the simulations to proceed from this point despite the large energy and angular momentum errors introduced by the ejection.

Due to the inability to further follow the systems with the effects of the general relativistic radiation reaction terms, we are once again forced to speculate to some degree about the final state of these objects. Given that in our previous set of simulations, all but one of the objects that began integration with HNDrag ended as EMRI events, it seems likely that many of them would also experience that fate.

Table C.1: Summary of the Third Set of N-body simulations of systems with an MBH.

| # of Sims | N | $\langle m \rangle / M_\odot$ | $\tau_{merge,i}$ restricted? | $\langle t_{final} \rangle$/yr | Merger Rate (yr$^{-1}$) |
|---|---|---|---|---|---|
| 8 | 50 | 50 | Yes | 3.4e6 | 2.6e-7 |
| 4 | 100 | 25 | Yes | 9.6e5 | 2.6e-7 |

Note. — The simulations in this group were started from identical initial conditions to those from the $2^{nd}$ group of those detailed in Tab. 2.5, and with the same required factor of 25 between the merger time and local relaxation time before we merged the objects.

## C.2 Simulation Results

We reran a subset of the simulations found in Tab. 2.5 with identical initial conditions, but using the new software detailed above. The HNBDriver code remained essentially unchanged except for the addition of a subroutine to eliminate ejected objects from the simulation. The details of the 12 simulations we performed for this Appendix are given in Tab. C.1, and correspond to the 12 simulations below the middle line in Tab. 2.5.

Also detailed in Tab. C.1 are the simulation-averaged rates of merger events. We can see that the data from these new simulations are consistent across the two values of $N$, as well as being consistent with the rates that we found in Chapter 2 and the results frequently found in the literature. This agreement suggests that the repeated kicks caused by low-pericenter orbits in our previous simulations were not systematically influencing the formation of EMRI-event objects as we feared they might be.

Fig. C.1 shows the evolution of the orbital elements of the objects in our 50-object simulations whose merger time due to gravitational radiation was less than the local 2-body relaxation time and began integration with HNDrag. We can
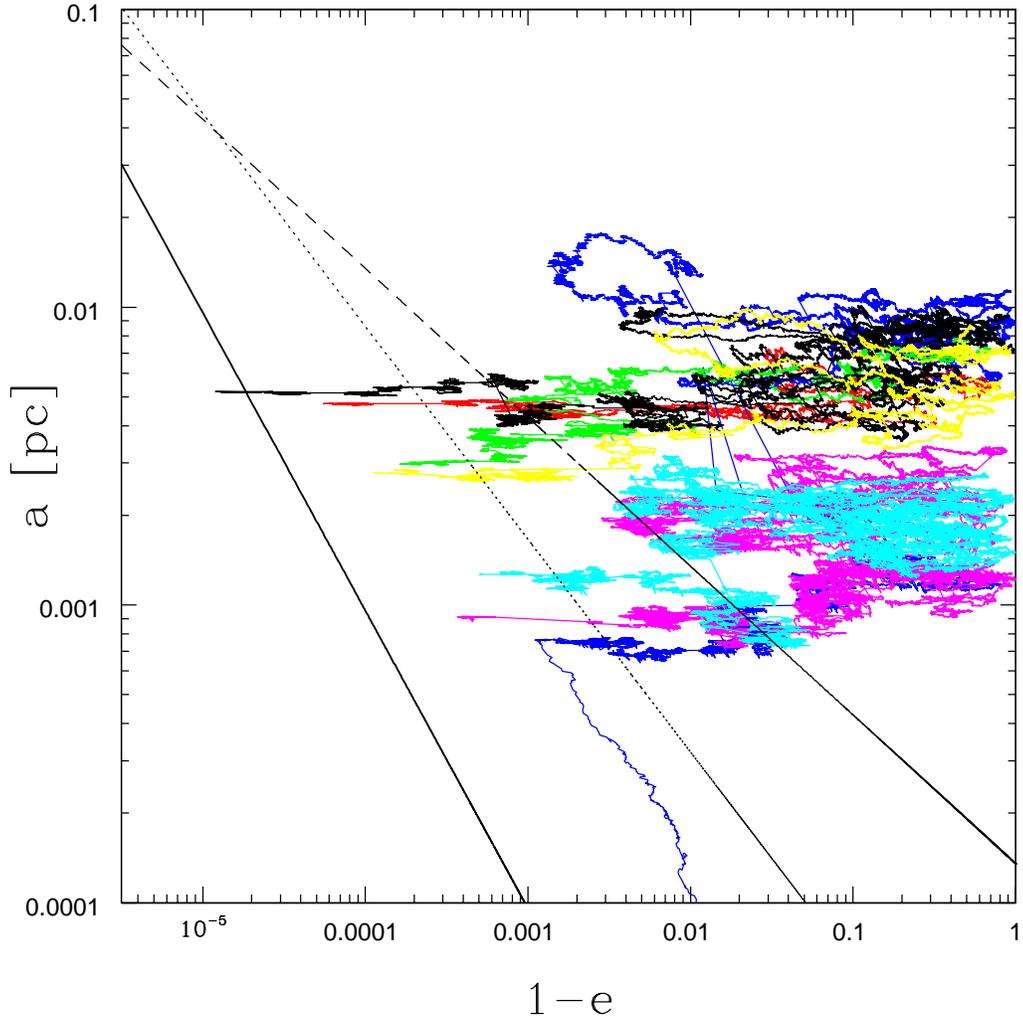
Figure C.1: Orbital evolution of the objects in the new 50-object simulations that ended up as merger events. Also plotted, as in Fig. 2.7 are the Schwarzschild barrier, the plunge line, and the critical eccentricity line with $C_{EMRI} = 0.1$. We can see that the object with the solid black color actually crosses the plunge line before its integration with HNDrag begins - in reality this object would have been losing energy and angular momentum during its time across the Schwarzschild barrier and may have not plunged.

see that, due to the fact that the HNBDriver code only checks for this condition periodically, that one of the objects actually drifts across the plunge line and back before actually being caught. In a totally realistic system, all of these objects would have begun losing energy and angular momentum long before the HNBDriver code identifies that they are on close enough orbits to warrant use of HNDrag. Since running the entire simulation with HNDrag would be computationally prohibitive due to the increased complexity of the equations of motion, this could be partially assuaged by using a lower threshold for changing over and by decreasing the length of each individual time segment in HNBDriver.

Due to the fact that all but one of our potential EMRI objects were ejected from their respective systems prior to losing significant energy and angular momentum due to gravitational radiation, we cannot be certain they would end as EMRIs rather than plunging or being kicked back to a lower eccentricity. Given that nearly all such objects ended as EMRIs in Chapter 2, we suspect that this population is also likely to meet a similar fate. However, due to this uncertainly, we choose not to speculate about the final orbital elements they would have given they must still interact with their host cluster for a significant time prior to inspiral. We do note that, like the population in Chapter 2, the semimajor axes remain smaller than those predicted in the literature.

Overall, the results of these new simulations increase our confidence in there results of Chapter 2. We have replicated the EMRI rates found in that Chapter, with about a factor of 4 more total integration time reducing the statistical noise. Once again, there was not a large difference between the results of our simulations with $N = 100$ and $N = 50$ objects, suggesting that further spreading the mass in the simulation among a larger number of objects should not significantly affect our conclusions.

Future work could further still refine the results by somehow preventing the ejections discussed earlier in this Appendix - this could be accomplished either by beginning the integrations with HNDrag earlier in the evolution of these objects before they reach a low enough pericenter to be ejected, or conceivably by figuring out and eliminating the specific problem in the equations of motion. This would allow a more comprehensive statement to be made about the final distribution of these objects when they reach the EMRI phase.

# Bibliography

Aarseth, S. J. 2003, Gravitational N-Body Simulations, ed. Aarseth, S. J.

Albrow, M. D., Gilliland, R. L., Brown, T. M., Edmonds, P. D., Guhathakurta, P.,
  &amp; Sarajedini, A. 2001, ApJ, 559, 1060

Amaro-Seoane, P., Gair, J. R., Freitag, M., Miller, M. C., Mandel, I., Cutler, C. J.,
  &amp; Babak, S. 2007, Classical and Quantum Gravity, 24, 113

Bahcall, J. N., & Wolf, R. A. 1976, ApJ, 209, 214

Barack, L., & Cutler, C. 2004, Phys. Rev. D, 69, 082005

Baraffe, I., Chabrier, G., Allard, F., & Hauschildt, P. H. 1997, A&A, 327, 1054

Baumgardt, H., De Marchi, G., & Kroupa, P. 2008, ApJ, 685, 247

Baumgardt, H., Hut, P., Makino, J., McMillan, S., & Portegies Zwart, S. 2003a,
  ApJ, 582, L21

Baumgardt, H., & Makino, J. 2003, MNRAS, 340, 227

Baumgardt, H., Makino, J., & Ebisuzaki, T. 2004, ApJ, 613, 1143

Baumgardt, H., Makino, J., Hut, P., McMillan, S., & Portegies Zwart, S. 2003b,
  ApJ, 589, L25

Beccari, G., Pasquato, M., De Marchi, G., Dalessandro, E., Trenti, M., & Gill, M.
  2010, ApJ, 713, 194

Begelman, M. C., Blandford, R. D., & Rees, M. J. 1984, Reviews of Modern Physics,
  56, 255

Blanchet, L. 2006, Living Reviews in Relativity, 9

Carretta, E., & Gratton, R. G. 1997, A&AS, 121, 95

Casertano, S., & Hut, P. 1985, ApJ, 298, 80

Cool, A. M., Piotto, G., & King, I. R. 1996, ApJ, 468, 655

De Marchi, G., & Paresce, F. 1996, Science with the Hubble Telescope, 310

De Marchi, G., Paresce, F., & Pulone, L. 2007, ApJ, 656, L65

de Marchi, G., & Pulone, L. 2007, A&A, 467, 107

Djorgovski, S. 1993, in Astronomical Society of the Pacific Conference Series, Vol. 50,
Structure and Dynamics of Globular Clusters, ed. S. G. Djorgovski & G. Meylan,
373

Dull, J. D., Cohn, H. N., Lugger, P. M., Murphy, B. W., Seitzer, P. O., Callanan,
P. J., Rutten, R. G. M., & Charles, P. A. 2003, ApJ, 585, 598

Efron, B. 1979, Ann. Stat., 7, 1

Eisenhauer, F., Genzel, R., Alexander, T., Abuter, R., Paumard, T., Ott, T.,
Gilbert, A., Gillessen, S., Horrobin, M., Trippe, S., Bonnet, H., Dumas, C., Hubin,
N., Kaufer, A., Kissler-Patig, M., Monnet, G., Ströbele, S., Szeifert, T., Eckart,
A., Schödel, R., & Zucker, S. 2005, ApJ, 628, 246

Ferrarese, L., & Merritt, D. 2000, ApJ, 539, L9

Fregeau, J. M., & Rasio, F. A. 2007, ApJ, 658, 1047

Freitag, M. 2001, Classical and Quantum Gravity, 18, 4033

Freitag, M., Amaro-Seoane, P., & Kalogera, V. 2006, ApJ, 649, 91

Freitag, M., & Benz, W. 2002, A&A, 394, 345

Gebhardt, K., Bender, R., Bower, G., Dressler, A., Faber, S. M., Filippenko, A. V.,
Green, R., Grillmair, C., Ho, L. C., Kormendy, J., Lauer, T. R., Magorrian, J.,
Pinkney, J., Richstone, D., & Tremaine, S. 2000, ApJ, 539, L13

Gebhardt, K., Rich, R. M., & Ho, L. C. 2002, ApJ, 578, L41

—. 2005, ApJ, 634, 1093

Gerssen, J., van der Marel, R. P., Gebhardt, K., Guhathakurta, P., Peterson, R. C., & Pryor, C. 2002, AJ, 124, 3270

—. 2003, AJ, 125, 376

Gill, M., Trenti, M., Miller, M. C., van der Marel, R., Hamilton, D., & Stiavelli, M. 2008, ApJ, 686, 303

Gültekin, K., Richstone, D. O., Gebhardt, K., Lauer, T. R., Tremaine, S., Aller, M. C., Bender, R., Dressler, A., Faber, S. M., Filippenko, A. V., Green, R., Ho, L. C., Kormendy, J., Magorrian, J., Pinkney, J., & Siopis, C. 2009, ApJ, 698, 198

Gürkan, M. A., & Hopman, C. 2007, MNRAS, 379, 1083

Harris, W. E. 1996, AJ, 112, 1487

Heggie, D., & Hut, P. 2003, The Gravitational Million-Body Problem: A Multidisciplinary Approach to Star Cluster Dynamics, ed. Heggie, D. & Hut, P.

Heggie, D. C. 1986, in Lecture Notes in Physics, Berlin Springer Verlag, Vol. 267, The Use of Supercomputers in Stellar Dynamics, ed. P. Hut & S. L. W. McMillan, 13

Heggie, D. C., Hut, P., Mineshige, S., Makino, J., & Baumgardt, H. 2007, PASJ, 59, L11

Heggie, D. C., Trenti, M., & Hut, P. 2006, MNRAS, 368, 677

Hils, D., & Bender, P. L. 1995, ApJ, 445, L7

Hopman, C., & Alexander, T. 2005, ApJ, 629, 362

—. 2006a, ApJ, 645, 1152

—. 2006b, ApJ, 645, L133

Hulse, R. A., & Taylor, J. H. 1975, ApJ, 195, L51

Hurley, J. R. 2007, MNRAS, 379, 93

Hurley, J. R., Pols, O. R., & Tout, C. A. 2000, MNRAS, 315, 543

King, I. R. 1966, AJ, 71, 64

Kormendy, J., & Gebhardt, K. 2001, in American Institute of Physics Conference Series, Vol. 586, 20th Texas Symposium on relativistic astrophysics, ed. J. C. Wheeler & H. Martel, 363–381

Kormendy, J., & Richstone, D. 1995, ARA&A, 33, 581

Krauss, L. M., & Chaboyer, B. 2003, Science, 299, 65

Kroupa, P. 2001, MNRAS, 322, 231

Larson, S. L., Hiscock, W. A., & Hellings, R. W. 2000, Phys. Rev. D, 62, 062001

Lynden-Bell, D. 1969, Nature, 223, 690

Marconi, A., Risaliti, G., Gilli, R., Hunt, L. K., Maiolino, R., & Salvati, M. 2004, MNRAS, 351, 169

McLaughlin, D. E., & van der Marel, R. P. 2005, ApJS, 161, 304

Merritt, D., Alexander, T., Mikkola, S., & Will, C. 2011, ArXiv e-prints

Merritt, D., Piatek, S., Portegies Zwart, S., & Hemsendorf, M. 2004, ApJ, 608, L25

Miller, G. E., & Scalo, J. M. 1979, ApJS, 41, 513

Miller, M. C. 2006, MNRAS, 367, L32

Miller, M. C., Alexander, T., Amaro-Seoane, P., Barth, A., Cutler, C., Gair, J., Hopman, C., Merritt, D., Phinney, E. S., & Richstone, D. 2009, in ArXiv Astrophysics e-prints, Vol. 2010, astro2010: The Astronomy and Astrophysics Decadal Survey, 209

Miller, M. C., & Colbert, E. J. M. 2004, International Journal of Modern Physics D, 13, 1

Miller, M. C., Freitag, M., Hamilton, D. P., & Lauburg, V. M. 2005, ApJ, 631, L117

Miller, M. C., & Hamilton, D. P. 2002, MNRAS, 330, 232

Milone, A. P., Piotto, G., Bedin, L. R., & Sarajedini, A. 2008, Mem. Soc. Astron. Italiana, 79, 623

Newhall, X. X., Standish, E. M., & Williams, J. G. 1983, A&A, 125, 150

Noyola, E., & Gebhardt, K. 2006, AJ, 132, 447

Noyola, E., Gebhardt, K., & Bergmann, M. 2008, ApJ, 676, 1008

Pasquato, M., & Bertin, G. 2008, A&A, 489, 1079

Pasquato, M., Trenti, M., De Marchi, G., Gill, M., Hamilton, D. P., Miller, M. C., Stiavelli, M., & van der Marel, R. P. 2009, ApJ, 699, 1511

Peters, P. C. 1964, Physical Review, 136, 1224

Piotto, G., & Zoccali, M. 1999, A&A, 345, 485

Portegies Zwart, S. F., Baumgardt, H., Hut, P., Makino, J., & McMillan, S. L. W. 2004, Nature, 428, 724

Pulone, L., De Marchi, G., Covino, S., & Paresce, F. 2003, A&A, 399, 121

Rauch, K. P., & Tremaine, S. 1996, , 1, 149

Richstone, D., Ajhar, E. A., Bender, R., Bower, G., Dressler, A., Faber, S. M., Filippenko, A. V., Gebhardt, K., Green, R., Ho, L. C., Kormendy, J., Lauer, T. R., Magorrian, J., & Tremaine, S. 1998, Nature, 395, A14

Ryan, F. D. 1995, Phys. Rev. D, 52, 5707

Salpeter, E. E. 1955, ApJ, 121, 161

—. 1964, ApJ, 140, 796

Sigurdsson, S., & Rees, M. J. 1997, MNRAS, 284, 318

Soltan, A. 1982, MNRAS, 200, 115

Spitzer, L. 1987, Dynamical evolution of globular clusters, ed. Spitzer, L.

Stadel, J. G. 2001, PhD thesis, UNIVERSITY OF WASHINGTON

Stetson, P. B. 1987, PASP, 99, 191

—. 1994, PASP, 106, 250

Trenti, M., Ardi, E., Mineshige, S., & Hut, P. 2007a, MNRAS, 374, 857

Trenti, M., Heggie, D. C., & Hut, P. 2007b, MNRAS, 374, 344

Trenti, M., Ransom, S., Hut, P., & Heggie, D. C. 2008, MNRAS, 387, 815

van der Marel, R. P. 2004, Coevolution of Black Holes and Galaxies, 37

Vesperini, E., & Chernoff, D. F. 1994, ApJ, 431, 231

Weisberg, J. M., Nice, D. J., & Taylor, J. H. 2010, ApJ, 722, 1030

Wen, L., & Gair, J. R. 2005, Classical and Quantum Gravity, 22, 445

Woosley, S. E., Heger, A., & Weaver, T. A. 2002, Reviews of Modern Physics, 74, 1015